PL-TR-94-2197

HIGH RESOLUTION DESCRIPTIONS OF IRAS 12 AND 25 MICRONS CONFUSED REGIONS

R. M. Kennealy   R. Canterna
R. S. Sample   R. Hermann
J. P. Kennealy   L. Townsley
R. A. Gonsalves

DTIC
ELECTE
SEP 0 6 1994
F
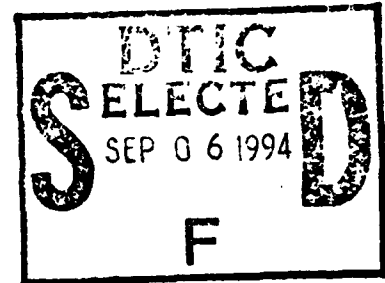
Mission Research Corporation
735 State Street
P.O. Drawer 719
Santa Barbara, CA 93102

April 1994

94-28882

Final Report
9 January 1990-30 September 1993
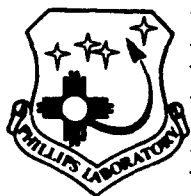
PHILLIPS LABORATORY
Directorate of Geophysics
AIR FORCE MATERIEL COMMAND
HANSCOM AIR FORCE BASE, MA 01731-3010

This technical report has been reviewed and is approved for publication

STEPHAN D. PRICE
Contract Manager

STEPHAN D. PRICE
Branch Chief

ROGER VAN TASSEL
Division Director

This report has been reviewed by the ESC Public Affairs Office (PA) and is releasable to the National Technical Information Service (NTIS).

Qualified requestors may obtain additional copies from the Defense Technical Information Center. All others should apply to the National Technical Information Service.

If your address has changed, or if you wish to be removed from the mailing list, or if the addressee is no longer employed by your organization, please notify PL/TSI, Hanscom AFB, MA 01731-3010. This will assist us in maintaining a current mailing list.

Do not return copies of this report unless contractual obligations or notices on a specific document requires that it be returned.

REPORT DOCUMENTATION PAGE

1. AGENCY USE ONLY *(Leave blank)*	2. REPORT DATE April 1994	3. REPORT TYPE AND DATES COVERED Final (9 Jan 1990 – 30 Sep 1993)

4. TITLE AND SUBTITLE
High Resolution Descriptions of IRAS 12 and 25 Microns Confused Regions

5. FUNDING NUMBERS
PE 62101F
PR 7670 TA 06 WU AV
Contract F19628-90-C-0110

6. AUTHOR(S)
R. M. Kennealy R. A. Gonsalves* L. Townsley**
R. S. Sample R. Canterna**
J. P. Kennealy R. Hermann**

7. PERFORMING ORGANIZATION NAME(S) AND ADDRESS(ES)
Mission Research Corporation
735 State Street
P. O. Drawer 719
Santa Barbara, CA 93102

8. PERFORMING ORGANIZATION REPORT NUMBER

9. SPONSORING/MONITORING AGENCY NAME(S) AND ADDRESS(ES)
Phillips Laboratory
29 Randolph Road
Hanscom AFB, MA 01731-3010

Contract Manager: Stephan Price/ GPOB

10. SPONSORING/MONITORING AGENCY REPORT NUMBER
PL-TR-94-2197

11. SUPPLEMENTARY NOTES
* Tufts University
** University of Wyoming

12a. DISTRIBUTION/AVAILABILITY STATEMENT

Approved for public release; distribution unlimited

12b. DISTRIBUTION CODE

13. ABSTRACT *(Maximum 200 words)*

12 and 25 micron IRAS Survey and AO footprint scan data in the galactic plane have been reprocessed as images for 2-dimensional point source extractions in an effort to provide a point source catalog supplement which is more complete than the IRAS PSC in the regions labeled "confused" by IRAS. Approximately 3500 square degrees of sky are available as an atlas of high resolution galactic plane images (14.4") pixels. For each region of the sky, there are separate background and point source images. Point source extraction results indicate that the 2-D processing improves completeness over the PSC everywhere in the plane, and increases source counts by a factor of 2-4 over the PSC.

14. SUBJECT TERMS
Point source extraction Additional observation
Maximum entropy
High resolution galactic plane images
IRAS survey

15. NUMBER OF PAGES
136

16. PRICE CODE

17. SECURITY CLASSIFICATION OF REPORT	18. SECURITY CLASSIFICATION OF THIS PAGE	19. SECURITY CLASSIFICATION OF ABSTRACT	20. LIMITATION OF ABSTRACT
Unclassified	Unclassified	Unclassified	SAR

TABLE OF CONTENTS

List of Figures

List of Tables

1.0 INTRODUCTION

While the IRAS Point Source Catalog is the best available data base of the infrared stars, distribution and characteristics, it is well known to the space surveillance community that the PSC v.2 is incomplete in regions which are important clutter backgrounds for sensor systems. This is shown in Figure 1., which is a plot of all the PSC sources in the galactic center region fainter than 1.0 Jy. The absence of sources is the antithesis of the true source distribution in the galactic center. The purpose of the "High Resolution" program was to re-process the 12 and 25 μm IRAS Survey data in the regions which were "confused" for IRAS, (mainly the galactic plane) and make a supplementary point source catalog which is complete to fainter fluxes than the PSC. The new Point Source List Database is called the Galactic Plane Supplement (GPS) to the IRAS Point Source Catalog. It is accompanied by an atlas of high resolution (14.4 arc second pixels) images of the galactic plane. The 60 and 100 micron IRAS survey data were not re-processed because that wavelength range is beyond the interest of the surveillance community, and because the resolution of these data is significantly lower than that of the 12 and 25 micron data.

Phillips Laboratory/GPOB at Hanscom AFB sponsored the effort, which was led by the Space and Atmospherics Division of Mission Research Corporation. IPAC provided the large amounts of "raw" survey data required for re-processing, and gave information and advice as needed. Robert Gonsalves of Tufts University provided consultation support to MRC in much of the algorithm development for the survey data processing. The University of Wyoming performed ground-based validation measurements and independent processing of AOs in the confused regions as verification for the survey processing results.

2.0 DEFINITION OF CONFUSED REGIONS

Definition of the regions to be re-processed under this effort was made by plotting the locations of sources with confusion flags set in the PSC. The CONFUSE, PNEARH, PNEARW, SES1 and SES2 flags were all examined. Plots of PSC sources with the CONFUSE flag set for the 12 or 25 μm band were used to subjectively bound the regions to be re-processed. The bounded area includes most of the galactic plane, and small regions in Orion, Cygnus, Ophiucus, and the Magellanic Clouds. The "galactic plane region" is a band six to fifteen degrees wide, centered on the galactic plane, with 100 degrees of extent in galactic longitude on both sides of the center. All of the named regions except the Magellanic Clouds are included in the new Galactic Plane Supplement Point Source List Database. Figure 4.1 is a map of the regions where survey data was re-processed.
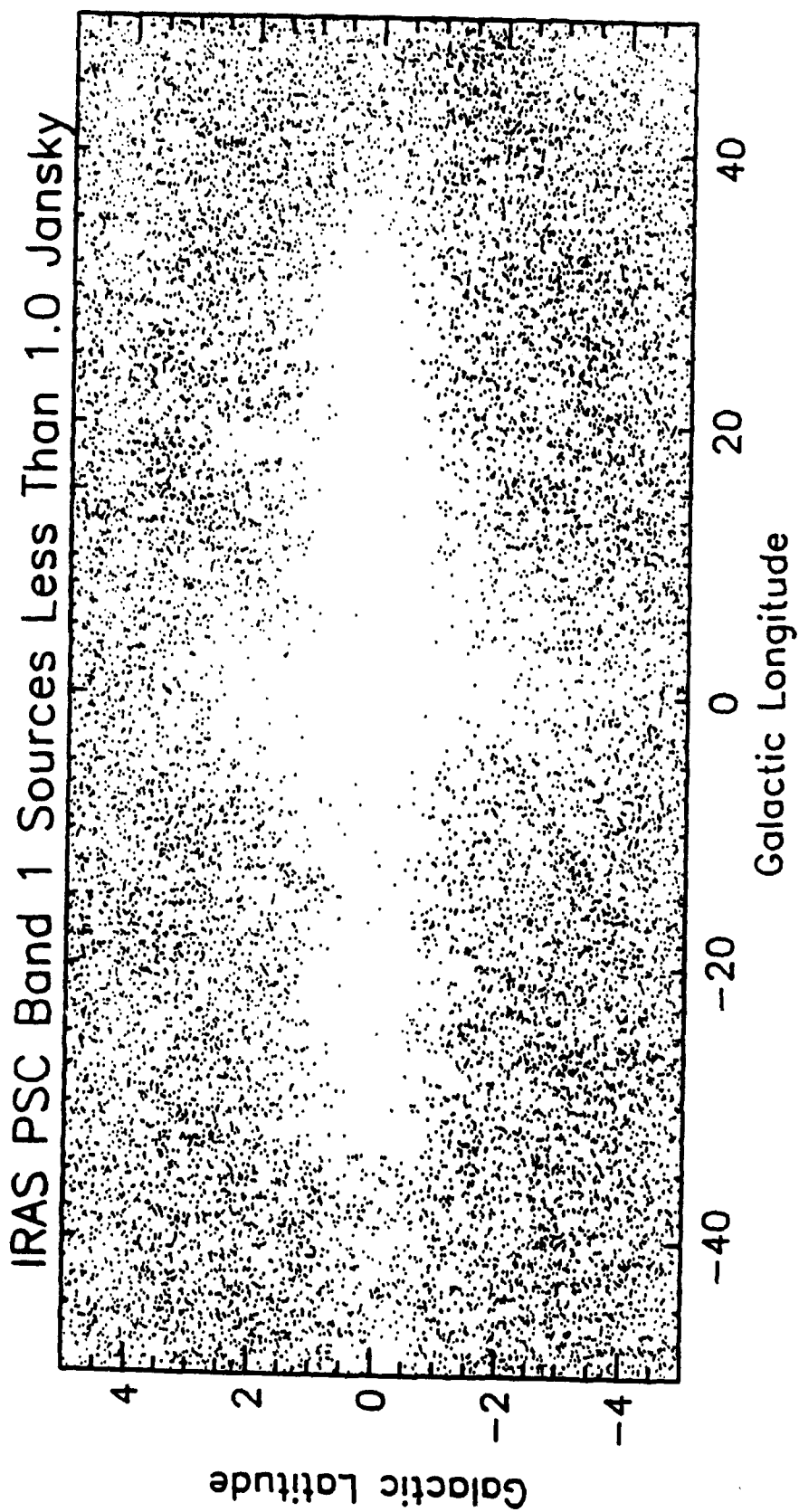
Figure 1.0 IRAS PSC Sources < 1.0 Jy in the Galactic Center.

3.0 METHODS OVERVIEW

3.1 2-D vs. 1-D Processing

At the heart of the Galactic Plane Supplement (GPS) Re-processing is the belief that more information may be gleaned from 2-Dimensional *image* representations of the IRAS survey data than from the 1-D scans and rule sets which were used to compile the PSC. MRC and the University of Wyoming (UoW) set out to perform point source extraction on *images* of confused regions. The images were constructed from survey and AO scans in footprint form at "high resolution", i.e., the pixel size of the image grid was set by the survey scan rate/sample spacing. The images were submitted to sophisticated object estimation algorithms which identified point source objects and derived their locations and amplitudes.

3.2 Roles of Survey data, AO data, and Ground Based Measurements

MRC performed image construction and point source extraction on about 5000 square degrees of survey scan snips which completely covered the galactic plane (boundaries noted in section 2.0). The GPS point source database is the point source extracted re-processed survey data. While MRC processed survey data, UoW used different and completely independent image processing algorithms on a set of AOs (total of ~ 200 square degrees of sky) in the confused regions. They produced a catalog whose purpose is to provide spot check, independent verification of the point source extraction results of the survey processing. Likewise, UoW performed ground based observations using a 10 μm bolometer array at the Wyoming Infrared Observatory (WIRO) to provide another source of validation for the survey re-processing results.

3.3 Survey Processing Overview

Sections 4 through 17 of this document detail the MRC image processing of survey data. This section is a high level overview of survey processing. Refer to the flowchart in Figure 3.3.

IRAS Survey data was provided to MRC by IPAC as 6° x 6° plates of position tagged scan snips. For each plate, MRC's survey processing begins with sorting the scan snips in each plate by SOP and scan rotation angle into 3 groups. Each group is called an "HCON" in the context of this project, and is destined to become an image. A series of data conditioning operations are applied *to the scans* prior to image construction. These include rotation (so x,y position tags are aligned with vertical and horizontal array elements), estimation of noise, separation of diffuse background structure from point source and high frequency noise, in-scan phasing, and interpolation over gaps. See Section 5 for details.

Image construction begins with a set of *conditioned* position tagged scans. The conditioned scan snips are cross scan interpolated onto a grid whose pixel size is 14.4 arc
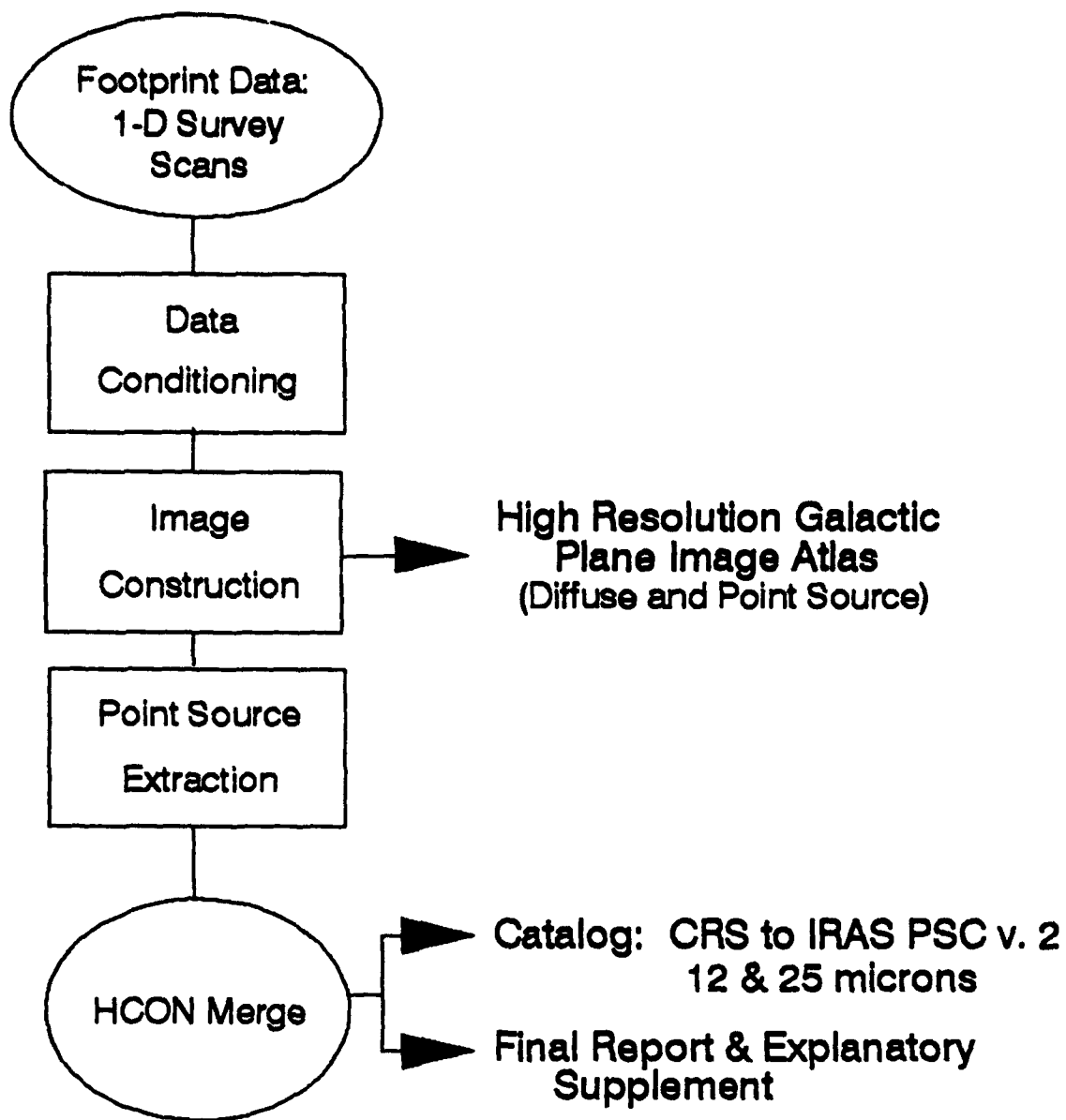
Figure 3.3   Overview of IRAS Survey Re-processing in the Galactic Plane.

4

seconds, the nominal in-scan sample spacing at the survey scan rate. Relative to the image grid, the cross scan density of the scan set is sparse by about a factor of 5. Each pixel in the image grid is filled with a flux density value based on the local scan data samples. Each interpolated flux value is a weighted sum of the flux values of nearby data samples. The weights are computed taking into account the relative proximity of each contributing data sample to the interpolation site, and the point response function (PRF) and noise associated with each data sample. The resulting image is a representation of the sky convolved with an ideal PRF (as opposed to the sky convolved with 14 different PRFs mixed in various regions of the scene). In each band, an "ideal" composite PRF was made from averaging the response profiles of the largest detectors. For each "plate" region, there are three HCON images in each band which go on to the point source extraction algorithm. See Section 6 for details.

Point Source Extraction is performed by a 2-Dimensional image processing algorithm. It uses an iterative least squares deconvolution with a positivity constraint and a local maximum criterion to recover the point source positions. Those candidate point source locations are used to create an ideal data scene. In the ideal data scene, the amplitudes at the point source locations are the unknown, but 'true' point source flux densities. That set of flux densities is solved for by minimizing the mean square error between the real data scene and the ideal data scene. This algorithm results in a position, flux point source list for each HCON image processed. Section 7 provides further explanation.

An algorithm to perform HCON merging was developed during first pass processing. It uses SNR ranking, and distance and flux matching criteria to combine the three redundant time-independent point source lists into one. The merge is also useful for sorting out spurious sources due to radiation hits, noise peaks, and mobile point source objects. Section 9 details the algorithm. HCON merging has not been applied to the delivered pass 1 point source list database.

4.0 DESCRIPTION OF DATA RECEIVED FROM IPAC

4.1 Survey Scan Coverage

MRC received sets of survey scan snips from IPAC in plates which were 6 degrees on a side, with a 5 degree separation between adjacent plate centers. Each plate contains snips of all the available survey scan data for the region bounded by the plate edges. Figure 4.1 is a map in galactic coordinates of the survey data which was re-processed. Table 4.1 is a list of the IPAC archive plate number and its center in equatorial coordinates. Use this table to identify the plate numbers for specific regions of interest. The plate number is key to locating images and point source lists in the product database.

4.2 Footprint Data and Geometry

The survey scan plates are "footprint" data. Footprint data is position tagged CRDD (Calibrated Raw Detector Data). Each data sample is provided as a triplet of x, y, and flux, where the x axis (units of arc minutes) is aligned with Declination, the y axis (units of arc minutes) is aligned with Right Ascension, and the flux units are W/m^2. The detector number and SOP/OBS number associated with each scan are provided. In each plate, the origin of the x,y grid is the plate's reference center in Equatorial Coordinates. For example, for one plate, the coordinate (0,0) in x,y data space is located at RA=273°, DEC=(-20°). A distance of one arc minute in x is equal to one arc minute in DEC. A distance of one arc minute in y is equal to one arc minute in RA. The scan snip plates are not flat projections of any kind; they are equivalent to small sections of the surface of a sphere. The x,y space is a spherical (Equatorial) coordinate system. At MRC's request, IPAC provided scan angles and noise estimates for each scan, but did not de-glitch the data, nor in any other way alter the flux stream. The data were not LAUNDERed. (LAUNDER is IPAC's scan data pre-processor. It estimates noise, removes radiation hits, and performs other data conditioning functions.)
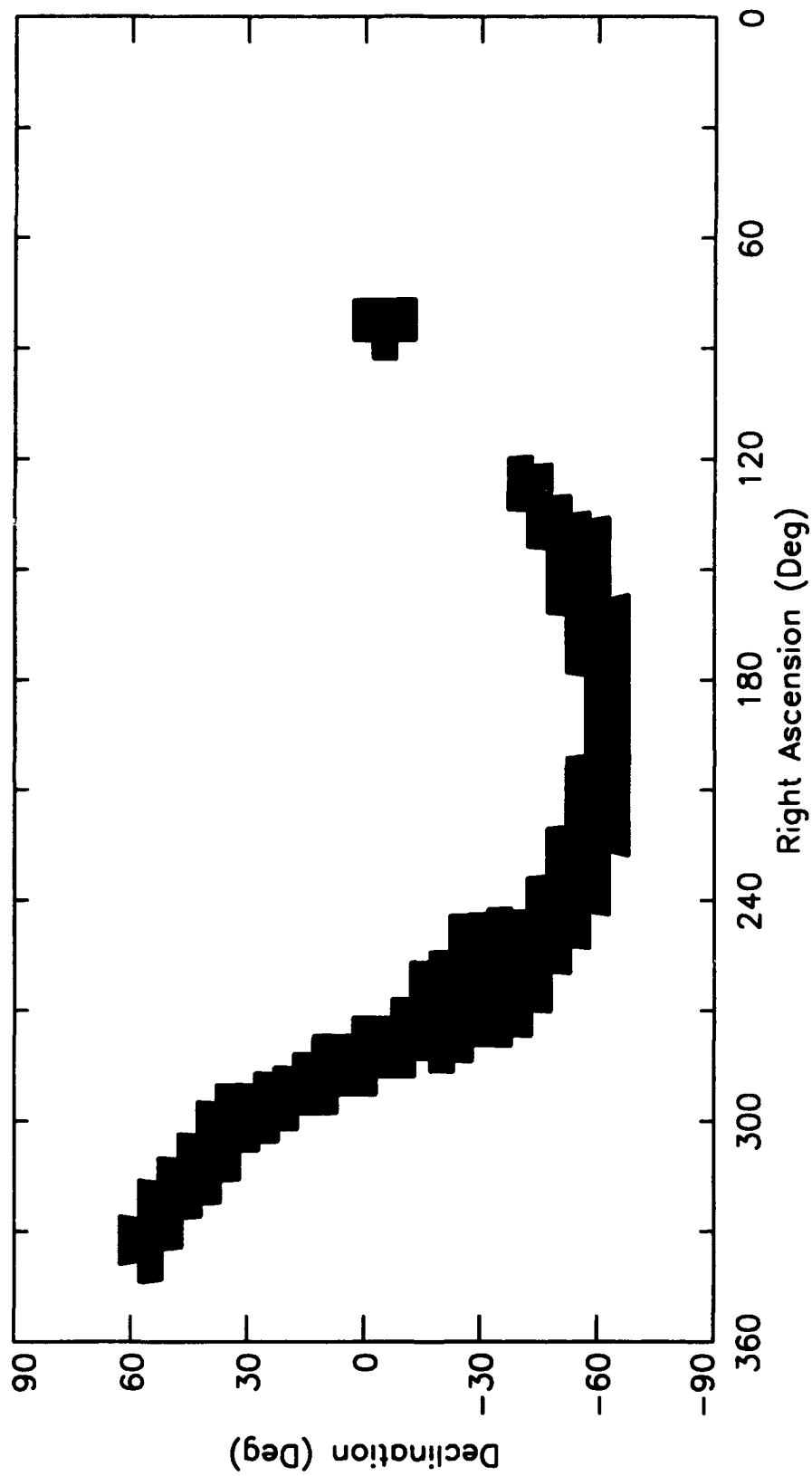
Figure 4.1 Spatial Coverage of the Galactic Plane Supplement

Table 4 (leftmost):

PLATE #	DEC°	RA°
1604	60.00	332.50
1566	55.00	338.25
1565	55.00	330.00
1564	55.00	321.75
1521	50.00	330.00
1520	50.00	322.50
1519	50.00	315.00
1471	45.00	322.00
1470	45.00	315.00
1469	45.00	308.00
1417	40.00	312.00
1416	40.00	305.50
1415	40.00	299.00
1360	35.00	306.00
1359	35.00	300.00
1358	35.00	294.00
1299	30.00	304.75
1298	30.00	299.00
1297	30.00	293.75
1235	25.00	302.50
1234	25.00	297.00
1168	20.00	299.25
1167	20.00	294.00
1166	20.00	288.75
1098	15.00	295.00
1097	15.00	290.00
1096	15.00	285.00
1025	10.00	290.00
1024	10.00	285.00
1023	10.00	280.00

Table 3:

PLATE #	DEC°	RA°
953	5.00	290.00
952	5.00	285.00
951	5.00	280.00
881	0.00	290.00
880	0.00	285.00
806	-5.00	275.00
735	-10.00	280.00
734	-10.00	275.00
733	-10.00	270.00
663	-15.00	280.00
662	-15.00	275.00
661	-15.00	270.00
660	-15.00	265.00
659	-15.00	260.00
592	-20.00	283.50
591	-20.00	278.25
590	-20.00	273.00
589	-20.00	267.75
588	-20.00	262.50
587	-20.00	257.25
523	-25.00	280.50
522	-25.00	275.00
521	-25.00	269.50
520	-25.00	264.00
519	-25.00	258.50
518	-25.00	253.00
517	-25.00	247.50
457	-30.00	276.00
456	-30.00	270.25
455	-30.00	264.50

Table 2:

PLATE #	DEC°	RA°
454	-30.00	258.75
453	-30.00	253.00
452	-30.00	247.25
395	-35.00	276.00
394	-35.00	270.00
393	-35.00	264.00
392	-35.00	258.00
391	-35.00	252.00
390	-35.00	246.00
335	-40.00	273.00
334	-40.00	266.50
333	-40.00	260.00
332	-40.00	253.00
331	-40.00	247.00
279	-45.00	266.00
278	-45.00	259.00
277	-45.00	252.00
276	-45.00	245.00
275	-45.00	238.00
227	-50.00	255.00
226	-50.00	247.50
225	-50.00	240.00
224	-50.00	232.50
223	-50.00	225.00
179	-55.00	247.50
178	-55.00	239.25
177	-55.00	231.00
176	-55.00	222.75
175	-55.00	214.50
174	-55.00	206.25

Table 1 (rightmost):

PLATE #	DEC°	RA°
136	-60.00	237.50
135	-60.00	228.00
132	-60.00	199.50
131	-60.00	190.00
130	-60.00	180.50
129	-60.00	171.00
128	-60.00	161.50
127	-60.00	152.00
126	-60.00	142.50
98	-65.00	220.00
97	-65.00	209.00
96	-65.00	198.00
95	-65.00	187.00
94	-65.00	176.00
93	-65.00	165.00
170	-55.00	173.25
169	-55.00	165.00
168	-55.00	156.75
167	-55.00	148.50
166	-55.00	140.25
214	-50.00	157.50
213	-50.00	150.00
212	-50.00	142.50
211	-50.00	135.00
261	-45.00	140.00
260	-45.00	133.00
259	-45.00	126.00
312	-40.00	123.50
313	-40.00	130.00

Table 4.1 IPAC plate numbers and their locations. (1950)

5.0 DATA CONDITIONING

5.1 Overview

Prior to image construction, the scan snip data plates are broken into quadrants (see Figure 5.1), and several operations are applied to the scans to prepare them for image construction.

In each quadrant, scan angles are calculated, and scans are sorted into "HCON" groups by SOP number and angle, and rotated to be aligned with the in-scan x axis. A noise value is estimated for each scan from the flux stream. Large scale extended emission is separated from the higher frequency point source signatures and noise. (Separate background and point source images are made from the separated flux stream.) The in-scan positions are phased so that the zero positions of all scans are at the middle pixel of a fixed scan length. Scan gaps are filled in with positions interpolated from the available data, and flux values which are flags. Figure 5.2 is a flowchart of the data conditioning processing.

5.2 "HCON" Sorting

For each quadrant plate, MRC's survey processing begins with sorting the scan snips by SOP and angle into 3 groups. Each group is called an "HCON" in the context of this project, and is destined to become an image. (In IRAS processing, "HCON" means "hours confirming", and refers to a scan of a region which occurs hours (within three SOPs) after the most recent scan there.) The MRC HCON sort has two goals. One is to group data close in time together in the same image. The other is to assure that the angles of scans that make up an image are sufficiently similar that the whole scan set can be considered parallel for purposes of image construction. Most scan snip plates divide neatly into three groups which are both isolated SOP groups, and nearly parallel angle scan sets. When there are more than three SOP groups or angle groups, the three largest sets were used, with scan angle boundaries as the primary limiter, and SOP number as a secondary limiter.

5.3 Scan Angle Calculations

Scan angles are calculated for each scan from the position tags. Each calculated scan angle is the average of 100 two-point angle determinations, each of which uses a slightly different set of 4/5 of the available samples.

5.4 Flux Units Conversion

Flux density units are converted from W/m^2 to Jy/sr. The conversion includes dividing the instrumental flux by 1.5939e13, and 5.6320e12 Hz, for the 12 and 25μm bands respectively. Instrumental flux was also divided by the detector solid angles. We used the
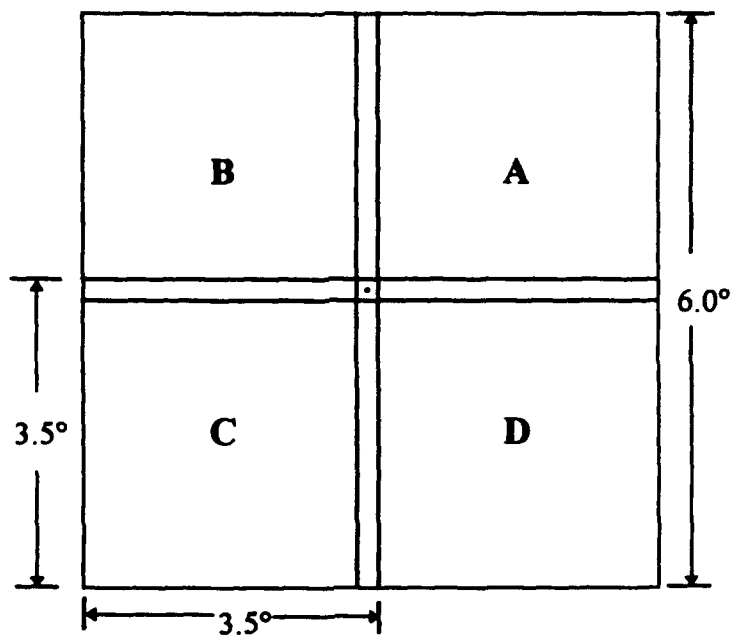
Figure 5.1 Definition of Quadrant plates relative to IPAC archival footprint plates. IPAC plates are 6° plates on 5° centers. MRC processed them in 3.5° quadrants, with .25° overlap on internal boundaries.

DATA CONDITIONING
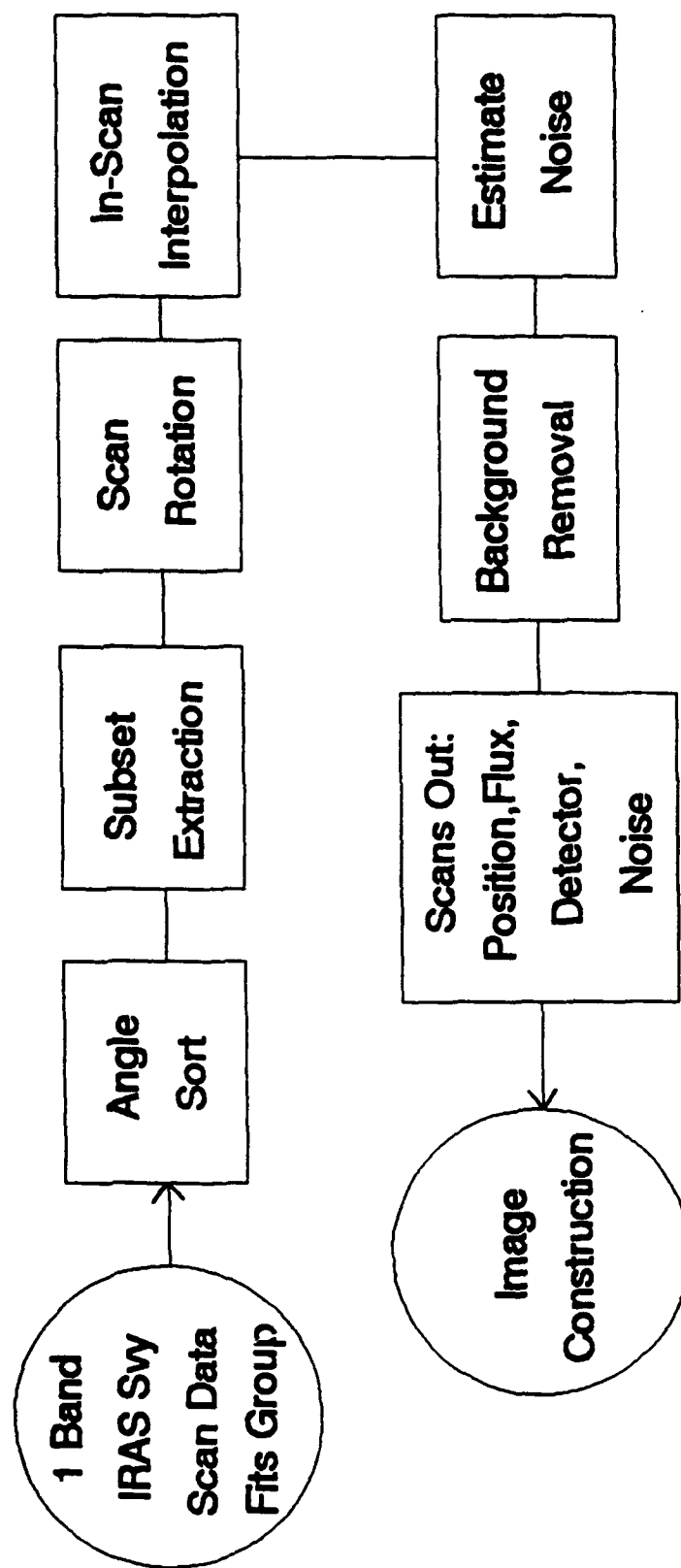
Figure 5.2 Survey Data Conditioning Flowchart.

solid angles reported in the IRAS Faint Source Survey Explanatory Supplement (pg. II-50). See notes relative to the bandpass values in section 11.2, Caveats.

5.5 Scan Rotation

In each quadrant plate, all the scans were rotated by the average angle of the scan set in that HCON to "near zero" degrees. This was done so the scans could be treated as columns in an array. The assumption that the scans are parallel greatly increases the speed of the image construction algorithm. Algorithm run time was a driving factor in this project because the data set which was processed was large. The parallel scan assumption contributes to position and flux uncertainties in the extracted sources. Figure 5.5 is a histogram of the scan angle spread in each quadrant plate. 80% of the data sets have an angle spread < 2.0°. 98% of the angle groups had a spread < 2.3°.

A simulation of the parallel scan assumption was performed to assess its effect on the positions and fluxes of extracted point sources. In a case where the scan length was 3.5° (876 samples) and the HCON group scan angle spread was 2.5°, the maximum error on in-scan position recovery was 15 arc seconds in the case of truly parallel scans and 18 arc seconds using the parallel scan assumption. The maximum error on cross scan position recovery was 120 arc seconds for truly parallel scans, and 137 arc seconds using the parallel scan assumption. The maximum ratio of extracted flux to true flux was 0.85 using the parallel scan assumption, compared to 0.97 for a truly parallel scan set. Measurements were made on 76 sources in a region with a source density of ~ 125 sources per square degree. The only variable in the simulation was the scan angle variations in the scan set. In one case all scans had a 0° scan angle. In the other case, the scans had angles that varied from -1.25° to 1.25°, but they were treated during image construction as if they were all parallel at 0°. The scans were spread over the 2.5° like a fan.

5.6 Noise Estimation

An estimate of the noise characteristics of each scan is made from the flux signature of each snip in a quadrant plate. The noise value is a single number per scan which represents one standard deviation of the data after high pass filtering. In this estimate, a three sigma envelope includes almost all the noise and excludes all point sources generally exceeding SNR=3. The noise estimate is derived from solving the imaging equation for the noise term, instead of the object, as is usually done. The imaging equation is:

$$d(x) = o(x) * p(x) + n(x),$$

where $d(x)$ is the data, or observed scan flux stream, $o(x)$ is the object observed by the telescope (sky), $p(x)$ is the observation system's point response function, and $n(x)$ is the noise. No attempt is made to separate out all the noise components which are present. The usual solution to the imaging equation is for an estimate of $o(x)$, and is in the form of

Scan Angle Bin Widths of HCON Quadrant Plates

Scan Angle Range per HCON Quadrant Plate (Degrees)
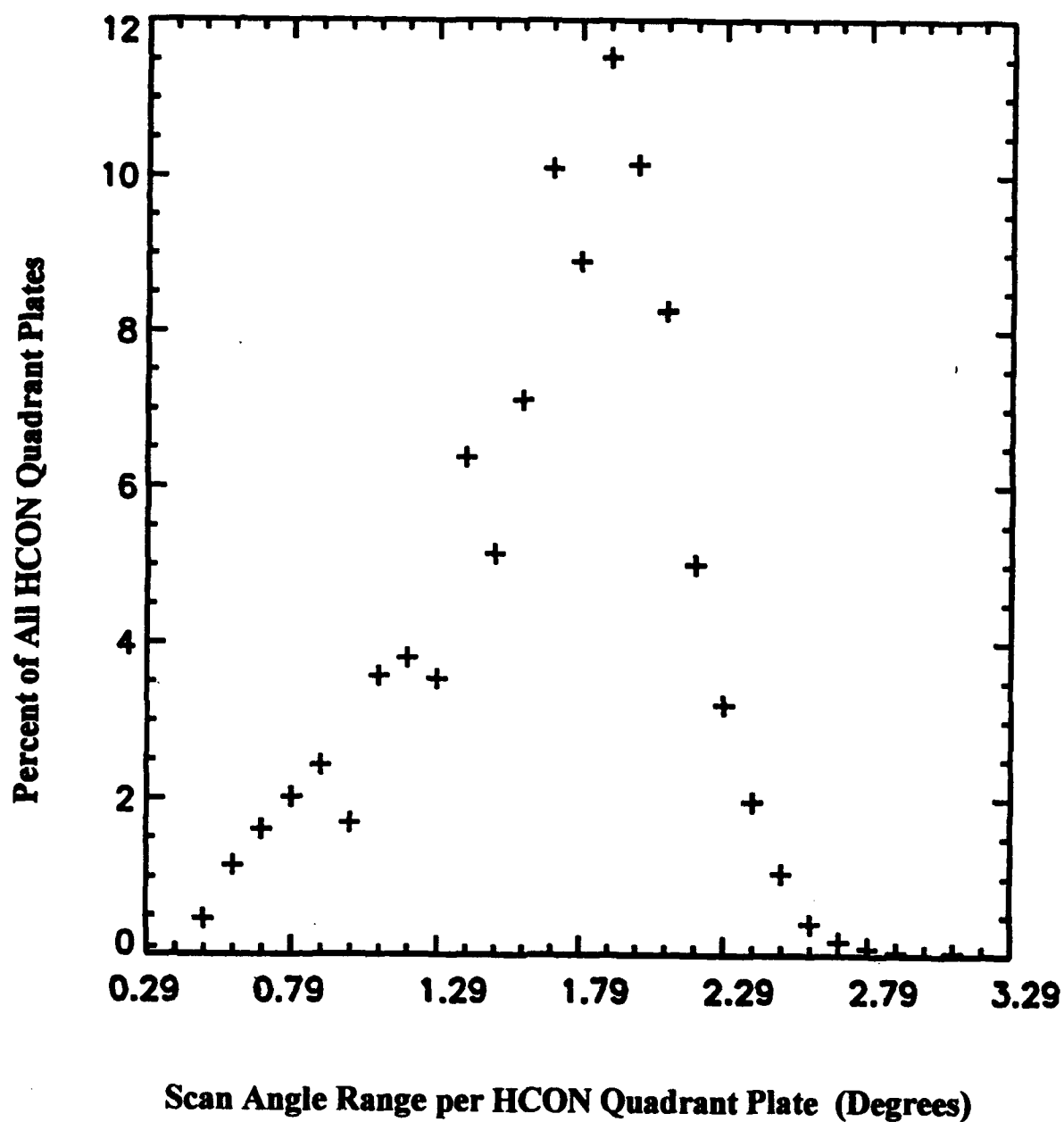
Figure 5.5   Histogram of Scan Angle Bin Ranges for All HCON Quadrant Plates.
A total of 2178 HCON Quadrant Plates are included. The histogram
binsize is 0.1°. The y axis is scaled to show the % of the total number
of plates in each angle bin.

a Wiener Filter. For the purposes of noise estimation, we solve for the filter function required to extract noise from the data. The Wiener Filter solution is

$$H(u) = \frac{|N(u)|^2}{|N(u)|^2 + |P(u)|^2} ,$$

where H(u) is the required filter in the frequency domain. $|N(u)|^2$ is the noise power spectrum, and $|P(u)|^2$ is the signal power spectrum (approximated by the prf, since it is the dominant component). The inverse transform of H(u) is trimmed to a 15 point, zero sum kernel.

Figure 5.6.1 shows the 15 point portion of h(x) used to high pass filter the scans and estimate noise from each scan. h(0:14) = [-0.35, -0.014, -0.126, 0.224, -0.136, 0.133, -0.546, 1.0, -0.546, 0.133, -0.136, 0.224, -0.126, -0.014, -0.35].

Figure 5.6.2 shows a typical survey scan which was filtered with the function in figure 5.6.1. Figure 5.6.3 shows the output of the application of the filter to the survey scan.

The standard deviation of the filter output is derived by iteratively excluding the peaks > 3 σ. The noise estimates arrived at in this manner are consistent with that of the survey flux stream in dark regions of the sky where noise is the dominant component of the scan signature. A typical noise value is 3.0e5 Jy/sr. For the "noisy" detectors 25 and 28, a typical noise value is 6.0e5 Jy/sr. These noise estimates are used in image construction, and in SNR reporting of extracted point sources.

5.7 Background Removal

An important aid to point source extraction is separation of the point sources from the diffuse background structure. MRC performed this operation on the scan data prior to image construction. Each scan was processed by a lower bound operator which was tuned to the signature of a point source. It works by forming a flexible baseline through the flux stream. The part of the flux signature above the base curve is the high frequency point source and noise content and the part below the baseline is the diffuse, extended emission. The base curve (background) is subtracted from the total flux stream, and the difference is the point source flux stream which will be image constructed and point source removed. The background flux stream is also made into an image. Both images are available as products in the Galactic Plane Supplement deliverables. Addition of the background and point source images produces an image which represents the flux stream before separation.

Background removal is a two step operation. In the first step, the base curve is generated by sliding a semicircle underneath the data. The base curve may rise with the data with the restriction that the data may not "pierce" the semicircle. That restriction together with the diameter of the semicircle (11 survey samples) keeps the base curve from following the

Noise Estimation Filter
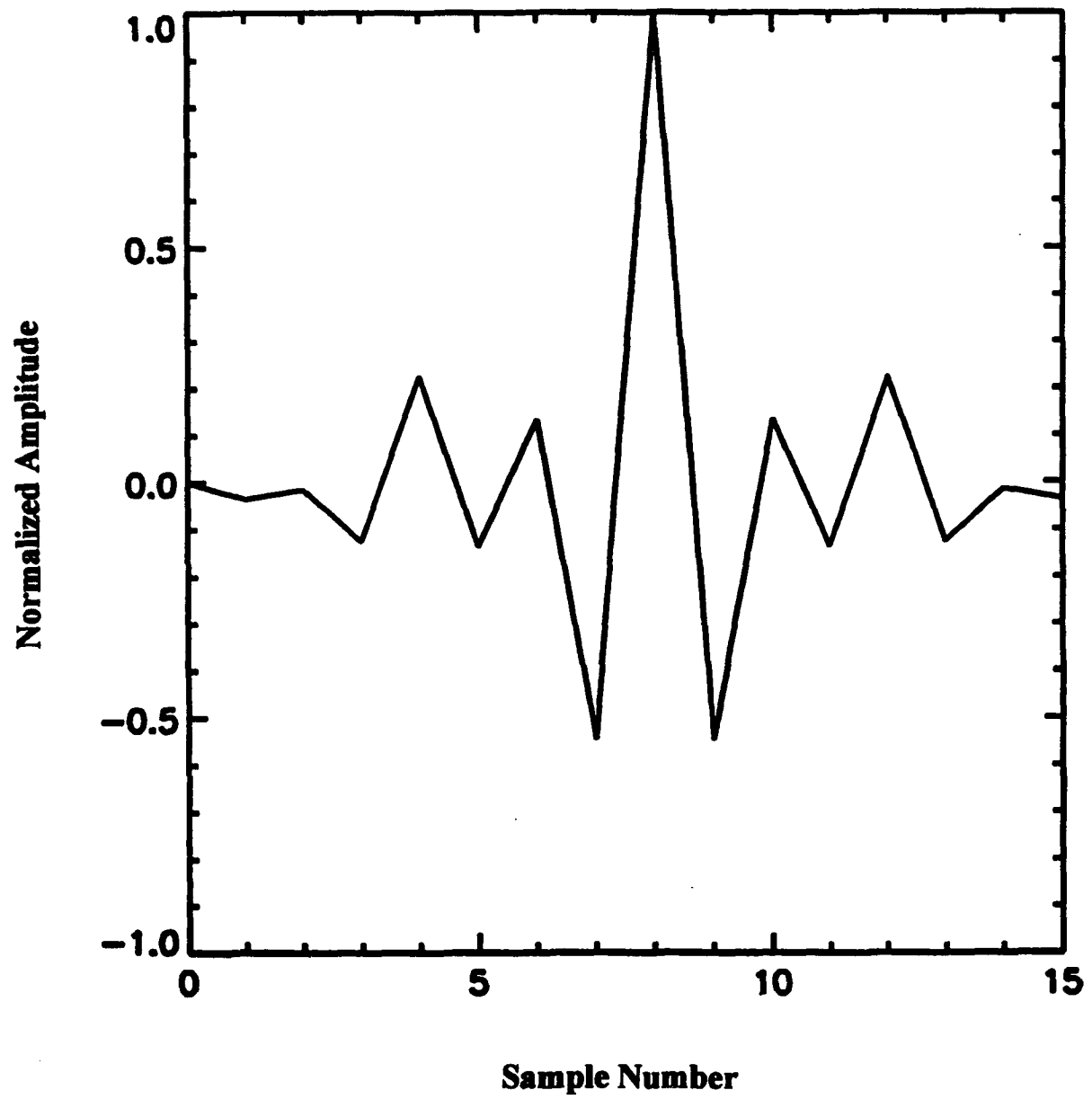
Figure 5.6.1 High Pass Filter Used to Estimate Noise Component of IRAS Survey Scans
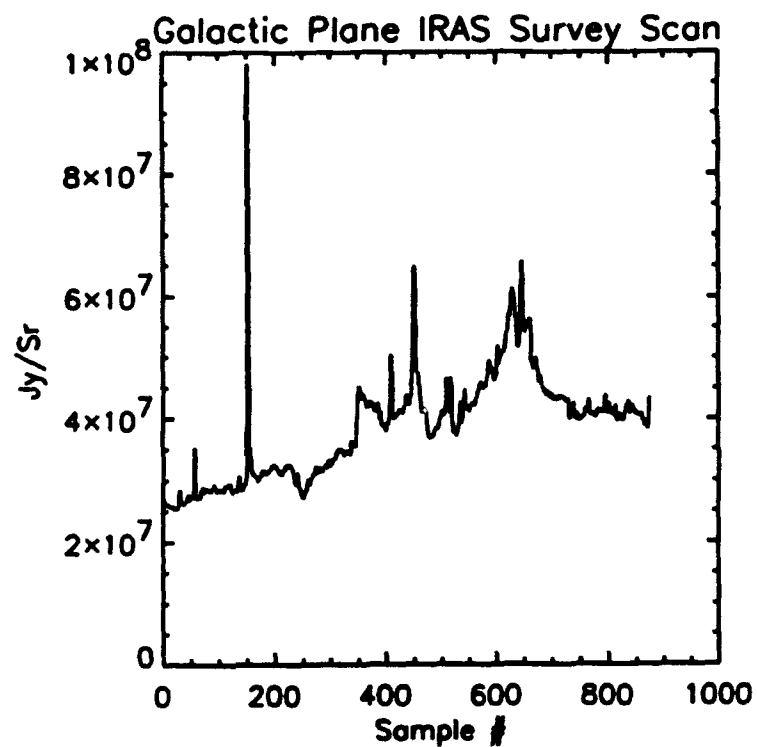
Figure 5.6.2   Galactic Plane Survey Scan as input to noise estimation filter.
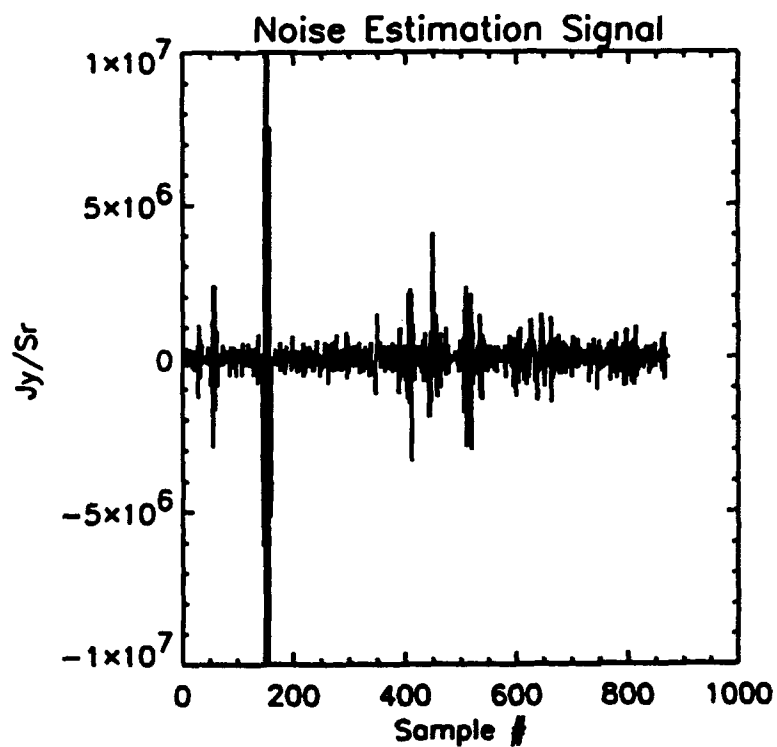
Figure 5.6.3   Signal out of noise estimation filter.

16

data up into a point source signature or a noise peak. The base curve is smoothed. This first pass base curve is subtracted from the original flux stream, leaving the point sources and noise rising from zero amplitude plus a small bias. This point source flux stream is the input to the next background removal step.

The second step of background removal applies another lower bound operator, a slope limitation called Differential Pulse Code Modulation. In this application of DPCM, a base curve is formed by following the data closely when flux is decreasing, and by following it closely when flux is increasing with the restriction that when the slope of the rising data exceeds a certain value, the base curve does not rise. The restriction causes the base curve to exclude point source signatures and noise. As you can see in Figures 5.7.1 and 5.7.2 the DPCM base curve is prone to direction specific ramping. To get an average base curve from this method, we run it in both directions, and average and smooth the two curves. Subtracting the cumulative (from both lower bound operators) base curve (shown in figure 5.7.3 under the input signal) from the input flux stream leads to a signal whose noise content is mostly above zero, instead of beating around zero. This leads to a small bias (~0.15 Jy) for the whole point source data base. Figures 5.7.4 and 5.7.5 show the effect of the background removal operation on a survey scan. In figure 5.7.5, the zero and $\pm 1\sigma$ noise lines are drawn through the signal.

An improvement was prepared for second pass processing which results in a base curve which has the noise beating around it. This "zero point" base curve is achieved by applying the lower bound operators to a smoothed copy of the original input flux stream. The base curve + 0.5 σ noise are subtracted from the original (unsmoothed) flux stream. The technique was refined using random noise signals as scan sample input. It's an improvement in three ways. The first is that the bias associated with the lower bound operator is no longer present in the point source images and lists. The second is that without the improved background removal, the magnitude of the bias associated with the lower bound operator is higher for the noisy detectors (also responsible for the prominent noisy stripes in the image data base). The third is that with an unbiased noise signature, it is easier to discriminate between faint sources and noise peaks. Figures 5.7.6 illustrates the result of using the improved background removal method. The delivered products were "first pass" processed only, and do not benefit from improved background removal.

5.8 In-Scan Phasing

Image construction is made significantly faster by reducing the complicated interpolation from two dimensions to one dimension (cross scan) through a small in-scan interpolation of the scan samples. Afterward, a cross scan cut through a group of scans could be treated as a row in an array. Samples are interpolated to be 0.24 arc minutes apart in scan. A modified cubic spline interpolation is applied to the flux stream. The modification restricts undershoots and overshoots which bounds the interpolated flux to remain between local minima and maxima of the original flux stream.

17
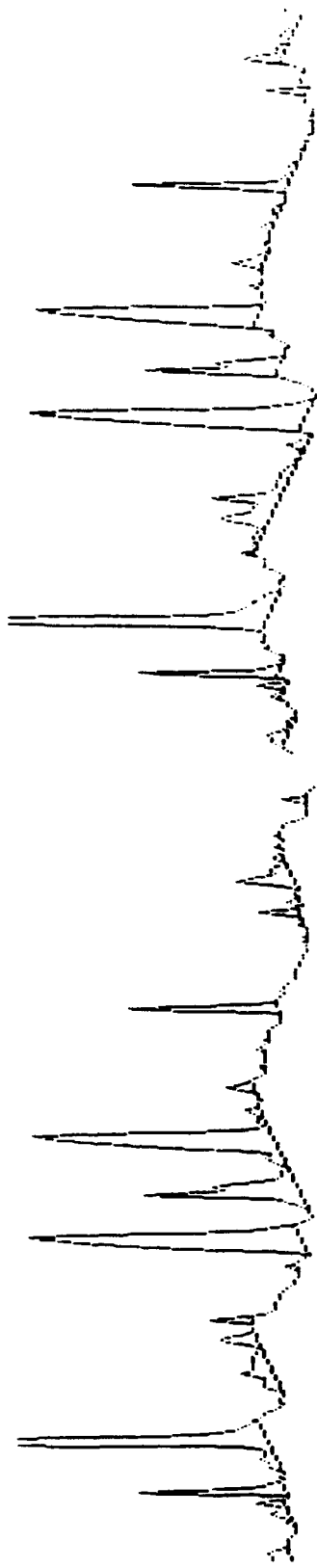
Figure 5.7.1 Scan Through Galactic Plane and Its Right-Scanning DPCM Signal

Figure 5.7.2 Scan Through Galactic Plane and Its Left-Scanning DPCM Signal

Figure 5.7.3 Scan Through the Galactic Plane and a Lower Bound Curve Which is the Smoothed Average of Right- and Left- Scanning DPCM Signals
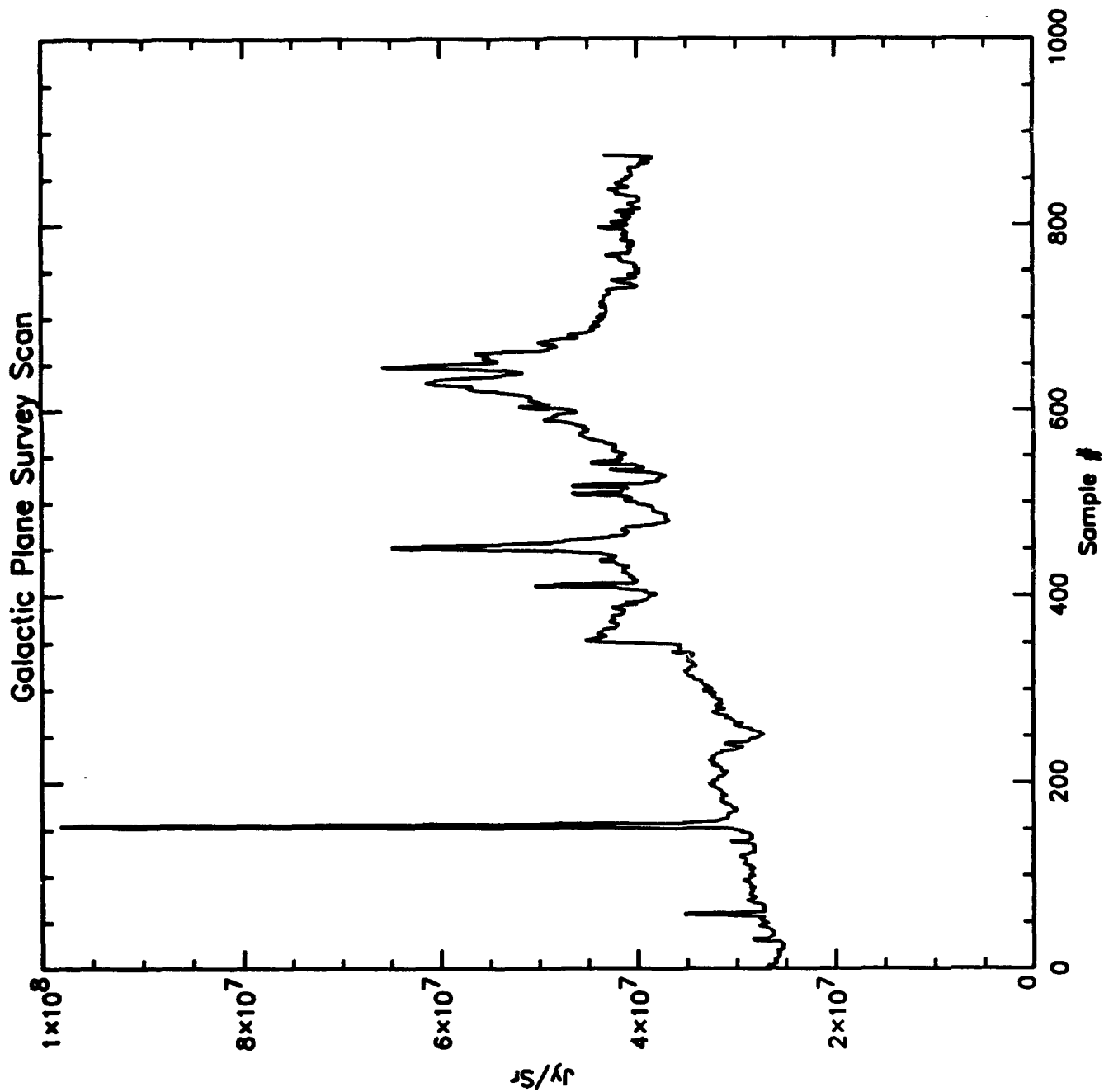
Figure 5.7.4 IRAS Survey Scan in the Galactic Plane; input to the Background Removal algorithm.

Pass 2 Background Removed Survey Scan

Jy/Sr

1×10^7 8×10^6 6×10^6 4×10^6 2×10^6 0 -2×10^6

0   200   400   600   800   1000

Sample #

Figure 5.7.6 High Frequency Content of the survey scan
of figure 5.7.4 after Pass 1 Background Removal
using *modified* lower bound operators.

Pass 1 Background Removed Survey Scan

$_{20}$ Jy/Sr

1×10^7 8×10^6 6×10^6 4×10^6 2×10^6 0 -2×10^6

0   200   400   600   800   1000

Sample #

Figure 5.7.5 High Frequency Content of the survey scan
of figure 5.7.4 after Pass 1 Background Removal
using lower bound operators.

5.9 Scan Gap Handling

Occasionally a scan snip has a gap in it. Our image reconstruction algorithm is made more efficient by assuming there will be no gaps in the scans. Gaps in position tags are filled in by the in-scan phasing interpolation. The x positions are interpolated from the pieces of the scan which are present. The y positions in gaps are assigned the average y position of the parts of the (rotated) scan which are present. Flux values associated with the filled in position tags are set to a flag value, and do not influence the image construction result.

6. Image Construction

6.1 Overview

Image construction was performed on 3.5 x 3.5 degree plates. *Two types of images were constructed* using either the "high frequency" or "low frequency" component of the scans as passed from the lower bound operator in the data conditioning algorithm. *Two sets of images were produced for each time take (HCON) and for each band:* point source-removed galactic plane background images and an associated set in which the point source signatures rise from a dark, relatively flat background.

The inputs to image construction, or regridding, from the data conditioning algorithm are (1) survey data scan snips, appropriately trimmed for the area of construction; (2) the set of unique per-scan noise values; (3) the set of average cross scan position tags (one for each scan); and (4) the set of detector numbers corresponding to each data scan. Prior to image construction, the data scans for a selected angle range and SOP range (i.e., HCON1, HCON2, or HCON3) pertinent to a specified 3.5 degree by 3.5 degree (in Equatorial coordinates) area of sky were sorted and rotated about their centers to the average scan angle. (See Caveats Section 11 for a description of this approximation and its implications on the results.) Each point of every scan has been "phased" slightly inscan by the Data Conditioning Algorithm to be at the exact pixel spacing of the output image. Each point is used as a data sample in the interpolation grid. As depicted in the Figure 6.1.A, the cross scan density of a typical HCON's set of scans is deficient by approximately 1:4 relative to the output image grid. An interpolated output image is formed using a Minimum Mean Square Error (MMSE) technique. The derivation for MMSE is contained in Section 6.5. Essentially a cross scan interpolation is used to populate the pixels of the output image. The input scans are overlaid on the interpolation grid, and for each grid cell the nearest 12 samples (3 inscan, 4 cross scan) and their noise values are used to compute a set flux weighting factors, $W=R^{-1}C$, where R is the autocorrelation function of the local data, and C is the cross correlation vector of the nominal point response function at the interpolation site and the local data (See Figure 6.1.B). The derived weights are normalized and applied to their respective data to compose each output image pixel, $\hat{s} = \sum_{i=1}^{12} w_i d_i$. The goal of this application of MMSE interpolation is to fill the output image with an accurate estimation of the sky convolved with a nominal point response function. Figure 6.1.C is a high level flowchart of the MRC image construction algorithm.

22
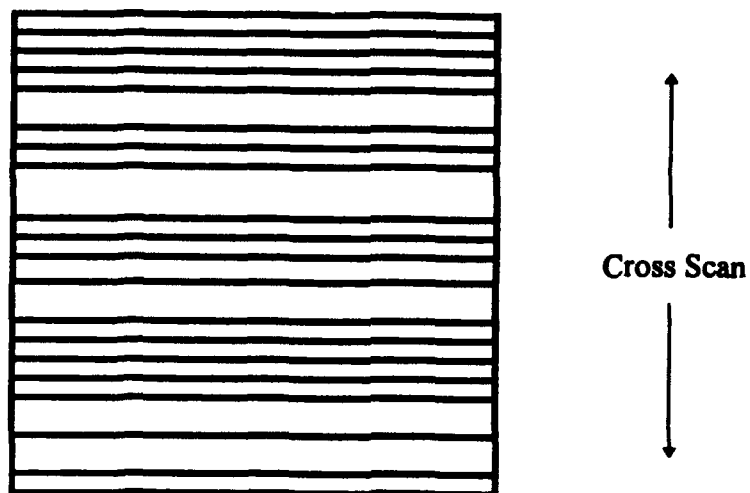
Figure 6.1.A Demonstration of
Cross Scan Undersampling

Cross Scan

Interpolation
Window

Interpolation
Site

Data Samples

x

Inscan ⟶
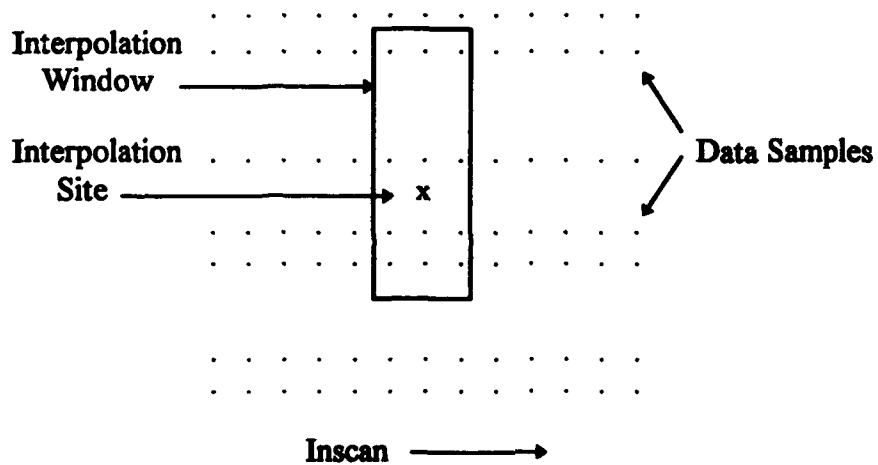
Figure 6.1.B Interpolation Window
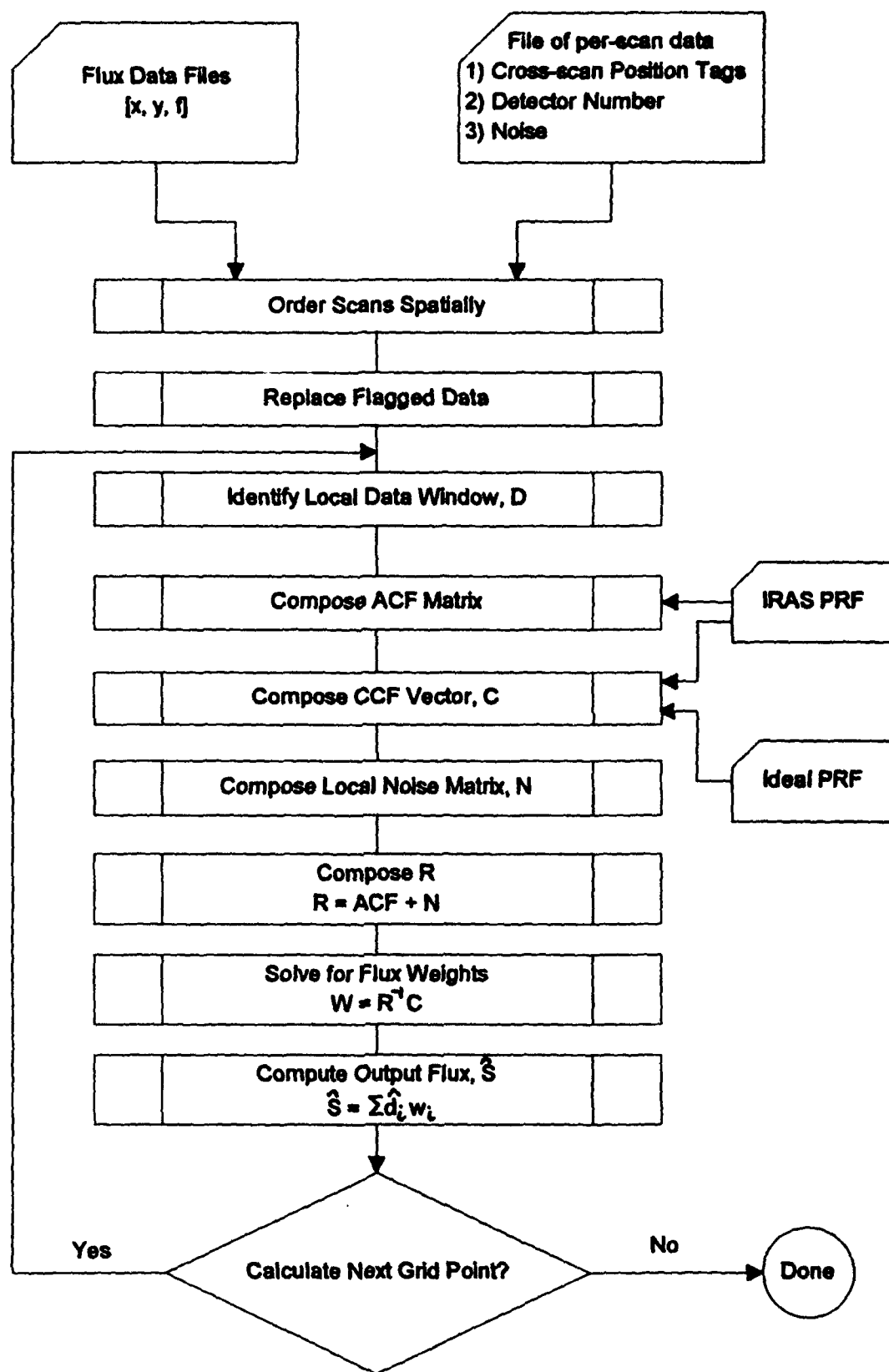
Figure 6.1.C   Image Construction Flowchart

6.2 Detector Profiles

The detector profiles used are those derived by M. Moshir, 1988 (private communication). For both 12μ and 25μ the IRAS detectors have considerably different response profiles (See IRAS Catalogs and Explanatory Atlases Explanatory Supplement, 1983, pp. IV-4, IV-5, for illustrations of the detector profiles) and sizes (see Figure 6.2.A for a drawing of the IRAS focal plane). The response profiles show prominent hot spots in different locations for each detector. The substantial differences between detectors necessitated using each detector profile in image construction. The Moshir detector profiles were extended slightly in the cross scan dimension by MRC. These extensions provided smooth roll off to zero.

Additionally, MRC constructed a nominal detector point response function in each band that represents the average of the detectors in the band, with imposed reflection symmetry about the center. (See Figures 6.2.B and 6.2.C for inscan and cross scan profiles of this nominal detector; these profiles have been area normalized). The final regridded image is an estimate of the sky convolved with this nominal or ideal point response function.

6.3 Flagged Data

Any unusable fluxes are passed from the data conditioning algorithm with a "flag" value. One of the first steps in image construction is to obtain a usable flux for each flagged value. If the flagged value is "straddled" cross scan by two usable data values, the flagged flux becomes the average of these two cross scan values. All other flagged data are assigned the value of their nearest valid cross scan neighbor. See Figure 6.3.A for illustrations of these cases.

6.4 Background Detector Bias Removal

For scans that went into composition of low-frequency background images *only*, a flat fielding (in addition to the data conditioning background removal) was performed. The purpose of this flat fielding was to remove any scan-to-scan differences due to detector bias.

An average value, av_0, for each scan was calculated, with flagged or negative data excluded from the average. For each scan av_0 is smoothed with a 15 point boxcar average to form av_s. A bias is calculated as the difference of these quantities:

$$bias = av_0 - av_s$$

This bias is subtracted from each flux value.
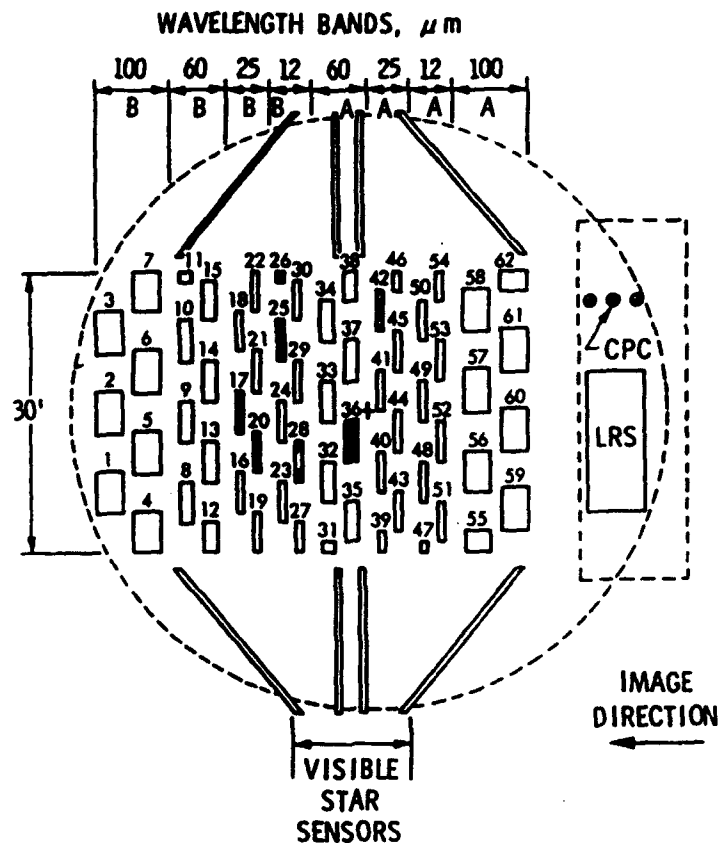
Figure 6.2.A. A schematic drawing of the IRAS focal plane. The numbered rectangles in the central portion each represent the field of view of a detector, filter and field lens combination. The image of a source crossed the focal plane in the Y direction as indicated. The filled-in detectors were inoperative while the cross-hatched detectors showed degraded performance during the mission.

[IRAS Catalogs and Atlases Explanatory Supplement (1983)]
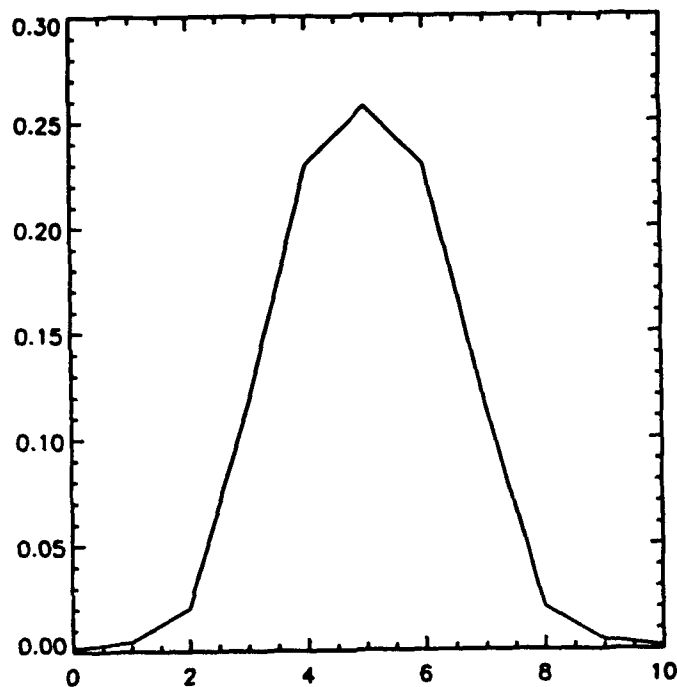
Figure 6.2.B An inscan trace of the ideal PRF.
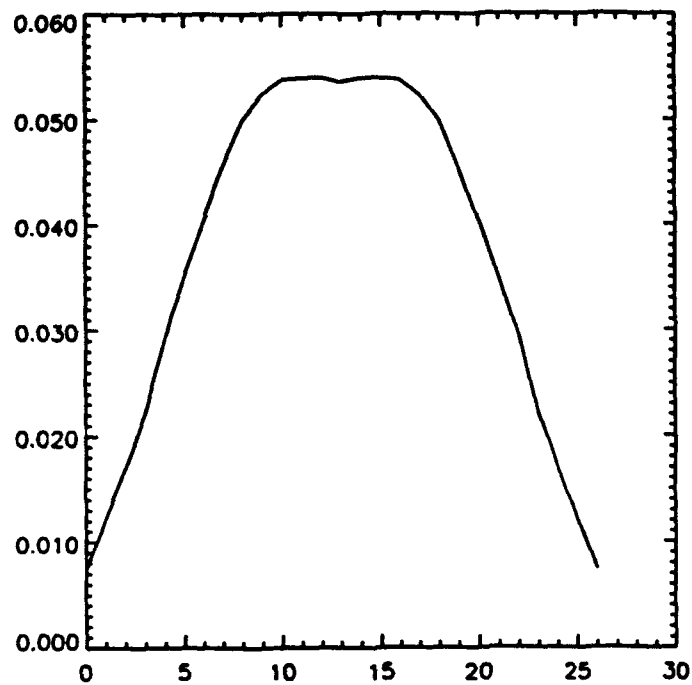
Figure 6.2.C A cross scan trace of the ideal PRF.
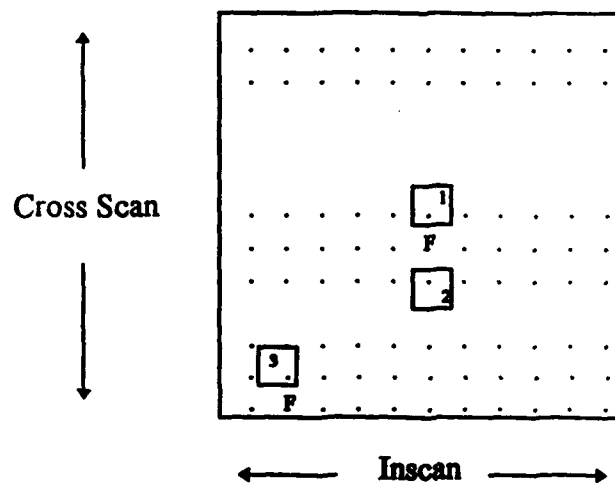
Figure 6.3.A. (a) The top flagged data value "F"
becomes the average of (1) and (2);
(b) The lower "F" is set to the value of (3).

6.5 Minimum Mean Square Error Formulation

6.5.1 Continuous Signal, One Detector

We begin the derivation for the simple case of a continuous signal and one detector. The observable is

$$d_1(x) = f(x) * p_1(x) + n_1(x), \tag{1}$$

where "*" denotes convolution, $f(x)$ is the underlying object, $p_1(x)$ is the point response function of detector 1, and $n_1(x)$ is the noise on detector 1. We represent a signal that would be seen by a noiseless, ideal detector

$$s(x) = f(x) * p_0(x), \tag{2}$$

where $p_0(x)$ is the ideal detector response. We use one-dimensional notation for simplicity, but the results extend easily to two dimensions.

We form an estimate for $s(x)$, by parsing $d_1(x)$ through a filter with impulse response $h(x)$. Thus the estimate is

$$\hat{s}(x) = d_1(x) * h(x). \tag{3}$$

We want to find $h(x)$.

In the spatial frequency domain, these equations become

$$D_1(u) = F(u)P_1(u) + N_1(u) \tag{4}$$

$$S(u) = F(u)P_0(u) \tag{5}$$

$$\hat{S}(u) = D_1(u)H(u). \tag{6}$$

If $H(u)$ is chosen to minimize the mean square error between $S(u)$ and $\hat{S}(u)$, then it must satisfy the orthogonality principle, that is, the data is orthogonal to the error:

$$< D_1^*(u)(S(u) - \hat{S}(u)) > = 0, \tag{7}$$

where "< >" denotes a statistical average. This yields:

$$< D_1^*(u)S(u) >=< D_1^*(u)\hat{S}(u) >$$

$$=< D_1^*(u)D_1(u) > H(u),$$

or

$$H(u) = \frac{< D_1^*(u)S(u) >}{< D_1^*(u)D_1(u) >}. \qquad (8)$$

The numerator of Equation (8) is

$$< D_1^*(u)S(u) >=< (F^*(u)P_1^*(u) + N_1^*(u))F(u)P_0(u))^2$$

$$= P_1^*(u)P_0(u) < |F(u)|^2 >, \qquad (9)$$

where the average over $N_1^*(u)F(u)$ is assumed to be zero. The denominator is, after a little work,

$$< D_1^*(u)D(u) >= |P_1(u)|^2 < |F(u)|^2 > + < |N_1(u)|^2 >. \qquad (10)$$

Thus, when we divide numerator and denominator by $< |F(u)|^2 >$, Equation (8) becomes

$$H(u) = \frac{P_1^*(u)P_0(u)}{|P_1(u)|^2 + < |N_1(u)|^2 > \left(< |F(u)|^2 > \right)^{-1}}$$

The noise-to-signal term is usually represented by a constant, NSR, and Equation (8) is

$$H(u) = \frac{P_1^*(u)P_0(u)}{|P_1(u)|^2 + NSR}. \qquad (11)$$

Note that the estimator for s(x) is, from Equation (3)

$$\hat{s}(x) = \int d_1(\sigma)h(x - \sigma)d\sigma,$$

which, for the estimate at x=0, is

$$\hat{s}(0) = \int d_1(\sigma)h(-\sigma)d\sigma. \qquad (12)$$

If we now define a weighting function w(x) to multiply $d_1(x)$ so as to get $\hat{s}(0)$, that is

29

$$\hat{s}(0) = \int d_1(x)w(x)dx$$
$$= \int d_1(\sigma)w(\sigma)d\sigma,$$

(13)

we see that, by comparing Equations (13) and (12),

$$w(x) = h(-x).$$

(14)

The Fourier transform of $w(x)$ is, therefore,

$$W(u) = H^*(u)$$

$$= \frac{P_1(u)P_0^*(u)}{|P_1(u)|^2 + NSR}.$$

(15)

We see that estimating $s(u)$ by a filter, $h(x)$, requires $H(u)$ to have $P_1^*(u)P_0(u)$ in the numerator; and that estimating $s(0)$ by a weighting function, $w(x)$, requires that $W(u)$ have $P_1(u)P_0^*(u)$ in the numerator. The two operations are entirely equivalent.

In the regridding procedure employed on the IRAS survey data, we solve for interpolation weights and multiply the observed data values by them. Thus, the conceptual approach is closer to selection of $w(x)$ than the selection of a filter $h(x)$.

6.5.2 Continuous Signal, Two Detectors

We set up this solution to guide the way to the discrete-sample, many-detector problem which is the realistic problem to be solved.

We have a second observable

$$d_2(x) = f(x)* p_2(x) + n_2(x),$$

(16)

with Fourier transform

$$D_2 = FP_2 + N_2$$

(17)

Here and in the following equation, we drop the u-dependence, (u). Our estimate for $\hat{s}$ now has two terms

$$\hat{s} = H_1 D_1 + H_2 D_2$$

(18)

and the orthogonality principal implies two equations:

$$< D_1 * (s - \hat{s}) >= 0$$

$$< D_2 * (s - \hat{s}) >= 0.$$

When we solve these for H_1 and H_2, we get, after a lot of work (see Appendix to Image Construction, following Section 6.7),

$$H = \begin{bmatrix} H_1 \\ H_2 \end{bmatrix} = R^{-1}C, \tag{19}$$

where C is a 2-element vector,

$$C = \begin{bmatrix} P_1^* P_0 \\ P_2^* P_0 \end{bmatrix}, \tag{20}$$

and R is a 2 by 2 matrix

$$R = \begin{bmatrix} |P_1|^2 + NSR_1 & P_1^* P_2 \\ P_2^* P_1 & |P_2|^2 + NSR_2 \end{bmatrix}. \tag{21}$$

Finally, when we reinstate the u-dependence, the estimator for s(u) is

$$\hat{s}(u) = P_0(u) \frac{D_1(u)P_1^*(u) + D_2(u)P_2^*(u)}{|P_1(u)|^2 + |P_2(u)|^2 + NSR}, \tag{22}$$

where we have set $NSR_1 = NSR_2 = NSR$ for simplicity in the derivation (See Section 6.6 for the actual treatment of NSR in the image construction algorithm.). We see that each data signal is multiplied by the complex conjugate of the corresponding detector response, that the sum of products is smoothed by $P_0(u)$, and that the result is divided by a real, non-negative function.

To give the spatial weighting operation corresponding to the $w(x)$ of the last section, we must define two weighting functions, $w_1(x)$ and $w_2(x)$. Then the estimate for $\hat{s}$ is

$$\hat{s}(0) = \int d_1(x) w_1(x) + \int d_2(x) w_2(x)$$

We deduce that $w_1(x)$ and $w_2(x)$ have Fourier transforms:

$$w_1(u) = \frac{P_1(u)P_0^*(u)}{|P_1(u)|^2 + |P_2(u)|^2 + NSR} \tag{23}$$

31

and

$$w_2(u) = \frac{P_2(u)P_0^*(u)}{|P_1(u)|^2 + |P_2(u)|^2 + NSR}. \qquad (24)$$

6.5.3 Sampled Data, Many Detectors

We now estimate $s(x)$ based on m data samples. The mth data sample is

$$d_m = g_m + n_m, \qquad (25)$$

where the noise samples, n_m, are assumed to be independent with zero mean and variance σ_m^2; and the signal samples, g_m, are samples of the ith detector taken at $x = x_m$. That is

$$\begin{aligned} g_m &= f(x) * p_m(x)\big|_{x=x_m} \\ &= \int f(\sigma) p_m(x_m - \sigma) d\sigma. \end{aligned} \qquad (26)$$

As before, the estimate for $s(x)$ is a weighted sum of the data. Thus

$$\begin{aligned} \hat{s}(x) &= w_1 d_1 + w_2 d_2 + \ldots + w_N d_N \\ &= \sum w_m d_m \\ &= \mathbf{D}^T \mathbf{W}, \end{aligned} \qquad (27)$$

where $\mathbf{D}^T$ is a vector of data samples

$$\mathbf{D}^T = (d_1 \quad d_2 \quad d_3 \quad \ldots \quad d_N), \qquad (28)$$

and $\mathbf{W}$ is a column vector of weights.

We select the weights to minimize the mean square error between $s(x)$ and $\hat{s}(x)$. The orthogonality principle implies

$$< \mathbf{D}(s(x) - \hat{s}(x)) > = 0$$

or, from Equation(27),

$$< \mathbf{D}s(x) > = < \mathbf{D}\mathbf{D}^T > \mathbf{W}, \qquad (29)$$

from which we can solve for $\mathbf{W}$.

First we examine the elements of the vector $< \mathbf{D}s(x) >$. The mth element is, from Equations (25) and (26),

$$< d_m s(x) > = < (g_m + n_m) s(x) >$$

$$= < (\int f(\sigma) p_m (x_m - \sigma) d\sigma + n_m) s(x) >. \qquad (30)$$

We assume that n_m is zero. Then using Equation (2) we have

$$< d_m s(x) > = < \int f(\sigma) p_m (x - \sigma) d\sigma \int f(\rho) p_0 (x - \rho) d\rho >$$

$$= \iint p_m (x_m - \sigma) p_0 (x - \rho) < f(\sigma) f(\rho) > d\sigma d\rho. \qquad (31)$$

We now assume that the statistical autocorrelation function of the object is impulsive. This is a valid assumption for objects which are point sources, randomly placed. Thus we set

$$< f(\sigma) f(\rho) > = E_0 \delta(\sigma - \rho),$$

where E_0 is a signal energy level. Then Equation (31) is

$$< d_m s(x) > = E_0 \int p_m (x_m - \sigma) p_0 (x - \sigma) d\sigma. \qquad (32)$$

We define the cross correlation detector p_m and the detector p_k, namely

$$R_{mk}(x) = \int p_m (\sigma) p_k (\sigma + x) d\sigma, \qquad (33)$$

and

$$< d_m s(x) > = E_0 \int p_m (\sigma) p_0 (\sigma + x - x_m)$$

$$= E_0 R_{m0}(x - x_m). \qquad (34)$$

Note that this element of the vector $< \mathbf{D}s(x) >$ is proportional to the overlap area between the mth detector placed at x_m and the ideal detector placed at x. The separation between them, $x - x_m$, and the functional form of the cross correlation are needed to perform the evaluation of Equation (34).

Now we evaluate elements of $< \mathbf{DD}^T >$. A typical term is

$$< d_m d_k > = < (g_m + n_m)(g_k + n_k) >$$

$$= < g_m g_k > + < n_m n_k >$$

33

$$= <g_m g_k> + \sigma_m^2 \delta_{mk}. \tag{35}$$

Again, we have assumed that signal and noise are independent.

The average in Equation (33) is calculated as above:

$$<g_m g_k> = <\int f(\sigma) p_m (x_m - \sigma) d\sigma \int f(\rho) p_k (x_k - \rho) d\rho>$$

$$= E_0 \int p_m (x_m - \sigma) p_k (x_k - \sigma) d\sigma$$

$$= E_0 R_{mk} (x_k - x_m). \tag{36}$$

When we divide both sides of Equation (29) by E_0 we get

$$\mathbf{W} = \mathbf{R}^{-1} \mathbf{C}, \tag{37}$$

where

$$\mathbf{C} = \frac{<\mathbf{D}s(x)>}{E_0}$$

$$= \begin{bmatrix} R_{10}(x_1 - x) \\ R_{20}(x_2 - x) \\ \vdots \\ R_{m0}(x_m - x) \end{bmatrix} \tag{38}$$

is the cross correlation vector; and

$$\mathbf{R} = \begin{bmatrix} R_{11}(0) + NSR_1 & R_{12}(x_2 - x_1) & \cdots \\ R_{21}(x_1 - x_2) & R_{22}(0) + NSR_2 & \cdots \\ \vdots & \vdots & R_{mm}(0) + NSR_m \end{bmatrix} \tag{39}$$

is the autocorrelation function matrix.

Calculation of the MMSE flux weights, $\mathbf{W}$, for each output pixel requires a noise value

$$NSR_m \equiv \frac{\sigma_m^2}{E_0} \tag{40}$$

Note that the noise-to-signal ratios appear only on the diagonal element of $\mathbf{R}$ and that $\mathbf{R}$ is a symmetric matrix. For example, from Equation (32),

$$R_{12}(x_2 - x_1) = \int p_1(\rho) p_2(\rho + x_2 - x_1) d\rho$$

$$= \int p_1(\rho' + x_1 - x_2) p_2(\rho') d\rho'$$

$$= R_{21}(x_1 - x_2).$$

Finally, we note the similarity of this solution for W to the solution, Equation (19), for H_1 and H_2. The similarities are evident when we compare Equations (20) and (21) with Equations (38) and (39).

6.6 Noise Implementation

The MRC data conditioning algorithm computes a noise value on a per-scan basis. A refinement of these values is performed to obtain "locally adaptive" noise values for use in computing MMSE flux weights, where W is the solution of

$$W = R^{-1}C.$$

R is the autocorrelation matrix with noise values in its diagonal elements. The calculation of the locally adaptive noise is done in a manner to run optimally with array usage in IDL.

The first step is the calculation of a *nsr* per point. The signal for each data point in the interpolation window is averaged and placed into an output vector, E:

$$E_j = \frac{\sum f_{ij}^2}{m} \quad ,$$

where

m = number of points in window (MRC has used 12 points),

$1 \leq j \leq$ number of points inscan,

$1 \leq i \leq m$.

E is then smoothed with a 9-point boxcar average.

The *nsr* value for point j is

$$NSR_j = \frac{\sigma^2_{MAX}}{E_j} \quad ,$$

where $\sigma^2{}_{MAX}$ is the square of the maximum noise value in the interpolation window. Note that depending on the spacing of the data, several points situated closely together cross scan can have the same *nsr*.

An approximation is used in solving for $\mathbf{R}^{-1}$, due to the excessive computation time involved in calculating and inverting an $m \times m$ matrix for each output pixel. Instead of doing the inversion on $\mathbf{R}$ with individual noise values added on its diagonal elements, four autocorrelation matrices are composed and inverted with *nsr* values of $0, .01, .1$ and 1. Each *nsr* falls in one of the ranges or bins between these four values, and the approximation of the ACF inversion is obtained by a linear weighting of the two calculated values that straddle the bin.

6.7 Discussion

We perform an interpolation of IRAS data scans to compose both high frequency images and low frequency or background images. We use a minimum mean square error procedure which requires knowledge of the following:

x = spatial point to be interpolated

$x_m = m^{th}$ spatial sample for data point d_m

$\sigma_m{}^2$ = noise variance on d_m

E_0 = local signal energy

$R_{mk}(x)$ = correlation function between detectors m and k

From these, we can calculate the C vector of Equation (38) and the R matrix and solve for the weight vector, $\mathbf{W}$. Then $\hat{s}(x)$ is

$$\hat{s}(x) = \sum w_m d_m.$$

APPENDIX TO IMAGE CONSTRUCTION

This appendix is referenced in the text prior to Equation (19) and contains the derivation of the autocorrelation and cross correlation elements.

Given

$$< D_1 (s - \hat{s}) >= 0$$

$$< D_1^* S >=< D_1^* (H_1 D_1 + H_2 D_2) >$$

$$= H_1 < D_1^* D_1 > + H_2 < D_1^* D_2 >$$

and

$$< D_2^* (s - \hat{s}) >= 0$$

$$< D_2^* S >=< D_2^* (H_1 D_1 + H_2 D_2) >$$

$$= H_1 < D_2^* D_1 > + H_2 < D_2^* D_2 >.$$

Form a matrix solution:

$$\begin{bmatrix} < D_1^* S > \\ < D_2^* S > \end{bmatrix} = \begin{bmatrix} < |D_1|^2 > & < D_1^* D_2 > \\ < D_2^* D_1 > & < |D_2|^2 > \end{bmatrix} \begin{bmatrix} H_1 \\ H_2 \end{bmatrix}$$

Evaluate

$$< D_1^* S >=< (P_1^* F^* + N_1^*) S >.$$

With independent noise this becomes

$$< D_1^* S >=< P_1^* F^* S >$$

$$=< P_1^* F^* P_0 F >$$

$$= P_1^* P_0 < |F|^2 >$$

and, similarly,

$$< D_2^* S >= P_2^* P_0 < |F|^2 >.$$

Now evaluate

$$< |D_1|^2 > = < (P_1^* F^* + N_1^*)(P_1 F + N_1) >$$

$$= |P_1|^2 < |F|^2 > + < |N_1|^2 >.$$

Simil

$$< |D_2|^2 > = |P_2|^2 < |F|^2 > + < |N_2|^2 >$$

$$< D_1^* D_2 > = P_1^* P_2 < |F|^2 >$$

and

$$< D_2^* D_1 > = P_2^* P_1 < |F|^2 >.$$

Division of both of the matrix equations by $< |F|^2 >$ yields **C** and **R** as defined in Equations (20) and (21), with

$$NSR_1 \equiv \frac{< |N_1|^2 >}{< |F|^2 >}$$

and

$$NSR_2 \equiv \frac{< |N_2|^2 >}{< |F|^2 >}.$$

7. Point Source Extraction

7.1 Introduction

We describe the point source extraction algorithm, which was used to extract the locations and amplitudes for point sources from each regridded image in the database. Figure 7.1.A gives an overview of the algorithm. The regridded or resampled data is partially deconvolved with an ideal point response function (PRF), which represents the average over all of the contributing detectors for a band. From this deconvolution, a sharpened image is formed. The locations of the local maxima in this sharpened image are used as the first estimate of the point source locations. A matched filter of the original regridded image is evaluated at these positions to give point source amplitudes which minimize the mean square error between the input, regridded data and the fit to the data. The output from the point source extraction algorithm is a list containing an entry for each point source: a coordinate pair and a corresponding amplitude. Sections 7.3 and 7.4 give the derivation for the point source extractor, with discussion of its use following in Section 7.5.

7.2 Model

The available data is a regridding of irregularly sampled data. The data conditioning and image construction algorithms are described earlier in Sections 5 and 6, but of major importance are the following three components achieved via application of these codes prior to point source extraction.

> (a) *Background removal*: this removes all low spatial frequency components in the original data, including any scan-to-scan fluctuations in the biases of individual scans.

> (b) *Interpolation*: in our application the inscan sampling is equal to the desired output image pixel size, so that each scan is, simply, phased to coincide with the desired output grid samples. The cross scan sampling, however, is inadequate by approximately 1:4, and a minimum mean square error (MMSE) algorithm is used to perform cross scan interpolation of data onto the output grid.

> (c) *Smoothing*: rather than trying to form an interpolated image of the underlying field of point sources, we try to form an interpolated image of the field of point sources convolved with an ideal PRF. Thus the regridded image "looks like" a conventional co-ad of the raw data. Each underlying point source takes the shape of an amplitude-scaled, shifted PRF.

POINT SOURCE EXTRACTION
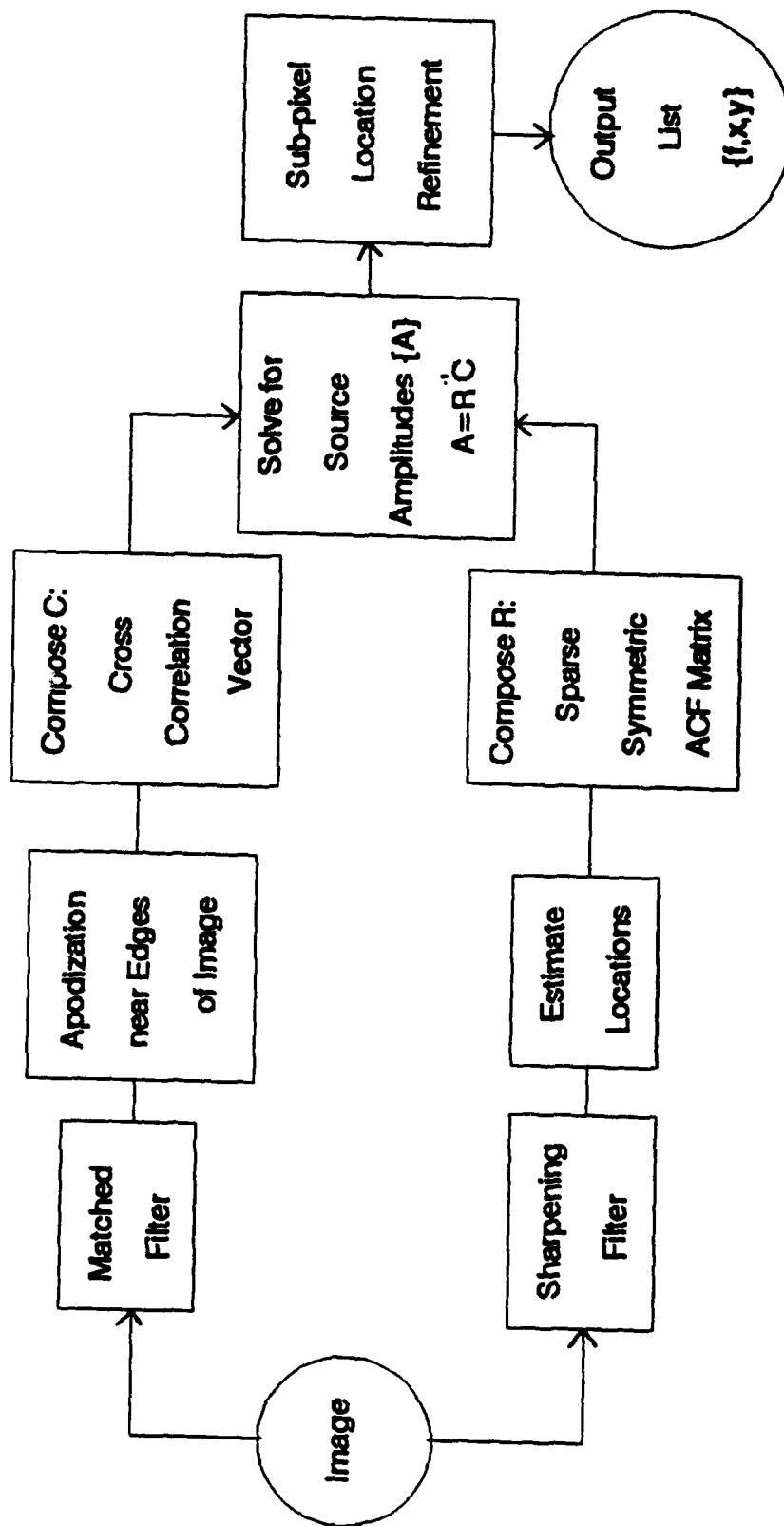
Figure 7.1.A Overview of the Point Source Extraction Algorithm.

With these preliminaries, we represent the data by a continuous signal $d(x)$, which is the interpolated image. (Note that one-dimensional notation will be used, although our results extend, almost without modification, to two dimensions.) Our model for the regridded data is

$$s(x) = \sum a_k p(x - x_k) ,\qquad\qquad (1)$$

where

a_k = amplitude of the kth star
x_k = location of the kth star

and

$p(x)$ = ideal PRF.

Our task is to select the amplitudes and locations which will force our model, $s(x)$, to look like the regrid, $d(x)$.

Figure 7.2.A is an example of a regridded image. This 12 micron image is 512 pixels on a side, sampled at .24 arc-min.

7.3 Point Source Locations

The point source locations are found by deconvolving the regrid with the ideal PRF and by finding the local maxima of the sharpened image. We use an iterative algorithm that estimates the underlying field of point sources, $s(x)$, convolves $s(x)$ with the ideal PRF, $p(x)$, and compares the convolution result with the regrid, $d(x)$. The difference is an error image, $e(x)$, that is used to refine the next iterate for $s(x)$.

Our metric is the mean square error between $d(x)$ and $\hat{d}(x)$, where

$$\hat{d}(x) = s(x)* p(x)\qquad . \qquad\qquad (2)$$

In Equation (2), "*" represents convolution. The metric is the mean square error,

$$mse = \int e^2(x)dx\qquad ,\qquad\qquad (3)$$

where $e(x)$ is the error image

$$e(x) = d(x) - \hat{d}(x)\qquad . \qquad\qquad (4)$$

The kth iterate for $s(x)$ is

41
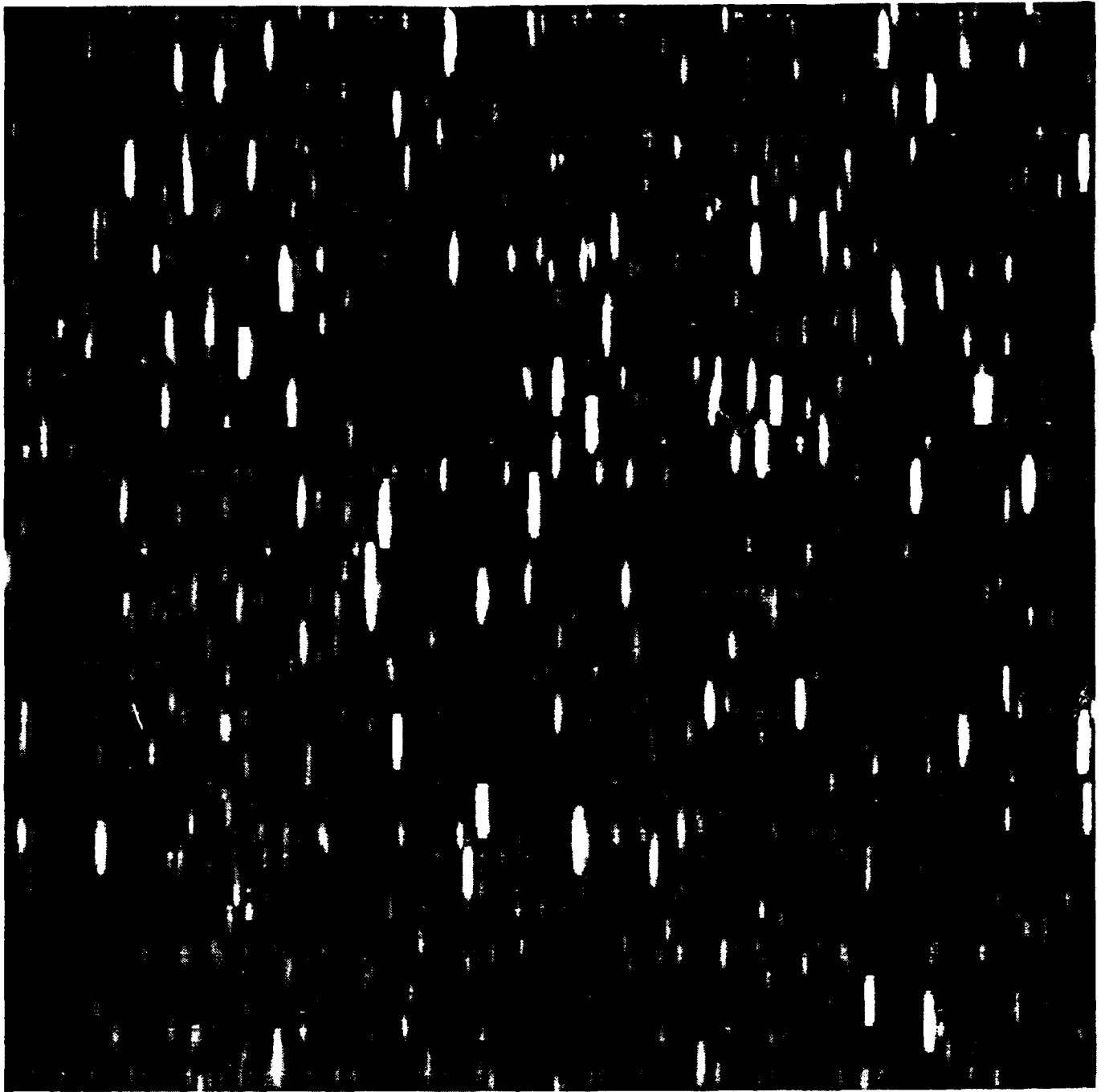
Figure 7.3.A. Regridded Data

$$s^k(x) = s^{k-1}(x) + b\,g(x) \qquad , \qquad \qquad (5)$$

where $g(x)$ is the gradient image and b is a (scalar) step size. The gradient is given by

$$g(x) = e(x) * p(x) \qquad , \qquad \qquad (6)$$

and the step size is

$$b(x) = \frac{\int e(x)q(x)dx}{\int q(x)q(x)dx} \qquad , \qquad \qquad (7)$$

where $q(x)$ is

$$q(x) = g(x) * p(x) \qquad . \qquad \qquad (8)$$

These formulae for $g(x)$ and b are proved in the Appendix to Point Source Extraction, which follows Section 7.5.

At each iteration, several constraints are imposed on the images. Basically, $s^k(x)$ is required to be non-negative. Thus, we impose this constraint after the calculation in Equation (5); and we constrain the gradient such that, if $s^{k-1}(x)$ is already zero, we do not allow $g(x)$ to go negative. Note that such constraints do not change our formulae: Equation (7) for the step size is valid for any gradient; and Equation (5) for the gradient is valid for <u>any</u> error image.

The resulting algorithm is called, generically, constrained iterative deconvolution. The properties of these algorithms are described in several papers, including Biemond, et. al., 1990. The major benefits of the constraints are that

      (a) we impose a known positivity constraint on the amplitudes of point sources, and
      (b) the deconvolution does not produce the dramatic ringing and side-lobe holes that often appear with application of unconstrained iterative deconvolution algorithms.

The goal of our deconvolution is to identify candidate locations for the field of point sources. For isolated sources, this is accomplished after just one or two iterations. After experimentation with the number of sharpening iterations, we find that most others are resolved in ten iterations. (Use of more than approximately ten iterations leads to an unrealistic number of candidate point sources.) After these ten sharpening iterations, we find the locations with a local maximum criterion.

In Figure 7.3.B we show the estimated star field after ten iterations of the sharpening algorithm have been applied to the image depicted in Figure 7.3.A. At each peak in this
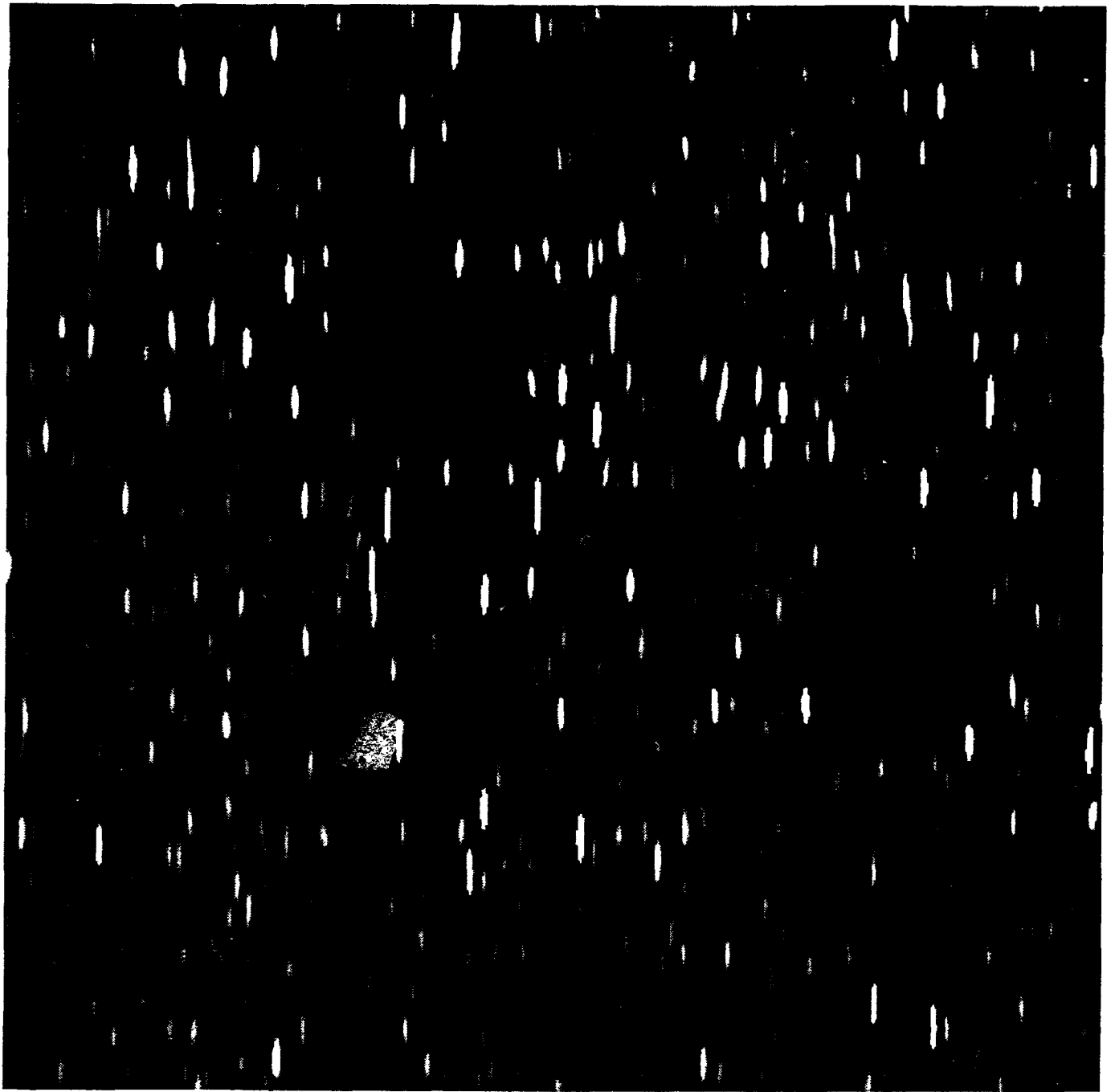
Figure 7.3.B.   Sharpening Filter Output

44

image, we locate the position of a candidate point source to form a set $\{x_k\}$ of point source locations.

7.4 Point Source Amplitudes

The data is the regridded image, $d(x)$, as represented by the image in Figure 7.3.A. We have a set $\{x_k\}$ of candidate locations from the location algorithm described in Section 7.3. Now an estimate to the point source field is formed,

$$\hat{s}(x) = \sum a_k \delta(x - x_k) , \qquad (9)$$

which places a point source with amplitude a_k at location x_k. Then an estimate to the observed data, $d(x)$, is

$$\hat{d}(x) = \hat{s}(x) * p(x)$$
$$= \sum a_k p(x - x_k) \qquad (10)$$

This is the same model we described in Equation (1).

The x_k's are fixed by source extraction so we only have to estimate the amplitudes. These are chosen to minimize the mean square error , mse, between $d(x)$ and $\hat{d}(x)$. The mse is

$$mse = \int \left[d(x) - \hat{d}(x) \right]^2 dx$$
$$= \int \left[d(x) - \sum a_k p(x - x_k) \right]^2 dx \qquad (11)$$

We differentiate mse with respect to a_k and set the result to zero. This yields

$$-2 \int \left[d(x) - \sum a_k p(x - x_k) \right] p(x - x_k) dx = 0$$

or

$$\sum a_j \int p(x - x_j) p(x - x_k) dx = \int d(x) p(x - x_k) dx \quad . \qquad (12)$$

We define the scalar r_{kj} as

$$r_{kj} = \int p(x - x_j) p(x - x_k) dx \qquad (13)$$

and another scalar c_k as

$$c_k = \int d(x) p(x - x_k) dx \qquad . \qquad (14)$$

With this notation Equation (12) becomes

$$\sum r_{kj} a_j = c_k$$

or, in matrix form,

$$\mathbf{R\,A} = \mathbf{C} \qquad . \qquad (15)$$

The solution for the vector **A** is, at least in principle,

$$\mathbf{A} = \mathbf{R}^{-1}\mathbf{C} \qquad . \qquad (16)$$

To explore this solution, we first examine Equation (13). This is simply the autocorrelation function of the PRF, sampled at $(x\text{-}x_k)$. That is, if we define the autocorrelation function

$$R(x) = \int p(\sigma) p(x + \sigma) d\sigma \qquad , \qquad (17)$$

then

$$\begin{aligned}
R(x_j - x_k) &= \int p(\sigma) p(x_j - x_k + \sigma) d\sigma \\
&= \int p(x - x_j) p(x - x_k) dx
\end{aligned} \qquad (18)$$

which is r_{kj} as in Equation (13).

Next we examine Equation (14). This is the correlation of $d(x)$ and $p(x)$, sampled at $x = x_k$. Thus, define

$$c(x) = \int d(\sigma) p(\sigma - x) d\sigma \qquad (19)$$

and it is obvious that Equation (14) is Equation (19) sampled at $x = x_k$. Note that $c(x)$ has Fourier transform

$$C(u) = D(u)\, P^*(u) \qquad . \qquad (20)$$

Since $P^*(u)$ is sometimes called the matched filter for $p(x)$, we call $c(x)$ the matched filter image, with $d(x)$ being the input image and $p(-x)$ the point response function. Figure 7.4.A is the matched filter image of Figure 7.3.A.
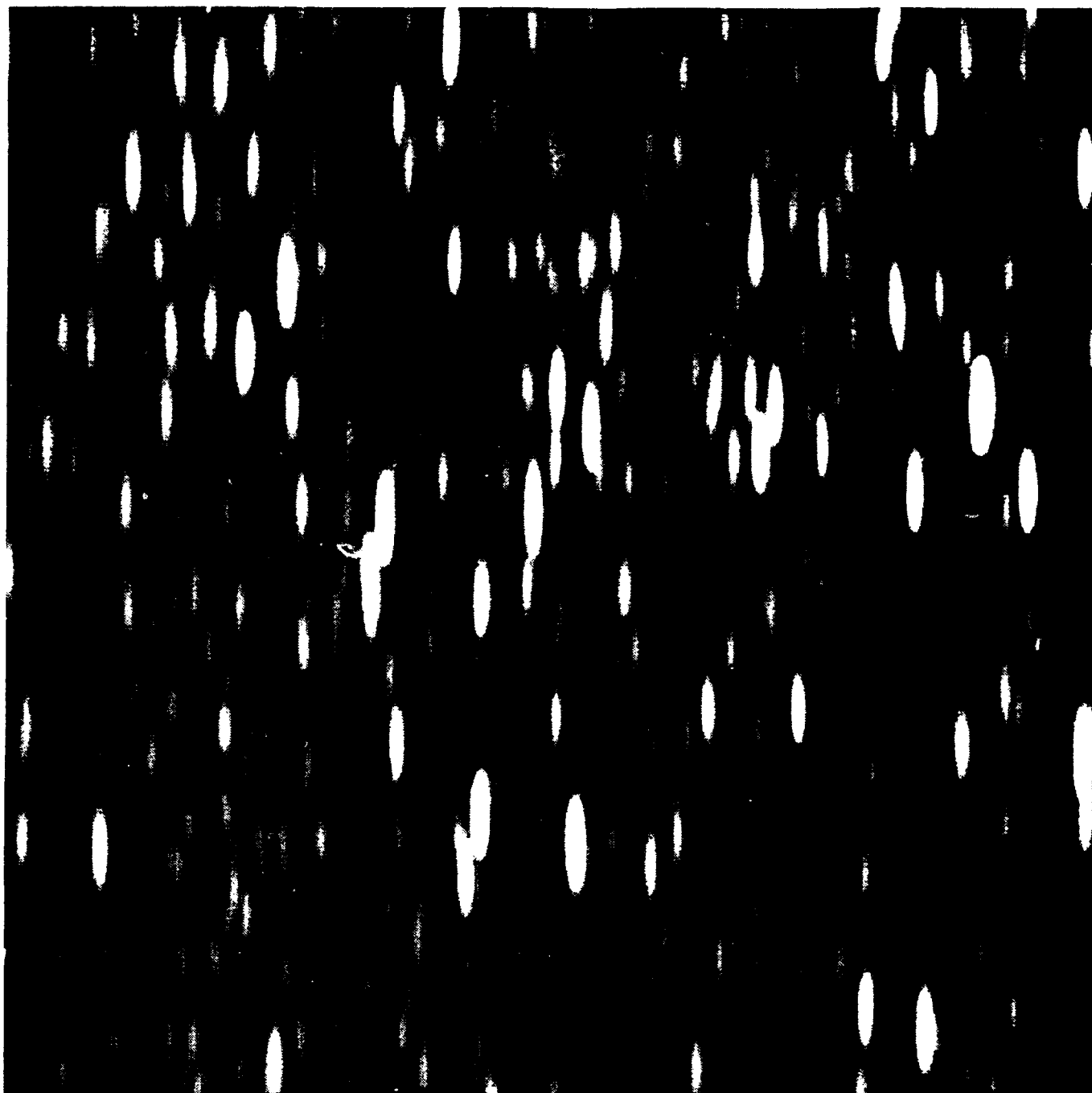
Figure 7.4.A.   Matched Filter Output

From these considerations we see that one should convolve the data with the 'transpose" of the ideal PRF. This both filters the noise and restores any distorting spatial-frequency-phase introduced by the data-taking system. This matched filtered image is sampled at the locations specified by $\{x_k\}$ to form a vector $\mathbf{C}$.

Next one samples the autocorrelation function of the PRF at the sample intervals $\{x_j\text{-}x_k\}$ to form the square matrix $\mathbf{R}$. This matrix has many ideal properties, including the following:

(1) It is symmetric, $\mathbf{R} = \mathbf{R}^T$, since the autocorrelation function is symmetric.

(2) It is sparse, since the only non-zero elements will occur for those point source locations close enough to fall within the support of the autocorrelation function. Thus, if $R(x) = 0$ for $x = x_0$

$$R_{kj} = 0 \quad if \quad |x_j - x_k| > x_0 \quad . \tag{21}$$

(3) The matrix is *positive definite*, which guarantees that it has an inverse. We prove this: by definition, a matrix is positive definite if and only if for every sequence $\{x_k\}$ not identically zero

$$sum = \sum x_k r_{kj} x_j > 0 \quad .$$

But

$$sum = \sum\sum x_k \int p(x - x_k)p(x - x_j)dx \, x_j$$

$$= \int \sum x_k p(x - x_k) \sum x_j p(x - x_j)dx$$

$$= \int \left[\sum x_k p(x - x_k)\right]^2 dx$$

which is positive for any non-zero $p(x)$. QED

Despite all these favorable qualities the solution of Equation (16) is not a simple matter. First and foremost is the size of $\mathbf{R}$. Consider that a typical field of point sources as processed may contain several thousand sources. If the number of sources in the field is 3000, for example, this means that $\mathbf{R}$, a square matrix, will be a *3000 x 3000* matrix that has to be inverted. Also, the point source amplitudes must be non-negative, which is an additional consideration when solving for $\mathbf{A}$.

This is a classical deconvolution problem, but of considerably reduced dimensions. That is, a typical deconvolution problem is a *512 x 512* image with *260K* samples. Our data (quantity $\mathbf{C}$) has only about *3000* samples in a typical field. Thus we are led to try a direct inversion of the matrix, in the following way.

First, we partition the matrix into blocks of 150 by 150. We find that these blocks will be non-zero only if centered on the diagonal of $\mathbf{R}$, provided we order the point source locations. We find that a simple rectangular ordering will do, if we use the long axis of the PRF as the "inside" dimension for the ordering. Then we solve a smaller matrix problem with only the 150 nearest point sources. This is repeated over all point sources, with a 10-point source overlap between blocks.

For each sub-block, we solve $\mathbf{A}=\mathbf{R}^{-1}\mathbf{C}$ for the sub-block. If any solution value for a_k goes negative, we eliminate that location, reconstitute $\mathbf{R}$ and $\mathbf{C}$, and solve again for $\mathbf{A}$. We repeat this until all $\mathbf{A}$'s are non-negative. Typically this takes only two or three iterations. When we have all A-vectors solved, we average them in the overlap regions, with a simple triangular weighting. This is our set of fluxes for the field of point sources.

In a final step, we refine the point source locations by returning to the sharpened image (described in Section 7.3) and performing a sub-pixel location estimation. We use a simple bilinear interpolation of the sharpened image. In Figure 7.4.B we show the estimated field of point sources, and in Figure 7.4.C we show the estimated data, a convolution of the star field with the PRF. The estimated data in Figure 7.4.B is to be compared to the original regridded image in Figure 7.3.A., noting that the estimated data has been rescaled to show more details of the fainter point sources.

7.5 Discussion

The point source extraction method outlined is a fairly general technique to find locations and amplitudes for point sources on regularly sampled data. We sharpen the image with an iterative deconvolution method and identify local maxima as candidate point source locations. Then we use these locations and go back to the original data to calculate the amplitudes. The calculation uses a matched filtered version of the data and requires inversion of a large matrix whose entries are samples of the autocorrelation function of the PRF. The inversion procedure sorts out the amplitudes associated with point sources that are close enough to interact with each other. We reject candidate point sources with negative amplitudes and recalculate the remaining point source amplitudes based on a reduced-size matrix. Finally, we refine the locations to account for the sub-pixel locations of point sources. The output of the point source extractor is a list of point source locations and their respective fluxes.
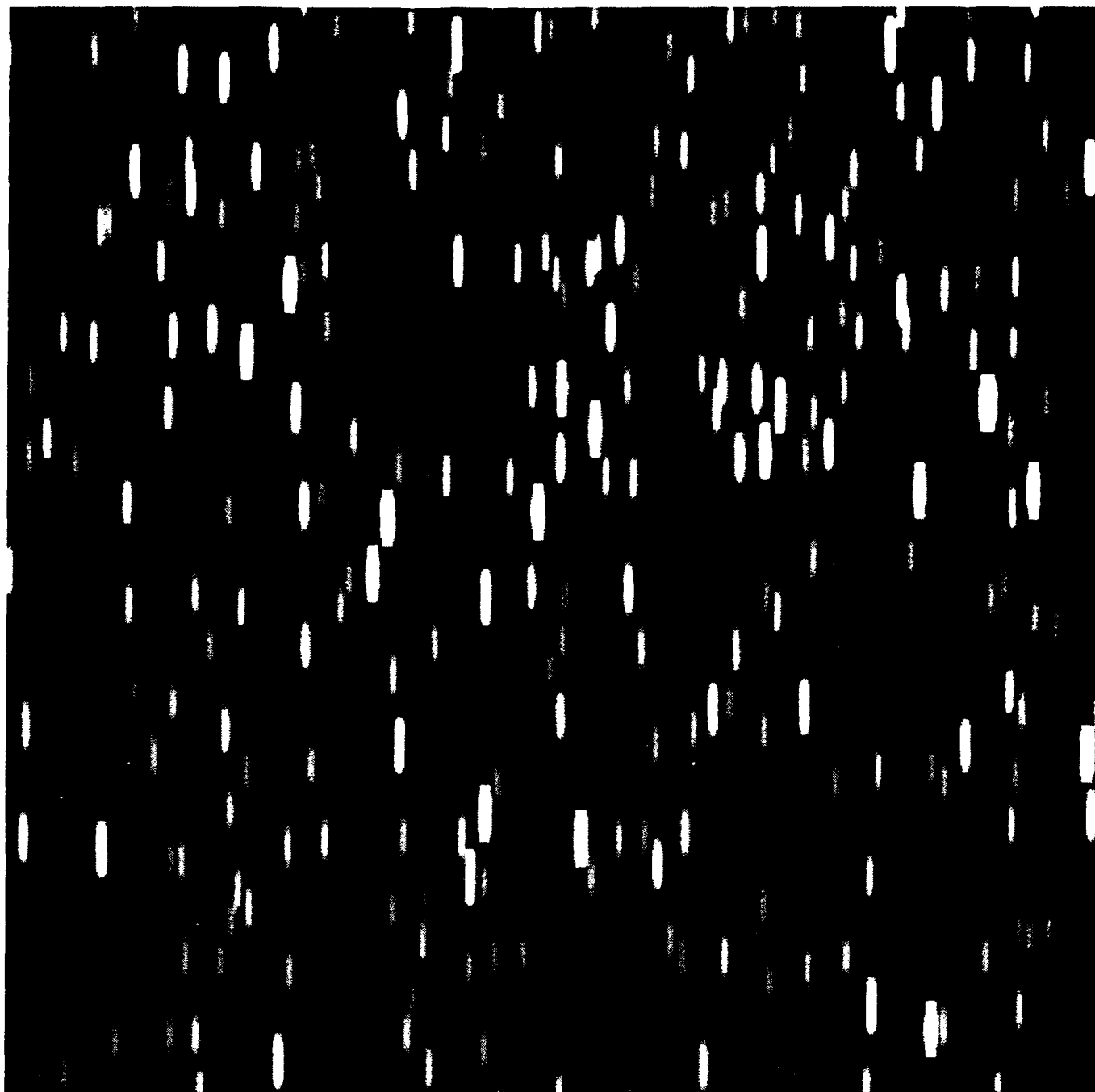
Figure 7.4.B.   Data Estimate
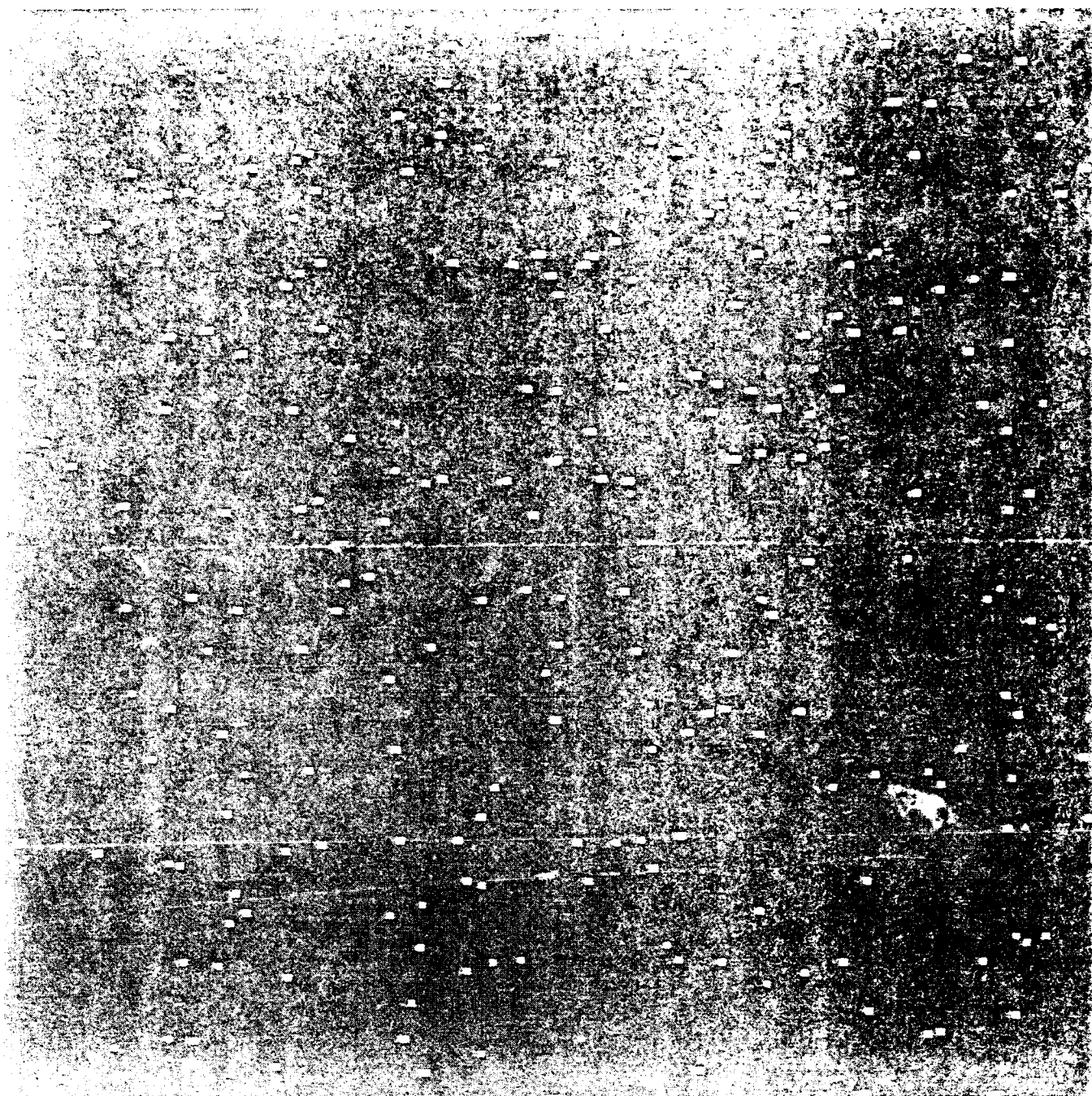
Figure 7.4 — Point Source Image.

APPENDIX TO POINT SOURCE EXTRACTION

Gradient and Step Size Formulae

We use the matrix notation:

D = data vector

P = point response function matrix

S = object estimate vector .

Given an object estimate, S, the estimated data vector is

$$\hat{D} = P S \qquad ; \qquad\qquad\qquad (A\text{-}1)$$

the error vector is

$$E = D - \hat{D} \quad , \qquad\qquad\qquad (A\text{-}2)$$

and the mean square error is

$$mse = |E|^2$$
$$= \sum [e(I)]^2 \qquad\qquad\qquad (A\text{-}3)$$

where $e(I)$ is the Ith element of E.

The kth estimate of S is

$$S^k = S^{k-1} + b\, G \qquad , \qquad\qquad\qquad (A\text{-}4)$$

where G is a gradient vector and b is a scalar. First, we will drive the optimal step size, b.

The $(k\text{-}1)^{th}$ mean square error is

$$mse^{(k-1)} = |E^{k-1}|^2$$

$$= \left| D - \hat{D}^{(k-1)} \right|^2 \qquad , \qquad \text{(A-5)}$$

where

$$\hat{D}^{(k-1)} = P \, S^{(k-1)} \qquad . \qquad \text{(A-6)}$$

The kth mean square error is

$$mse^{(k)} = \left| D^{(k)} \right|^2$$

$$= \left| D - \hat{D}^{(k)} \right|^2$$

$$= \left| D - P \, S^{(k)} \right|^2$$

$$= \left| D - P(S^{(k-1)} + b \, G) \right|^2$$

$$= \left| E^{(k-1)} - b \, P \, G \right|^2$$

$$= \left| E^{(k-1)} \right|^2 - 2 \, b \, (P \, G)^T E^{(k-1)} + b^2 \left| P \, G \right|^2 \qquad . \qquad \text{(A-7)}$$

We want to choose b to minimize this mean square error.

We differentiate (A-7) with respect to b and set the result to zero. This gives

$$b = \frac{(P \, G)^T E^{(k-1)}}{\left| P \, G \right|^2} \qquad , \qquad \text{(A-8)}$$

which is our first result.

To make correspondence between (A-8) and Equation (7) in the main text (Section 7.3), we define the vector

$$Q = P \, G \qquad . \qquad \text{(A-9)}$$

Then (A-8) becomes

$$b = Q^T \frac{E^{(k-1)}}{\left| Q \right|^2}$$

$$= \frac{\sum q(I) e^{(k-1)}(I)}{\sum q(I) q(I)} \qquad . \qquad \text{(A-10)}$$

Equation (A-10) is the discrete form of Equation (7) and Equation (A-9) is the discrete form of Equation (8) in the main text (Section 7.3).

Now we turn to the gradient calculation. The mean square error is, after we drop the k superscript,

$$mse = \left| D - \hat{D} \right|^2$$

$$= \sum \left| d(I) - \hat{d}(I) \right|^2 \quad , \tag{A-11}$$

where, from (A-1),

$$\hat{d}(I) = \sum p(I,J)s(J) \quad . \tag{A-12}$$

In (A-12) $s(J)$ is the Jth element of S and $p(I,J)$ is the I,J element of **P**.

We want to find how to change S to minimize *mse*; that is, we want to find the gradient of *mse* with respect to $s(J)$. Again, we differentiate *mse* in Equation (A-11) with respect to the variable, in this case, $s(J)$.

$$\frac{d\,mse}{d\,s(J)} = -2\sum \left[d(I) - \hat{d}(I) \right] \frac{d\,\hat{d}(I)}{d\,s(J)} \quad . \tag{A-13}$$

But, from (A-12), the derivative in (A-13) is

$$\frac{d\,\hat{d}(I)}{d\,s(J)} = p(I,J) \quad . \tag{A-14}$$

Remembering that our step size *b* can be calculated for <u>any</u> gradient, we cancel the *-2* and define the gradient element

$$g(J) = \frac{1}{-2} \frac{d\,mse}{d\,s(J)}$$

$$= \sum \left[d(I) - \hat{d}(I) \right] p(I,J)$$

$$= \sum E(I)p(I,J) \quad . \tag{A-15}$$

Noting the change of summation indices in (A-12) and (A-15), we see that the vector **G** is

$$\mathbf{G} = \mathbf{P}^T \mathbf{E} \quad . \tag{A-16}$$

54

This result show that the gradient vector is the error image blurred by the transpose of the PRF.

Now we clarify the correspondence between convolution and matrix multiplication. In the case of continuous signals and a convolving PRF, the estimated data is

$$\hat{d}(x) = s(x) * p(x)$$

$$= \int s(\sigma) p(x - \sigma) d\sigma$$

$$= \int s(\sigma) p(x, \sigma) d\sigma \qquad . \qquad \text{(A-17)}$$

This corresponds to the vector case

$$\hat{\mathbf{D}} = \mathbf{P} \mathbf{S} \qquad , \qquad \text{(A-18)}$$

where the elements of $\mathbf{P}$ are $p(x, \sigma)$. The gradient image is, by correspondence,

$$g(x) = \int s(\sigma) p(\sigma, x) d\sigma$$

$$= \int s(\sigma) p(\sigma - x) d\sigma \qquad , \qquad \text{(A-19)}$$

which is a correlation, not a convolution. However, for the case of a symmetric PRF, the case we impose with our regridding procedure,

$$p(x) = p(-x) \qquad . \qquad \text{(A-20)}$$

So (A-19) becomes

$$g(x) = \int s(x) p(x - \sigma) d\sigma$$

$$= s(x) * p(x) \qquad . \qquad \text{(A-21)}$$

This is the result, Equation (6), in the text (Section 7.3).

8. Uncertainty Estimation of Point Source Extraction Results

8.1 Introduction

The point source extraction algorithm extracts the locations and amplitudes of point sources from a regrid, an interpolation image created from sampled data. It produces a list of the amplitudes or fluxes$\{A_k\}$ and locations $\{x_k\}$ for all of the detected point sources in the input image. It is of interest to define and calculate a reliability metric for each parameter of a point source. For the flux estimate, A_k, we calculate a signal to noise ratio, suitably defined (See Section 8.5); and for the location, x_k, we calculate a positional variance. In both cases we require a calculation of the mean of the estimate and its variance.

Any reasonable estimator for A_k or x_k will be unbiased. Thus the actual estimates, A_k and x_k, are their means. The variances will be dependent on noise, sampling profiles, and model uncertainties. In the following section, we describe an analytical method to estimate these variances. (Note that we use one-dimensional notation for the locations but our results are easily generalized to two dimensions.)

8.2 The Cramer-Rao Bound

The Cramer-Rao (CR) bound is a method to bound the variance of any unbiased estimator, a, for an unknown parameter based on data $\{d_m\}$. The bound states that the variance on a must be larger than

$$\sigma_a^2 = \frac{1}{\sum \left(\frac{\partial d_m}{\partial a} \right) / \sigma_m^2},\qquad (1)$$

where σ_m^2 is the noise variance on each data sample and $\frac{\partial d_m}{\partial a}$ is the way each data sample changes with respect to the parameter a. Equation (1) assumes that the noise samples are Gaussian and independent, which is a generally useful assumption. A more involved equation results when these assumptions are not true, and it yields a smaller value for σ_a^2. Thus equation (1) is conservative in the sense that more favorable conditions (i.e., dependent noise, non-Gaussian statistics) could result in a smaller σ_a^2. Equation (1) is the starting point for our estimate of the required variances. In the following sections, we extend it to multiple parameters and show how it can be used in the point source extraction algorithm.

56

8.3 Multiple Parameters

In the usual case we need to estimate a set of parameters. For example we estimate the flux A_k and the position x_k of a star. In this case we must calculate the Fisher information matrix J:

$$J = \begin{bmatrix} \sum_m \left(\dfrac{\partial d_m}{\partial A_k}\right)^2 / \sigma_m^2 & \sum_m \left(\dfrac{\partial d_m}{\partial A_k}\dfrac{\partial d_m}{\partial x_k}\right) / \sigma_m^2 \\ \sum_m \left(\dfrac{\partial d_m}{\partial A_k}\dfrac{\partial d_m}{\partial x_k}\right)^2 / \sigma_m^2 & \sum_m \left(\dfrac{\partial d_m}{\partial x_k}\right)^2 / \sigma_m^2 \end{bmatrix} \quad . \tag{2}$$

With

$$J = \begin{bmatrix} J_{11} & J_{12} \\ J_{21} & J_{22} \end{bmatrix} \quad ,$$

the diagonal elements of J^{-1} are the required variances. Thus,

$$\sigma_A^2 = \frac{J_{22}}{J_{11}J_{22} - J_{12}J_{21}} \quad , \tag{4}$$

and

$$\sigma_x^2 = \frac{J_{11}}{J_{11}J_{22} - J_{12}J_{21}} \quad . \tag{5}$$

This 2-parameter result extends in a simple and obvious way to estimation of many parameters. In the point source extraction algorithm, it is clear that only stars in close proximity to a given star will have non-zero, off-diagonal entries in J. As we shall see, this sorting is already accomplished in the point source extractor so the calculation of J, for a block of closely spaced stars, can easily be accomplished.

8.4 Evaluation of the Partial Derivatives

We need a model for the observed data sample, d_m. The assumption is taken in the point source extractor that d_m is a sample of $d(x)$, the noisy convolution of the true star field and an ideal point response function, $p(x)$.

$$d(x) = p(x) * \sum_k A_k \delta(x - x_k) + n(x) \quad , \tag{6}$$

where $\{A_k\}$ is the set of star fluxes, $\{x_k\}$ is the set of star locations and $n(x)$ is the noise. Equation (6) simplifies to

$$d(x) = \sum_k A_k p(x - x_k) + n(x)$$

and the mth sample at $x = m\Delta x$ is

$$d_m = \sum_k A_k p(m\Delta x - x_k) + n_m \quad .$$

To simplify the notation we assume $\Delta x = 1$ so the d_m sample is

$$d_m = \sum_m A_k p(m - x_k) + n_m \qquad . \qquad (7)$$

Now we can take the partial derivatives:

$$\frac{\partial d_m}{\partial A_k} = p(m - x_k) \qquad (8.1)$$

and

$$\frac{\partial d_m}{\partial x_k} = -A_k p'(m - x_k) , \qquad (8.2)$$

where $p'(x)$ is the derivative of $p(x)$.

To calculate the elements of $\mathbf{J}$, we order the parameters such that the first N parameters are the star fluxes and the next N parameters are the star locations. With this convention J_{11} is a signal-to-noise ratio:

$$J_{11} = \sum \left(\frac{\partial d_m}{\partial A_1} \right)^2 / \sigma_m^2$$

$$= \sum_m p^2(m - x_1) / \sigma_m^2 \qquad . \qquad (9)$$

If σ_m^2 were the same for all m (which it is not, but we assume so only for exposition), we see that J_{11} is a signal-to-noise ratio:

$$J_{11} = \frac{\sum_m p^2(m - x_1)}{\sigma^2} , \qquad (10)$$

where the numerator is the "energy" in the point response function.

This sum will be approximately the same for all shifts. The numerator is the autocorrelation function of $p(x)$, evaluated at the origin. Thus, if

$$R_0(x) = \sum_m p(m)p(m+x) \quad , \tag{11}$$

we see that the numerator is

$$R_0(0) = \sum_m p^2(m) \quad . \tag{12}$$

Now examine J_{12}:

$$J_{12} = \sum_m \left(\frac{\partial d_m}{\partial A_1} \frac{\partial d_m}{\partial A_2} \right) / \sigma_m^2 \quad .$$

From equation (8) and with the constant noise assumption, this becomes

$$J_{12} = \frac{p(m-x_1)p(m-x_2)}{\sigma^2} = \frac{R_0(x_2-x_1)}{\sigma^2} \quad . \tag{14}$$

Thus, we see that the numerator is the autocorrelation function sampled at the spacing of the two stars, exactly as calculated in the point source extractor, at one point.

The observations above take care of one fourth of J, namely the upper left quadrant. We can show that the matrix has symmetries so we need only examine the upper right quadrant and the lower left quadrant.

A typical term in the upper right quadrant is

$$J_{ki} = \sum_m \left(\frac{\partial d_m}{\partial A_k} \right) \left(\frac{\partial d_m}{\partial x_i} \right) / \sigma_m^2 \quad , \tag{15}$$

which involves the cross-sampling between flux A_k and location x_i. From equations (8), (9) and with the same noise assumption, this is

$$J_{ki} = \frac{-\sum_m p(m-x_k)A_1 p'(m-x_i)}{\sigma^2} \quad . \tag{16}$$

The numerator requires evaluation of the cross correlation function $R_1(x)$ between $p(x)$ and $p'(x)$. Thus, with

$$R_1(x) = \sum_m p(m)p'(m+x) \quad , \tag{17}$$

we see that

$$J_{ki} = \frac{R_1(x_k - x_i)A_i}{\sigma^2} \quad . \tag{18}$$

Finally, we must evaluate the terms in the lower right quadrant of J. The typical term is

$$J_{ki} = \sum_m \frac{\dfrac{\partial d_m}{\partial x_k}\dfrac{\partial d_m}{\partial x_i}}{\sigma_m^{\,2}} \quad , \tag{19}$$

which becomes

$$J_{ki} = \frac{A_k A_i}{\sigma^2} \sum_m p'(m - x_k)p'(m - x_i) \quad . \tag{20}$$

With $R_2(x)$ the autocorrelation function of $p'(x)$, we have

$$J_{ki} = \frac{R_2(x_k - x_i)A_k A_i}{\sigma^2} \quad . \tag{21}$$

Combining these results, we have for J:

$$J = \frac{1}{\sigma^2}\begin{bmatrix} \begin{bmatrix} R_0(x_k - x_i) \end{bmatrix}_{k,i=1,\ldots,n} & \begin{bmatrix} -A_i R_1(x_k - x_i) \end{bmatrix}_{k,i=1,\ldots,n} \\ \begin{bmatrix} -A_k R_1(x_i - x_k) \end{bmatrix}_{k,i=1,\ldots,n} & \begin{bmatrix} A_i A_k R_2(x_k - x_i) \end{bmatrix}_{k,i=1,\ldots,n} \end{bmatrix} \quad . \tag{22}$$

J is a $2N$ by $2N$ matrix. The first N diagonal elements of the inverse of J are the variances on the N fluxes. The second N diagonal elements are the variances on the N locations.

8.5 Signal-to-Noise Calculations and Processing Gain

Signal-to-Noise (SNR) is an important measure of the reliability of point source parameter estimates, such as position and flux. The SNR definition for a single parameter, such as the flux, A, of a point source, is as follows. We define

A = unknown parameter

$\hat{A}$ = estimate of A

E = A - $\hat{A}$ = error

b = bias in E

= av(E)

and

E_{rms} = root mean square value of E

= $(\mathrm{av}(E^2))^{1/2}$.

The *SNR* for the estimate $\hat{A}$ is

$$SNR = \frac{\mathrm{av}(\hat{A})}{E_{rms}} ,$$

and for an unbiased estimate , for which

$$\mathrm{av}(\hat{A}) = A \quad ,$$

the *SNR* is

$$SNR = \frac{A}{E_{rms}} .$$

As a first example of the use of this definition, we consider a set of data samples

$$d(m) = Ap(m) + n(m) \quad , \tag{23}$$

where $p(m)$ is the mth sample of a point response function and $n(m)$ is the mth sample of noise. A matched filter estimator for A will be

61

$$\hat{A} = \frac{\sum p(m)d(m)}{\sum p(m)p(m)} \quad , \tag{24}$$

for which, with unbiased noise samples,

$$\hat{A} = A + E \quad , \tag{25}$$

where E is an unbiased scalar. Thus $\hat{A}$ is unbiased and its *SNR* is

$$SNR = \frac{A}{E_{rms}} \quad , \tag{26}$$

as determined earlier.
To evaluate E_{rms} we combine Equations (23), (24), and (25) to get

$$E = \frac{\sum p(m)n(m)}{\sum p(m)p(m)} \quad . \tag{27}$$

Thus, $av(E^2)$ is

$$av(E^2) = \left(\frac{1}{\sum p(m)p(m)} \right)^2 \sum \sum p(m)p(l)\, av(n(m)n(l)). \tag{28}$$

If the $n(m)$ samples are independent, zero mean random variables with variance σ_m^2, then the $av(E^2)$ in Equation (28) is zero unless $m = l$, and Equation (28) reduces to

$$av(E^2) = \left(\frac{1}{\sum p^2(m)} \right)^2 \sum p^2(m)\sigma_m^2 \quad . \tag{29}$$

If, in addition, all noise variances are equal (in the summation over m) to σ^2, then Equation (29) becomes

$$av(E^2) = \frac{\sigma^2}{\sum p^2(m)} \quad , \tag{30}$$

and *SNR* is

$$SNR = \frac{A\left(\sum p^2(m) \right)^{1/2}}{\sigma} \quad . \tag{31}$$

This calculation is easily made. The *SNR* for any estimated flux is the product of the flux, itself, and the *rms* value of the point response function divided by the standard deviation of the noise on the input data.

For simplicity, the preceding derivation assumes uniform sample density in both dimensions. In our application, there are typically four times fewer samples available in the cross scan dimension than inscan. Therefore, the actual computed *SNR* values reflect the local cross scan sample density, and are usually approximately half of what the preceding equations indicate.

It is of interest to calculate the processing gain associated with the estimator $\hat{A}$ for A. Thus, if one used a typical, single sample of the data to estimate A, say $d(0)$, the central data sample, the estimate would be, from Equation (23) and by assuming no noise,

$$\hat{A} = \frac{d(0)}{p(0)} \quad . \qquad (32)$$

This estimate is also unbiased since, from Equation (23),

$$\hat{A} = A + \frac{n(0)}{p(0)} \quad . \qquad (33)$$

The *rms* error is, simply,

$$E_{rms} = \frac{\sigma}{p(0)} \quad . \qquad (34)$$

and the *SNR* is

$$SNR = \frac{A\, p(0)}{\sigma} \quad . \qquad (35)$$

Redefining this as the input *SNR*

$$(SNR)_{in} = \frac{A\, p(0)}{\sigma} \qquad (36)$$

and the earlier calculation as the output *SNR*,

$$(SNR)_{out} = \frac{A\left(\sum p^2(m)\right)^{1/2}}{\sigma} \quad , \qquad (37)$$

we can calculate the processing gain,

$$G = \frac{(SNR)_{out}}{(SNR)_{in}} \quad , \qquad (38)$$

and G is

$$G = \frac{\left(\sum p^2(m)\right)^{1/2}}{p(0)} \quad . \tag{39}$$

For the ideal point response function in our application, $G \approx 3.4$.

For our second application we consider two point sources which are separated in the inscan direction by a distance x. A third applicatic͏ ͏ ͏ ͏int sources separated in the cross scan direction by a distance y. Figure 8.5.A depicts these cases of one interfering star.

In both applications we draw on the Cramer-Rao Bound calculations presented earlier, in which the joint estimation of parameters of one, two, or many point sources was considered. In the case of one point source, the variance on $\hat{A}$ was shown to be Equation (30), when the noise is as described previously. In the case of two point sources, the variance is

$$E_{rms} = \frac{\sigma^2}{\sum p^2(m)} \frac{1}{1-F^2} \quad , \tag{40}$$

where F is a factor

$$F = \frac{\sum p_1(m)p_2(m)}{\sum p_1^2(m)} \quad , \tag{41}$$

and $p_1(m)$ and $p_2(m)$ are both the PRF of the ideal detector, shifted by the separation of the point sources.

When we make the calculations indicated by Equation (41), put them into Equation (26) and then into Equation (28) for the processing gain, the two curves shown in Figure 8.5.B are obtained. Thus, for example, when two stars are separated in the cross scan direction by 10 pixels, the processing gain is approximately 1.4, whereas with a large separation, the gain is 3.4. These curves show that interacting point sources suffer a loss in processing gain whenever their separation is less than 5 pixels inscan or 20 pixels cross scan. The curves in Figure 8.5.B illustrate the quantitative measure of that loss.

8.6 Discussion

Note that **J** as defined in Section 8.4, Equation (22) has elements which contain the estimated amplitudes and positions. This means that the variances will be highly object-
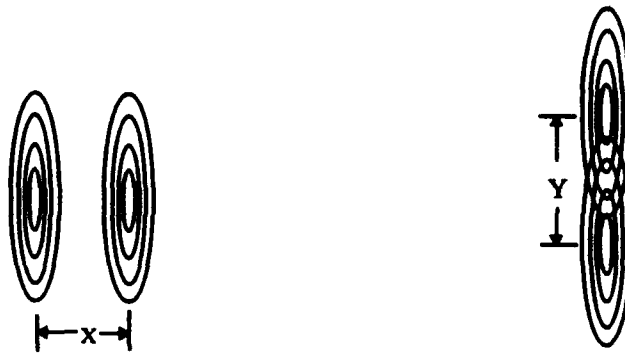
Figure 8.5.A One interfering point source with (a) inscan separation, and (b) cross scan separation.
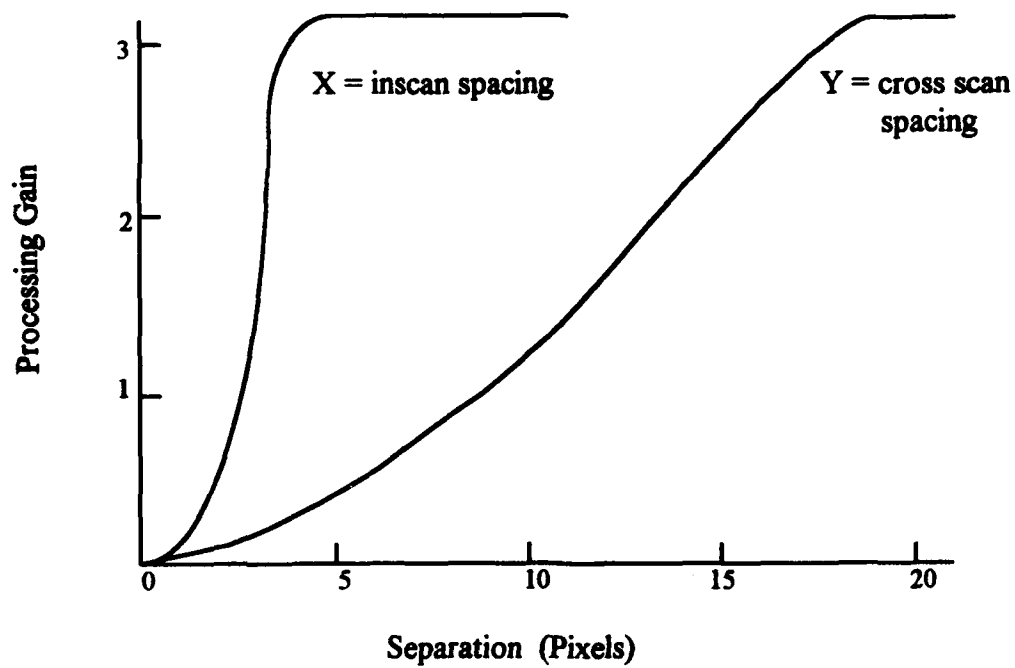
Figure 8.5.B Processing Gain vs. Point Source Separation

65

dependent. For example, if A_k is small, we observe that the variance on x_k will be large, as seems intuitively satisfying. Also the procedure incorporates the uncertainties in estimation of A_k based on the estimated values of A_k and its closest neighbors. We observe that for a faint source in close proximity to a bright source, the flux variance is larger than if the faint source were isolated.

8.7 Algorithm Implementation

This estimator uses the per-scan noise values are passed from the data conditioning algorithm, and the point source locations and amplitudes given by the point source extractor as inputs to the CR-bound calculation given in Sections 8.3-8.4. For each point source uncertainty estimate, the *nearest* data scan noise value was identified and used.

8.8 Results

For the majority of the point sources in the database, uncertainties have been calculated for flux and position with the Cramer-Rao Bound technique. Typical values for σ_{inscan} are .1-2.0 pixels, and for $\sigma_{cross\,scan}$ are .3-7.0 pixels. It is true in general that there is an inverse relationship between *isolated* point source amplitudes and their positional uncertainties as estimated by CR-Bound. We observe that the *actual* CR-Bound positional σ's are substantially different than the equivalent PSC positional uncertainties for verified fields. Figure 8.8.A depicts CR-Bound $\sigma_{cross\,scan}$ vs. PSC SMJ for matched sources.

CRBD Ypos Errors vs. PSC SMJ position uncertainties
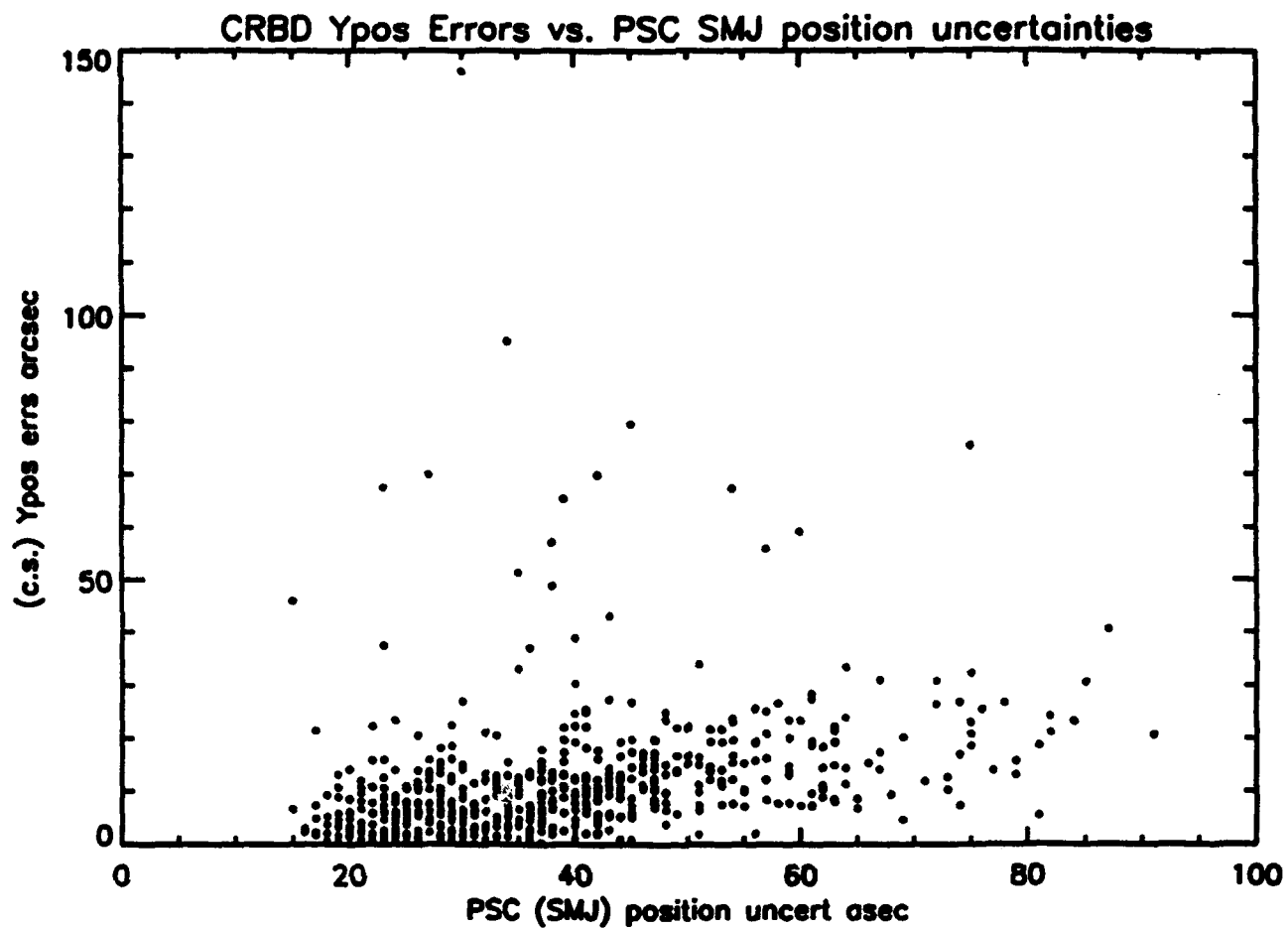
Figure 8.8.A   CR-Bound Cross Scan Positional Uncertainty vs. PSC (SMJ)
Positional Uncertainty

9.0 HCON MERGE LOGIC

During pass 1 processing, this algorithm for merging point source lists from different HCONs was developed and tested. It has not been applied to the delivered pass 1 point source list database.

In each band, most plate regions have three point source lists which must be merged into a single catalog entry. The three HCON coded lists are concatenated and ordered according to decreasing SNR. Beginning with the highest SNR source as a seed, we search the list with a coarse spatial window (0.75' x 1.5') to collect all the potential mergers in the neighborhood. Mergers must be from a different HCON than the seed. Each merger must pass a test of probability that it represents the same source as the seed. This is done based on the amount of overlap of the unique error spaces of the seed and the merger being tested. If there are still multiple mergers within an HCON after the position test, they are resolved to one merger per HCON by choosing the one with the highest SNR. Most of the time, there is only one merger from each non-seed HCON. A flux ratio test is applied to merges between sources from HCON1 and HCON2. These sources must have a flux density ratio within a factor of two. If an HCON1:HCON2 pair fails the flux test, the one with the higher SNR is kept and the other is not used. No flux matching requirements are put on any merges including an HCON3 source. That is because the HCON3 scans were acquired months later than the HCON1 and HCON2 scans, and we don't want to exclude sources which exhibit variable flux densities. Now, with a seed from one HCON, and a merger each from the other two HCONs, the positions, fluxes and uncertainties are combined into a single source record. The positions and their uncertainties are flux weighted averages of the seed and merger. The reported flux is $(f_1 f_2 ... f_n)^{1/n}$, where n is the number of sources involved in the merge. The SNRs are combined in the following manner:

$$SNR = \frac{n}{\sqrt{\sum_{i=1}^{n} \frac{1}{(SNR)_i^2}}} \qquad (19)$$

For equal SNRs, this is equivalent to $\sqrt{n}$ SNR.

When a source has been a seed or involved in a merge, it is removed from the list. HCON merging eliminates spurious sources due to noise, radiation hits and moving objects. Figure 9.1 is a flowchart for the HCON merge algorithm.

Figure 9.1   HCON MERGE LOGIC
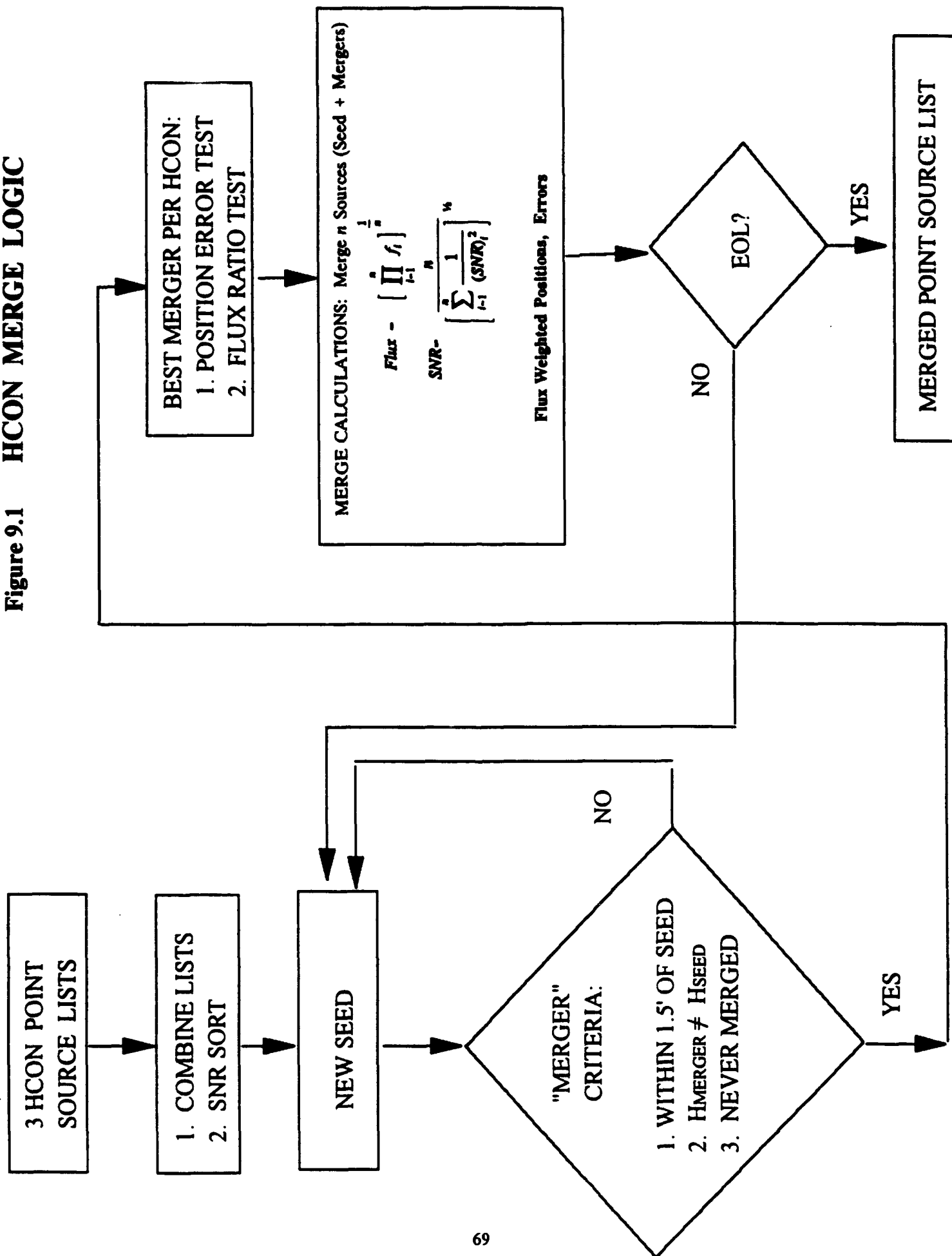
10.0 VALIDATION

Throughout algorithm development and pass 1 processing we used comparisons with the PSC to build validity for our growing point source database. This section offers a brief review of the quality of data our algorithms were producing at the end of the project. Two other sources of validation for the results of the survey image processing are available from the ground based observations and the GPS AO Point Source Catalog, both produced by the University of Wyoming during this project. These topics are discussed in section 14.0.

In Table 10.0 we have compared selected GPS results with the PSC FQUAL=3 data. Most columns in this table are self-explanatory, with the exception of the last four which will be discussed shortly. Of primary interest are columns four and five, listing the increase in source count provided by the GPS and the "success rate" of the GPS in recovering the original PSC sources. The SNR threshold employed here in the "HCON merge" step of the GPS extraction and validation process was 4.4 : 1. This is slightly conservative, largely accounting for the ~1-2% of PSC sources which are not shown as confirmed here. For those PSC sources in the fields covered by this table, the average Band 1 flux ratio of GPS:PSC data is 1.005 : 1. Although this may be serendipitously close to 1.0, these fields were *not* specially selected to show excellent flux agreement with the PSC. The σ for the GPS:PSC Band 1 flux ratio here is 4.7%, achieved without application of heuristic flux correction factors.

The last four columns of Table 1 characterize the consistency of GPS and PSC position assignments for the PSC sources in these fields. As is clear, σ_{RA} is the only potential indicator of position "discrepancies" here, being about 25 arcsec. The meaning of σ_{RA} rather closely corresponds to the semi-major axis (SMJ) of the PSC position uncertainty ellipse; both metrics are dominated by the influence of the large cross scan extent of the IRAS detectors. For all PSC sources with Band 1 fluxes less than 1 Jy (which dominate the GPS), the PSC's average SMJ is approximately 45 arcsec. (Because the statistics of PSC position uncertainties are not purely Gaussian, the SMJ parameter is not easily characterized as 2σ or 3σ.). Thus, this ~25 arcsec σ_{RA} is highly consistent with PSC position uncertainties.

Table 10.0 Galactic Plane Supplement vs Point Source Catalog

Field Center	Field Area	N_{GPS}	$\dfrac{N_{GPS}}{N_{PSC}}$	% PSC Confirmed	Mean δ_{RA}	σ_{RA}	Mean δ_{DEC}	σ_{DEC}
(l, b)	(deg^2)	(deg^{-2})			(arcmin)	(arcmin)	(arcmin)	(arcmin)
-24.9, +0.5	8.7	116	3.3	97.9	+0.04	0.48	-0.02	0.09
-11.4, -0.2	10.8	145	3.5	97.7	+0.04	0.44	-0.02	0.06
+ 9.1, -0.7	10.9	171	3.2	99.2	+0.02	0.38	-0.01	0.05
+25.4, +0.3	8.9	200	3.7	97.6	-0.02	0.39	0.00	0.06
- 4.6, +2.2	11.5	102	2.5	99.6	0.00	0.38	-0.01	0.05
+34.9, -0.4	7.2	251	4.8	97.4	+0.03	0.42	+0.02	0.09

Figure 10.0 shows a cumulative log(N) - log(S) comparison of GPS data with corresponding PSC data. It is noteworthy that the additional sources extracted by GPS processing are not restricted only to sub-Jy flux density levels. There is a significant number of additional sources found here in the 1 - 10 Jy range by the GPS processing. Although the GPS "*first pass*" processing did not find this high-flux source density increase for all fields, neither was it uncommon. It was true for all fields, however, that the GPS was complete to lower flux levels than the PSC.

Figure 10.0.1 is a 12μm high resolution image of the galactic plane at RA=263.5°, Dec= -32.4°. It was made from IRAS Survey footprint data in the manner described in sections 5 and 6. It is the sum of a background image and a point source image from the GPS Image Atlas. Figure 10.0.2 shows the point sources extracted from figure 10.0.1. This image was made by adding a background image and an image of extracted point sources like the one in figure 7.4.C.

GPS

Sources per Deg^2

$RA_0 = 283.5°$
$DC_0 = 1.5°$

Area = 7.0 deg^2
2089 Sources
Slope Fit = -1.30 +/$-$ 0.02

$l_0 = 34.9°$ $b_0 = -0.4°$

Flux Density (Jy)

PSC

Sources per Deg^2

$RA_0 = 283.5°$
$DC_0 = 1.5°$

Area = 7.2 deg^2
374 Sources
Slope Fit = -1.11 +/$-$ 0.01

$l_0 = 34.9°$ $b_0 = -0.4°$

Flux Density (Jy)
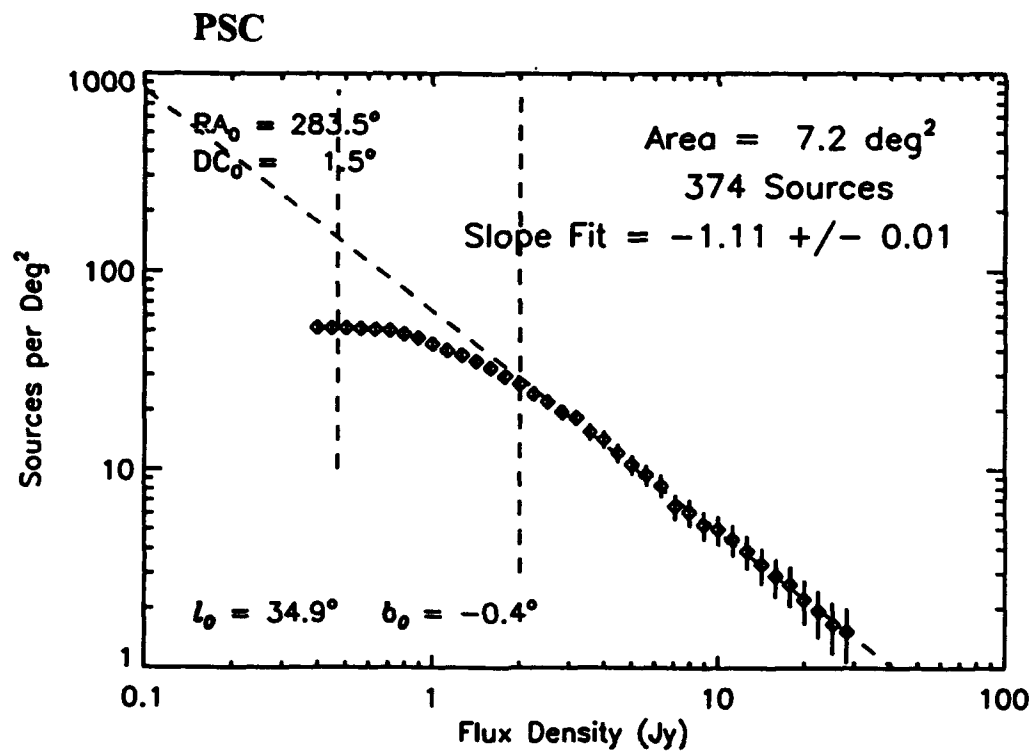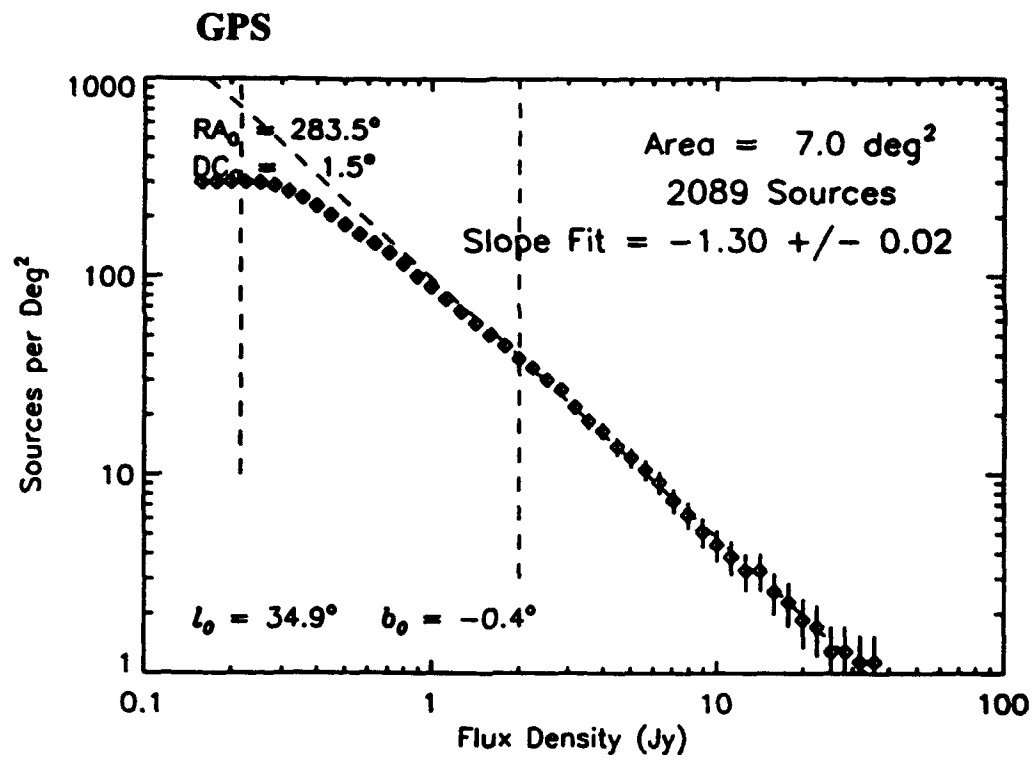
Figure 10.0   Cumulative Source Counts for GPS and PSC
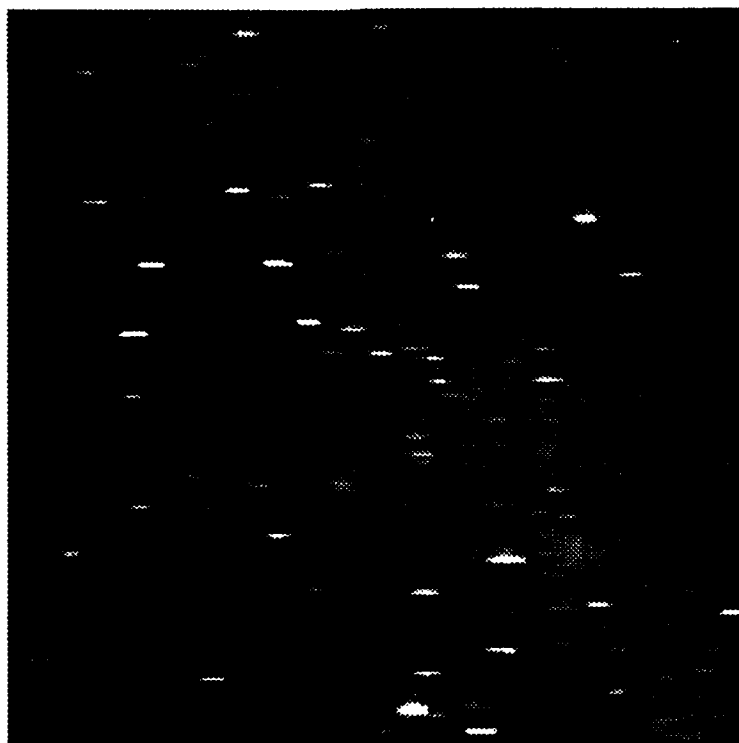
Figure 10.0.1   High Resolution Galactic Plane Image
made from IRAS Survey Footprint Data.
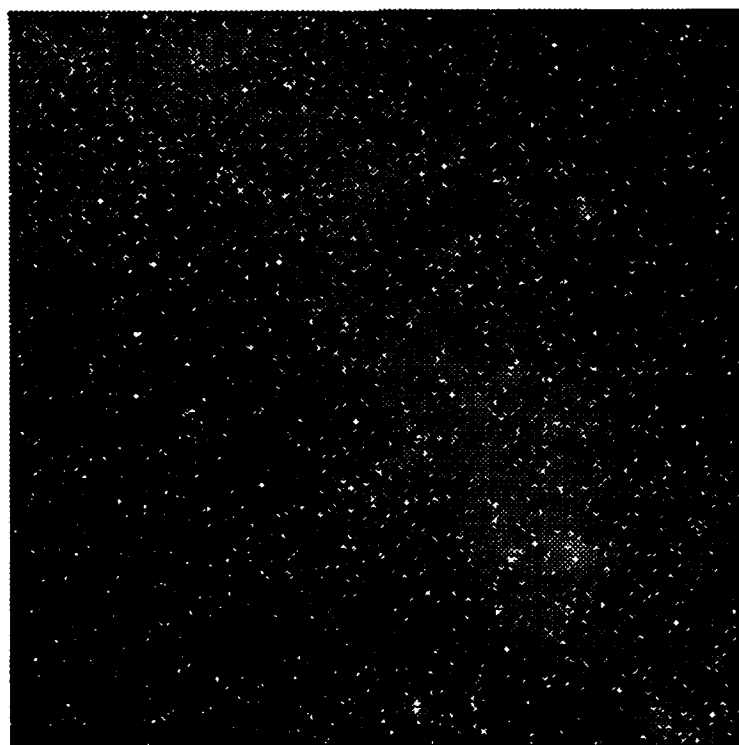
Figure 10.0.2   Image Representation of Point Sources Extracted
from Galactic Plane Image in figure 10.0.1.

11.0 CAVEATS

11.1 HCON Scan Sort

Sorting the scans by SOP group and scan angle into three HCON groups prior to image construction meant that for any given HCON image, the scan density in the cross scan dimension was always approximately one third of the scans available. In some plates it was not possible to use all the scans when forming three HCONs. Usually 75% to 99% of the available scans were included by the time the three HCON groups were defined. In some plates, two or more distinct SOP groups were combined as a single HCON so there would be enough scans to construct an image. When this happened, the combined SOP groups were as close in time as possible, and scans with SOP numbers greater than 425 were not mixed with scans whose SOP numbers were less than 426. All HCON 3 images are made from scans with SOP numbers greater than 425. SOP group mixing is responsible for some of the patches of low contrast striping visible in some of the images.

11.2 Band Pass Values in Flux Units Conversion

The band pass values used to convert instrumental flux to flux density in the early data conditioning stage of the processing were $1.5939e13$ and $5.6320e12$ Hz for 12 and $25\mu m$, respectively. They should have been $1.348e13$ and $5.16e12$ Hz respectively, according to the Explanatory Supplement for IRAS Catalogs and Atlases (pg. X-13). This was confirmed by personal communication with T. Chester at IPAC. The bandpass values which were used for the delivered, first-pass processed data base lead to an underestimation of flux densities (for point source lists, images and noise estimates) of approximately 15% ($12\mu m$) and 8% ($25\mu m$).

11.3 Noise Estimation

Due to the use of incorrect bandpass values in the flux density units conversion as described in section 11.2, the noise estimates described in section 5.6 are 15% ($12\mu m$) and 8% ($25\mu m$) lower than they ought to be. In addition, the high pass filter (section 5.6) used to estimate the noise is not identical to the filter which is derived from the described Wiener filter solution. The correct filter function values are [0.015, -0.087, -0.040, 0.115, 0.070, -0.085, -0.488, 1.0, -0.488, -0.085, 0.070, 0.115, -0.040, -0.087, 0.015]. Tests comparing use of the two filters show that the filter defined in section 5.6 consistently gives a one sigma noise estimate that is 10% lower than the noise estimates which result from using the properly derived filter function defined here.

11.4 Background Removal

The use of lower bound operators in separating the diffuse and point source signal components leads to representations of the scans which put point sources and noise on equal footing above zero. A better separation would place the zero line through the noise signature, resulting in some portion of the noise being negative. The algorithm improvement prepared for pass 2 processing provides such improved placement of the zero point base curve. However, the delivered, "pass 1" processed data base used lower bound operators which left the majority of the noise signature positive. The pass 1 products (point source lists *and* images) have a small positive bias (higher for noisy detectors), and difficulty in discriminating between faint sources and noise peaks. The bias is ~ 0.15 Jy for point sources and it causes the noisy stripes visible in the point source images. Refer to section 5.7 for a full description.

11.5 Image Bright Stripe Artifact

A small percentage of the images have a processing artifact which looks like a ramped bright stripe in the in-scan direction. It originates in the first stage of the background removal algorithm, and occurs when the first sample in a scan is part of a bright point source signature (i.e., a point source is on the edge of a plate boundary). A spatially coincident dark ramp stripe will appear in the associated background image. Point sources extracted from the ramped region are unreliable.

11.6 Detector Bias Removal From Background Images

Separation of the point sources from diffuse background emission leaves minor detector variations in the background signal. These were treated as biases, estimated and removed during background image construction. Differential detector bias estimation and removal were accomplished as follows. Background scans were sorted into their correct cross scan order. For each scan, the average of all samples was computed. The averages of the ordered scans represent a cross scan view of the scan set. That cross scan profile is bumpy with minor detector specific variations. The bumpy cross scan profile was smoothed with a boxcar averager of width 15 to make a curve which represents large scale background variations over the field. The difference between the original cross scan profile and the smoothed one is our estimate of the detector bias variations. There is one bias value for each scan in the difference profile. For each scan, that bias value is subtracted from all the samples in the scan. Except for the subtraction of these small biases, the sum of a background image and its associated point source image is equivalent to the image one would produce in the absence of the background separation algorithm.

11.7 Parallel Scan Angle Assumption

Assuming the scans within an HCON group are parallel for the purposes of image construction has the potential to contribute to position and flux uncertainties in the point source lists. (All the scans in an HCON plate are rotated by the same angle (the average of the group) toward 0°.) The potential for error is highest at the edges of plates, and highest for the 2% of the data sets whose angle spread exceeds 2.3°. Refer to section 5.5 for more description, and discussion of tests of the assumption.

11.8 Noisy Detector Stripes in Images

If, when viewing the point source images, you scale them so you can see faint sources, you will also see prominent periodic stripes at the level of the noise. These are the locations of the noisy detectors. They are emphasized by the fact that the lower bound operators used in pass 1 background removal leave almost all the noise above the zero line. For noisy detectors, that amounts to a slightly higher bias than for the other detectors. The improvement prepared for pass 2 processing eliminates these stripes. See section 5.7 for a more thorough description.

11.9 Point Response Functions and Background Removal

While the point source signatures in the data have undergone the background removal operation, the point response profiles used in image construction have not. A test of the effect of this discrepancy indicates that it could lead to a point source flux underestimation of ~ 5%. Pass 2 preparations included performing background removal of the point response functions. No full field tests on survey data were performed to make a comparison.

11.10 Flux Underestimation in Point Source Extraction

In the point source extraction algorithm, the first estimate of point source locations is quantized to a 14.4 arc second image pixel. The fluxes associated with them are computed at the quantized location. A parabolic fit refinement is then made for the reported point source locations so they are no longer quantized to any image pixel size. In the pass 1 data, the associated flux refinement was not made. We have estimated this omission to lead to a small flux underestimation on the order of a few percent. Pass 2 preparations include the refined flux solution.

11.11 Faint Sources With Close, Bright Neighbors

Simulation tests of the point source extractor were used to explore the effects on faint sources of close, bright neighbors. In particular, we observed significant errors in the recovery of the cross scan positions of faint sources with close, bright neighbors. A "faint" source was of equivalent brightness as $5*1\sigma$ noise (~ 0.45 Jy). "Bright" sources were 5 - 80 times brighter. The prf was an average band 1 detector response profile. When the in-scan separation between the faint-bright pair was less than 30 arc seconds (~ half a prf width) AND the cross scan separation was less than 200 arc seconds, the faint source's position (in-scan and cross scan) was recovered with 10-50 % errors when the bright source is 5-20 times brighter than the faint one. Smaller source separations in both dimensions and higher flux ratios lead to failure to recover the faint source. The faint source may still be recovered well when the cross scan separation is small, if the in-scan separation is greater than ~ 60 arc seconds. The recovered flux of the faint sources decreases proportionally with the increase in the position error. This happens because bright sources "ring" on the first iteration of the deconvolution in point source extraction. During subsequent iterations, the nearby faint source first appears on the ring around the bright source, where the energy in the neighborhood is currently concentrated. At that point the faint source is pushed away from its true position by the bright source. The effect is by far the greatest in the cross scan dimension which is the long prf dimension. In simulations of IRAS survey images, a couple hundred deconvolution iterations can move the faint source back to its original position and recover the proper flux. In real data, the number of practical iterations is limited to 10-15 (pass 1 used 10) because of noise and imperfect knowledge of the prf. Therefore, a faint source with a close, bright neighbor may sometimes be reported with a lower flux and a less reliable cross scan position than if the source were isolated. No attempt has been made to determine which faint sources might suffer this particular type of flux and cross scan position uncertainty.

11.12 Spurious Sources Due to Detector Memory at bright Sources

For *very* bright sources, detector memory effects cause a significant false flux signature on the trailing side of the source. The point source extractor may find sources in those tails. Since two HCON images have the tail in the same direction, there is potential for those spurious sources to pass an HCON merge which requires two source confirmation. An examination of the three HCON images of the region in question will reveal whether memory related spurious sources have passed the merge. In the HCON 3 image, the tail (and potential spurious sources) will be on the side of the bright source which is opposite their location in the HCON 1 & 2 images.

11.13 Flux Correction Terms

The only flux correction terms applied to the pass 1 data base were the DC/survey rate response ratios recorded on pg. IV-9 of the IRAS Explanatory Supplement. During the point source conversion from x, y, flux to RA, Dec, Flux, the 12μm point source flux densities were divided by 0.78, and the 25μm flux densities were divided by 0.82.

11.14 Coverage Holes

While the scan snip plates provided by IPAC were 6° on a side (on 5° centers), we processed the 6° plates as four quadrant plates, 3.5° on a side. In some plates, the scan angle was large enough that when the scans were rotated in the 3.5° frame, enough data was rotated off the edge of the frame to cause a hole in the coverage. We estimate the loss in coverage caused in this manner at less than 1% of all the galactic plane survey data shown on the map in figure 4.1. Table 11.14 identifies regions affected by the coverage holes.

Table 11.14 Coverage Holes Due to Scan Rotation

Plate #	Middle	Side	Top
0880	√		
0881	√		
0951	√		
0952	√		
0953	√		
1023	√		
1024	√		
1025	√		
1026	√		
1096	√		
1097	√		
1098	√		
1166	√		
1167	√		
1168	√		
1233	√		
1234	√		
1235	√		
1297	√		
1298	√		
1299	√		
1358	√		
1359	√		
1360	√	√	
1361	√		
1415	√		
1416	√		
1417	√		
1418	√		
1469	√		
1470	√	√	√
1471	√	√	√
1519	√		
1520	√	√	
1521	√	√	√
1564	√		
1565	√	√	
1566	√	√	
1604	√		
0808	√		
0736	√		
0392	√		
0391	√		
0390	√		
0333	√		
0332	√		
0278	√		

```
            TOP
             X
   +-----------------+
   |                 |
MIDDLE            SIDE
   X                X
   |                 |
   +-----------------+
```

Plate #	Middle	Side	Top
0275	√		
0227	√		
0226	√		
0225	√		
0224	√		
0223	√		
0179	√		
0178	√		
0177	√	√	
0176	√	√	
0175	√	√	
0174	√		
0170	√	√	
0169	√	√	
0168	√	√	
0167	√	√	
0166	√		
0136	√	√	
0135	√	√	
0134	√		
0132	√	√	
0131	√	√	
0130	√	√	
0129	√	√	
0128	√	√	
0127	√	√	
0126	√		
0098	√	√	
0097	√	√	
0096	√	√	
0095	√	√	
0094	√	√	
0093	√		
0214	√	√	
0213	√	√	
0212	√	√	
0211	√		
0261	√	√	
0260	√	√	
0259	√		
0313	√	√	
0312	√		
0453	√		
0452	√		
0517	√		

12.0 PRODUCTS

12.1 Galactic Plane Supplement Image Atlas

A set of "high resolution" IRAS survey galactic plane images is being delivered to Phillips Lab as results of this project. Each image is a 12.25 square degree frame (3.5° on a side), and is a quadrant of an IPAC archival plate. (Refer to Table 4.1 and Figure 5.1.) There are twelve images for each quadrant. Six are from 12μm data and six are from 25μm data. Of the six 12μm images, three (HCON 1,2,3) are images of the point source content of the survey signals, and three are background images of the diffuse, extended emission. They are high resolution in the sense that they are interpolated from IRAS survey footprint data onto an image grid space whose pixels reflect the finest sample spacing available (14.4 arc seconds).

An example of an image filename is 0880b_21.pic. The first four numbers (0880) are the IPAC plate number (Table 4.1). The letter in the fifth place is the MRC quadrant (a, b, c or d) in the larger plate (see Figure 5.1). The "2" in the seventh place is the HCON number (1, 2 or 3). The number in the eighth place (1 or 2) represents the IRAS band number; 1 for 12μm, and 2 for 25μm. Background images have a final ".bkgd" extension. Associated point source and background images may be summed for a complete high resolution IRAS view of the galactic plane.

The pass 1 processed images are delivered in binary form with separate header files and are accompanied by a FITS writer which will combine a header and a binary image. If one chooses to study the images in their non-FITS format, the following information will be helpful. The format of the ASCII header files is apparent from viewing one in an editor; the meaning and exact format of each line is spelled out at the end of the file. The binary images are 876 x 876 REAL*4 arrays. To view them in "near equatorial coordinates", they must be displayed with an upper left origin and rotated 90° CW. (If displayed in IDL with a lower left origin, two applications of the "rotate" command with values of 7 then 3 will accomplish the re-orientation.) "Near Equatorial Coordinates" means that when the frame's scan angle is 0° the vertical axis will be Dec (increasing up) and the horizontal axis will be RA (increasing to the left). All images with a non-zero scan angle will be rotated north into east, Dec into RA by the frame's scan angle. Scan angles are recorded in the header files. The pixel coordinate associated with the image's physical reference center is given in the header file for the starting image orientation (lower left origin), and assumes the pixels are numbered from 1 to 876. If the reference pixel is to be used with the image in near equatorial coordinates, it must be traced through the re-orientation:

$$(\text{new in-scan refpix}) = 876 - (\text{orig in-scan refpix}), \quad \text{and}$$

$$(\text{new c.s. refpix}) = 876 - (\text{orig c.s. refpix}).$$

In the starting image orientation, the in-scan direction is parallel to the horizontal axis. In the near equatorial orientation, the in-scan orientation is parallel to the vertical axis.

12.2 Galactic Plane Supplement Point Source Database

In its pass 1 processed form, the GPS is a point source list database. For each quadrant plate, the database contains six point source lists: three separate HCON lists in each of the 12 and 25μm bands. Uncertainty estimations, point source SNR definitions, and HCON merging were developed during pass 1 processing so uncertainties and SNR tags are not present in the early lists. Every list contains the point sources extracted from a single HCON plate. At least three columns are present: position in RA (degrees) and Dec (degrees) (1950), and flux in Janskys. The lists are ASCII and can be examined in an editor. No HCON merging, plate overlap merging or band merging has been performed on the delivered pass 1 GPS Point Source database.

Table 12.2.1 lists the plates in order of their pass 1 processing dates. All lists prior to plate number 0098 have 3 column point source lists containing position and flux. Lists between plate numbers 1234 and 0313, inclusive, have five columns: RA, Dec, Flux, SNR and Correlation. SNR values should be divided by the processing gain value of 6.7. (Refer to section 8.6.) No SNR thresholds have been applied to these lists. The correlation value is a 2-D extension to the method used to compute PSC correlation values. In these lists it is a correlation between a source's signature in the image data and the source's signature in the ideal data set derived during point source extraction. Lists from plates 1564 through 1566 have seven columns. In addition to the five columns described so far, these lists contain the in-scan (column 6) and cross scan (column 7) position uncertainties computed with the Cramer Rao Bound algorithm described in section 8. The units of the position uncertainties are pixels (14.4 arc seconds per pixel). These uncertainties should be regarded as theoretical bounds on the *minimum* values of the variances they describe. Plates 1604 and 0094 have eight column point source lists. The eighth column is an integer identifying which HCON image the list is from. Plates 0096 through 0840 have eight column point source lists like those described thus far, but with an additional line in each point source list file. The first line contains a single number which is the scan angle for the sources in the list. The angle is given in degrees of rotation, north into east, Dec into RA. The naming convention for the point source list data base is identical to that described in section 12.1 for images.

Table 12.2.1 Survey Plates in Order of Re-Processing

PLATE

0279	0395	1416	0259
0278	0452	1417	0134
0393	0453	0136	1026
0520	0454	0177	1233
0177	0455	0178	1361
0178	0456	0179	1418
0454	0457	0331	0736
0455	0519	0277	0807
0452	0522	0275	0808
0453	0523	1469	0878
0456	0587	0225	0879
0457	0663	1470	0695
0332	0733	1471	0696
0333	0521	1519	0767
0335	0734	1520	0768
0334	0735	0313	0769
0390	0806	1564	0839
0391	0226	1521	0840
0392	0227	1565	
0394	0276	1566	
0395	0517	1604	
0519	0881	0094	
0521	0224	0096	
0522	0953	0097	
0523	0880	0129	
0587	1023	0128	
0588	1024	0127	
0520	1025	0126	
0518	1096	0166	
0589	1097	0130	
0590	0951	0167	
0591	0952	0168	
0592	1098	0132	
0659	1166	0135	
0660	1167	0169	
0661	1168	0131	
0662	0093	0170	
0278	0095	0174	
0279	0098	0175	
0332	1234	0176	
0333	1235	0211	
0334	1297	0212	
0335	1298	0213	
0390	1299	0214	
0391	1358	0223	
0392	1359	0260	
0393	1360	0261	
0394	1415	0312	

References

Explanatory Supplement to IRAS Catalogs and Atlases, 1988, Pasadena, California Institute of Technology.

Frieden, B.R., "Fisher Information and Uncertainty Complementarity," Phys. Lett. A, Vol. 169, No. 3, 123-130 (1992).

Gonsalves, R.A., R.M. Korte, J.P. Kennealy, "Entropy-based Image Restoration: Modifications and Additional Results," Proc. SPIE, Vol. 829 (1987).

Gonsalves, R.A., J.P. Kennealy, R.M. Korte and S.D. Price, "FIER: A Filtered Entropy Approach to Maximum Entropy Image Restoration," Maximum Entropy and Bayesian Methods, ed. P.F. Fougere, Kluweter Academic Press (Neth), 369 (1990).

Gorman, J.D., and A.O. Hero, "On the Application of Cramer-Rao Type Lower Bounds for Constrained Estimation," Proc. International Conference on Acoustics, Speech, and Signal Processing, Vol. 2, 1333-1336 (1991).

IRAS Faint Source Survey Explanatory Supplement Version 2, 1992, Pasadena, California Institute of Technology.

Kennealy, J.P., R.M. Korte, R.A. Gonsalves, T.D. Lyons, S.D. Price, P.D. LeVan and H.H. Aumann, "IRAS Image Reconstruction and Restoration," Advances in Image Processing, Proc. SPIE 804, 16, (1987).

Korte, R.M., J.P. Kennealy, R.A. Gonsalves and C. Wong, "Analysis of IR Celestial Survey Experiments," AF Geophysics Lab. Technical Report, GL-TR-89-0265 (1989). ADA235997

Price, S.D., and R.M. Korte, R.S. Sample, J.P. Kennealy, and R.A. Gonsalves, "A High Resolution Atlas of the Galactic Plane at 12mm and 25mm," Proc. Workshop on Science with High Spatial Resolution Far-Infrared Data, IPAC, Pasadena, CA (1993).

13.0 GALACTIC PLANE SUPPLEMENT

From

IRAS ADDITIONAL OBSERVATIONS

THE GALACTIC PLANE SUPPLEMENT:

THE ADDITIONAL OBSERVATIONS

by

R. Canterna

Leisa Townsley

Robert Hermann

James Benson

Patrick Broos

from the
Department of Physics and Astronomy
University of Wyoming

with consultation from:

Gary L. Grasdalen, G-Star Enterprises

John Hackwell, The Aerospace Corporation

86

THE GALACTIC PLANE SUPPLEMENT:
THE ADDITIONAL OBSERVATIONS

A major proportion (approximately 40%) of the observing time of IRAS was dedicated to pointed observations of pre-selected regions of the sky, centered around certain objects of astrophysical significance. The pointed observations are commonly called Additional Observations or AO's. Approximately 10,000 AO's were planned in six major scientific programs or sub-groups: Active Galaxies (AG), Bright Stars (BS), Close Galaxies (CS), Deep Fields (DF), Molecular Clouds (MC), Galactic Structure (GS), and the Solar System (SY). Two special additional sub-groups (FL and SF) were added to the pointed observations to increase the efficiency of the IRAS satellite data collection and to re-observe special regions discovered during the mission. Specific objects are identified by sub-group type with a running number; there may be multiple observations of the same field labeled A, B, etc.

Typical AO's lasted 15 minutes. Several raster-scanning sequences or MACROS of the IRAS satellite were used to obtain the individual AO data. The scan lengths, cross steps, and scan speeds for each characteristic MACRO were varied for technical and scientific reasons. The reader is strongly encouraged to read A User's Guide to IRAS Pointed Observation Products (Young, E.T., Neugebauer, G., Kopan, E.L., Benson, R.D., Conrow, T.P., Rice, W.L., and Gregorich, D.T. Joint IRAS Science Working Group, 1985, U.S. GPO, Washington, D.C.) for a more complete summary of the AO program.

THE UNIVERSITY OF WYOMING
IRAS IMAGE-ENHANCEMENT PROGRAM

I. A Brief Overview

The principal objective of the IRAS AO high spatial-resolution enhancement component of the "**High Resolution Descriptions of the IRAS 12 and 25 Microns Confused Regions**" program is to provide validation for survey-recovered point source fluxes and positions. This AO work was done at the University of Wyoming. The image enhancement algorithm uses a general technique to treat unevenly-spaced data such as the IRAS AO data. This general technique was developed at the Aerospace Corporation by John Hackwell and uses the maximum entropy recovery algorithm (MemSys5) from Gull and Skilling. Many improvements to the original technique were developed at the University of Wyoming.

1

A point-source extraction algorithm was developed specifically for the maximum entropy-produced IRAS AO images at the University of Wyoming. This robust algorithm produced both positional and photometric measurements of point sources while eliminating low frequency signals due to either a broad, diffuse background or semi-extended, bright HII regions, star formation regions, or molecular clouds.

Approximately 300 individual AO fields were processed within the galactic plane confused region for this program. Roughly 200 of the AO fields are spatially unique. All fields were processed for both the 12 μm and 25 μm bands. Several AO fields were multiple observations of the same region. The choice of such fields was made to provide a representative sample of AO's within the galactic plane confused region.

The analysis of the MemSys images within the galactic plane confused region shows that more point sources are recovered than were extracted for the IRAS PSC, especially at the lower flux levels. The image enhancement algorithm also is able to reconstruct with greater spatial resolution large extended sources that are often misinterpreted as point sources or confused as multiple point sources.

Further validation of the program encompassed ground-based infrared observations of a selected field from the University of Wyoming Infrared Observatory. See Section VIIC for details.

Two final products were produced from this component of the project. The first product is a compendium of reproductions of the final images in FITS format. The second product is a complete catalog of point sources extracted from the final images. These two products are available electronically. To produce the final catalog a robust matching procedure was used to combine multiple observations of individual sources within each band and between bands.

II. The Choice of AO Fields

The most important decision regarding the choice of AO fields was to obtain a representative sample of AO data that would adequately cover the major regions of reconstruction from the survey data. The IRAS galactic plane confused region is defined within a band centered along the galactic plane varying in latitude from $\pm 6°$ ($l = 90°$) to $\pm 15°$ ($l = 0°$) and within $\pm 100°$ in longitude centered around the galactic center ($l = 0°$). Regions in the constellations Cygnus, Orion, and Ophiuchus also were defined as confused. The galactic plane was then separated into 19 regions. An additional region centered on the Orion Nebula also was sampled. The IRAS AO galactic plane regions for this program are listed below in Table 1.

2

TABLE 1.
THE IRAS GALACTIC PLANE REGIONS
FOR
AO IMAGE ENHANCEMENT

Region	Galactic Longitude		Galactic Latitude	
	center	size	center	range
	(degrees)		(degrees)	
1	30	10	0	± 5
2	0	15	0	±10
3	20	10	0	± 5
4	340	10	0	± 5
5	330	10	0	± 5
6	40	10	0	± 5
7	320	10	0	± 5
8	50	10	0	± 5
9	310	10	0	± 5
10	60	10	0	± 5
11	300	10	0	± 5
12	70	10	0	± 5
13	290	5	0	±10
14	80	5	0	±10
15	280	5	0	± 5
16	90	5	0	± 5
17	270	5	0	± 5
18	100	5	0	± 5
19	260	5	0	± 5
Orion	208	10	-19	±10

Figure 1 shows the regions within the confused part of the galactic plane where AO data were processed through the image-enhancement algorithm. In Figure 1 the positions of all single-measurement point sources are plotted as a function of galactic longitude and latitude on an Aitoff projection. The individual AO fields are randomly distributed within the IRAS confused region.

3
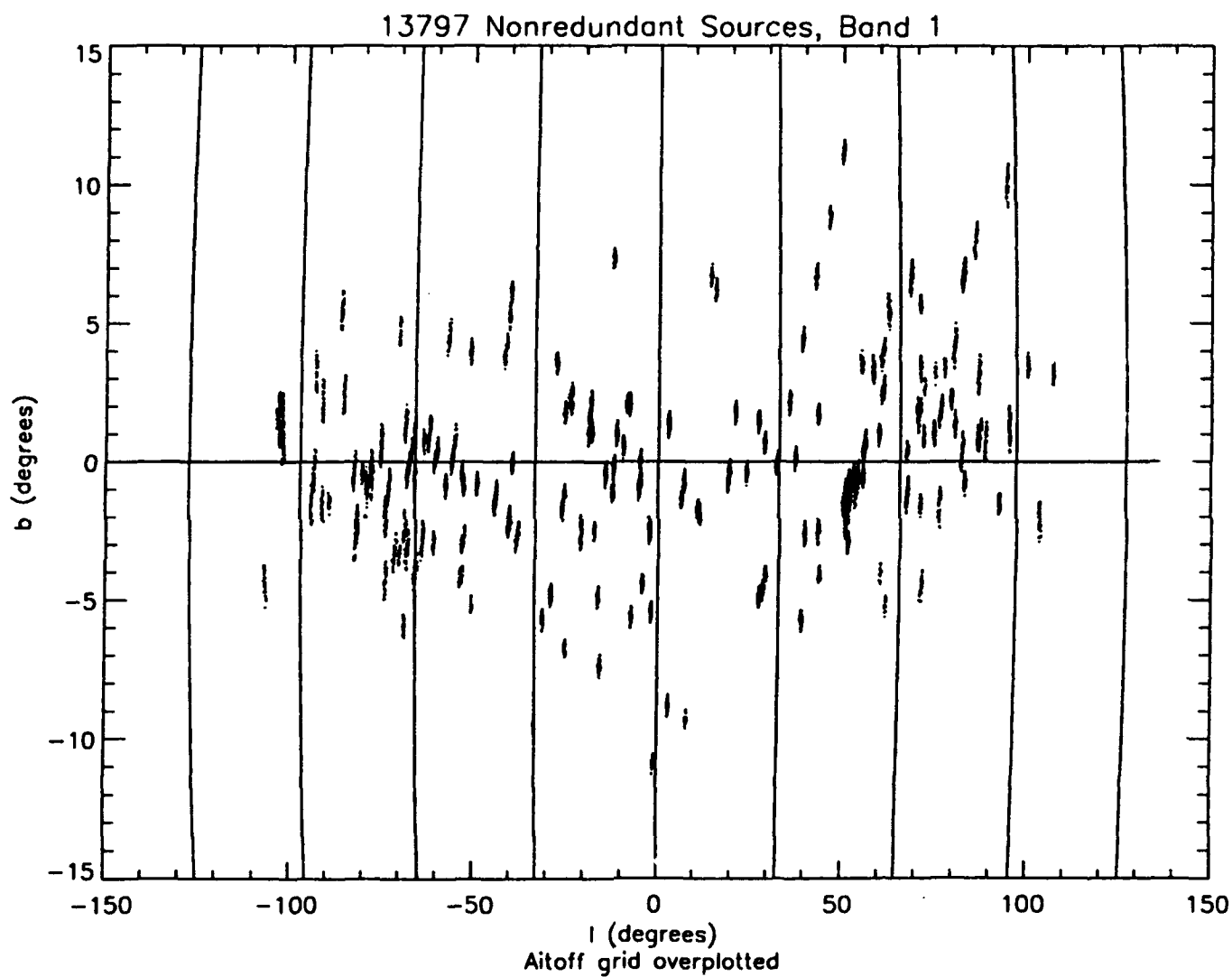
Figure 1. An Aitoff projection of the positions of point sources extracted from the enhanced images. The clustering of points shows the individual AO fields covered by the University of Wyoming's IRAS image-enhancement program.

4

The second most important consideration was the MACRO used for each AO data set. This second constraint was placed on our choice of AO fields because only a select group of AO MACROS have been successfully processed through the maximum entropy program for image enhancement. During the initial development phase of the program, data from a sample of all common MACRO types were processed. For this evaluation only AO fields with relatively flat backgrounds with no major bright sources or extended objects were chosen. The final images were evaluated based on image artifacts due to inadequate data sampling per MACRO type. In addition, certain MACRO types were more heavily used by IRAS and use of a large sample of MACRO types would give the program a more consistent sample of images. Finally, we attempted to include a random sample of sub-group types in order to avoid any selection effect. In Table 2 the AO MACROs used for the image-enhancement program are listed with information about the number of scans of the satellite which cross the object or region of interest, the scan length and cross step in arcminutes, the total observing time to complete each MACRO, the speed of the IRAS satellite relative to the survey speed, and the theoretical signal-to-noise gain based on dwell time. The speed is relative to the survey scan rate of 1, which equals 3.85 arcmin per second.

TABLE 2.
AO MACROS USED IN RECONSTRUCTIONS

MACRO Name	Number Scans	Scan Length	Cross Step	Obs Time (sec)	Speed	SNR gain
		(arc min)				
DSD01A	18	28	0.5	464	1/2	
DPS02B	6	96	0.3	428	1/2	4.8
DPS60B	4	60	0.8	244	1/2	4.0
DPS61D	14	48	0.2	634	1/2	7.7
DPS62D	9	96	0.4	583	1/2	6.0
DPM06D	7	180	<28		1	1.4-4.0

5

III. The Aerospace Image-Enhancement Technique

A. A Brief Overview

One great advantage of the pointed observations is that they are greatly over-sampled with respect to the beam size, especially in the in-scan direction. Thus, in principle, they should lend themselves to image recovery methods that can restore the data to high spatial resolution. Nevertheless, the data have many problems from the point of view of a straightforward image processing problem. The arrangement and geometry of the individual IRAS detectors are key to the unique opportunities and difficulties presented by the IRAS data. A map of the IRAS focal plane shows that the rectangular shapes of the individual detectors were designed to efficiently carry out the survey mission.

The AO data were taken by the IRAS spacecraft scanning back and forth over a given area of the sky. The number, length, and separation of individual scans as well as the scan rate in a given MACRO will vary as indicated in Table 2. An example of a complex pattern of data that is indicative of the IRAS AOs is illustrated in Figure 2, which is a reproduction of the MACRO DPS60B for the object field GS0513 for all 12 μm detectors. Every third datum is plotted in Figure 2 and the detector area given by the small rectangle. The complex pattern of coverage for this and other MACROS is further complicated by the differences among the detectors' point spread functions within a wavelength band.

B. Theory for Randomly Positioned Data

Each data point, d_i, is the result of two processes: the integration over the surface brightness distribution of the sky performed by the total telescope and detector system and the addition of noise by the detector system. Formally, this can be written as

$$F_i = \oint B(\omega_i - \omega) S(\omega)\, d\omega \ , \tag{1}$$

$$d_i = r(F_i,\ t) + n(F_i,\ t) \ , \tag{2}$$

where F_i is the flux falling on the detector, $S(\omega)$ is the surface brightness distribution, $B(\omega_i - \omega)$ is the response of the telescope system, r is the response function of the detector, n is the noise function of the detector, and t is the time at which the data were obtained.
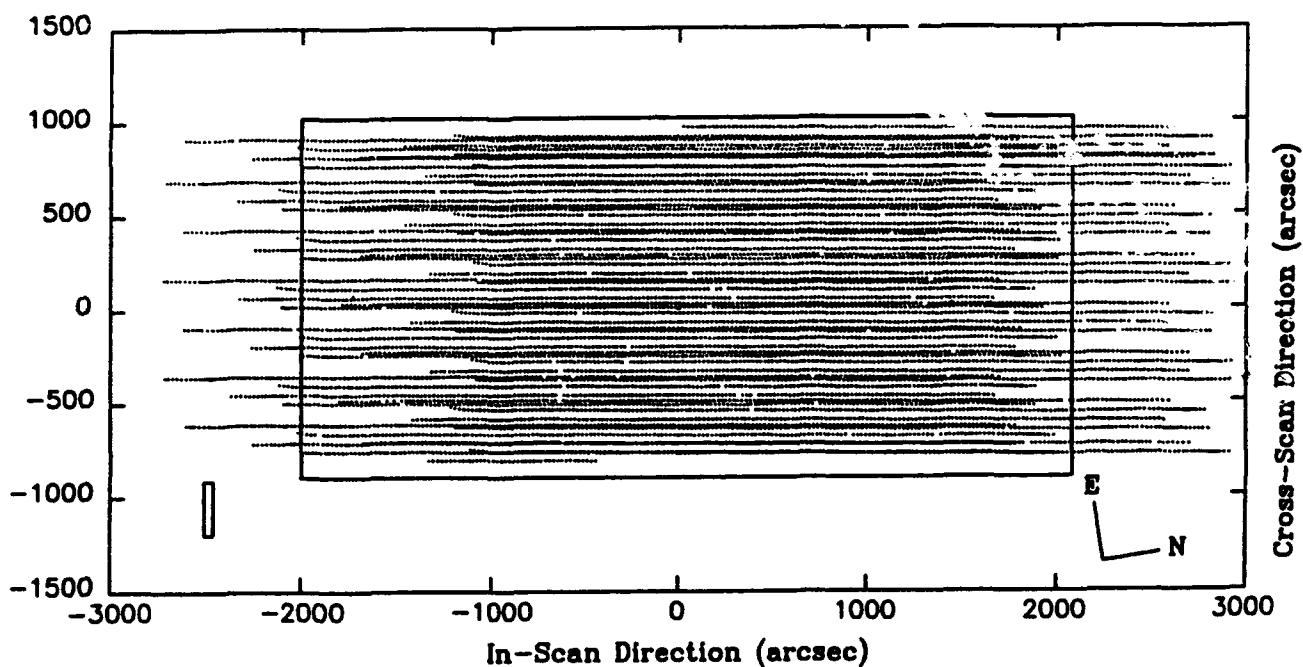
Figure 2. The positions of every third data point are plotted for each 12 μm detector as a function of the in-scan and cross-scan directions for the raster scanning MACRO DPS60B for the field GS0513. The large box outlines the reconstructed area; the small box outlines the size for a 12 μm detector. North and east directions are shown in the lower right-hand corner. Notice the over-sampled data in both the in-scan and cross-scan directions.

The response and noise functions are explicit functions of the flux falling on the detector and the time. Not only is this formally correct, but in the case of IRAS, the response and noise in the detectors was seen to vary with the history of the detector over time scales such as months, weeks and even days. On the basis of the examination of the AO data, neither of these effects come into play during the course of a single pointed observation.

With these simplifications, discrete representations of the sky surface brightness, s_j, and the combined telescope and detector response function, b_{ij}, at the frequency, ω_i, are made and equations (1) and (2) become the linear equation

$$d_i = \sum_{j=0}^{j=M} b_{ij} s_j + n_i \ . \tag{3}$$

The goal of any reconstruction procedure is to obtain estimates of s_j that fit the data within the 'noise'. The least-squares case assumes that the noise is gaussian and that by minimizing the sum of the squares of the residuals (normalized by the widths of the noise distributions), the most likely fit to the data is achieved. The noise normalization is easily carried out. Algebraically, the simplest approach is to divide each data point and its associated beam profile by σ_j. It follows that for

$$H(s_0 \ , \ s_1 \ , \ , \ , \ s_M) = \sum_{i=0}^{i=N} (d_i - \sum_{j=0}^{j=M} b_{ij} s_j)^2 , \tag{4}$$

the goal is to minimize H as a function of the set of discrete sky surface brightnesses, $\{s_j\}$, or the image. Examination of this equation shows how the noise normalization works. This is formally accomplished by setting each of the partial derivatives of H with respect to s_j equal to zero, i.e.

$$\frac{\partial H}{\partial s_j} = 2 \sum_{i=0}^{i=N} b_{ij} (d_i - \sum_{j=0}^{j=M} b_{ij} s_j) = 0 \ . \tag{5}$$

It is very useful to re-write equation (5) in matrix form as

$$B^T D = B^T B S \ . \tag{6}$$

It follows from the defining equation, equation (3), that the matrix B operates on the image, or $\{s_j\}$, to produce an estimate of the data. Unfortunately it is not true that the transpose of B operates on the data to produce an image. Although the number of elements of $B^T D$ is equal to the number of points in the image, it cannot be directly compared to the reconstruction. Operationally, the product $B^T D$ is the sum of each data point convolved by its own point response function. Thus equation (6) is equivalent to Jaynes' Theorem: 'Fit the data convolved by the beam.' The only extension to the customary derivation of this result is that there is no explicit

8

requirement on the spacing or positioning of the data points. The reconstructed points do have to be chosen so that the numerical integration in equation (3) is a reasonable approximation.

The simplest case for equation (6) is that in which the number of data points equals the number of image points. In that case a unique algebraic solution to this equation may be possible. The essence of the present investigation is to ask if realistic approximate solutions to equation (6) can be obtained when the number of points in $\{s_j\}$ and $\{d_i\}$ are not equal. The goal is to demonstrate that, by applying the additional constraints implicit in the maximum entropy technique, realistic reconstructions are obtained.

C. Maximum Entropy Method

A maximum entropy algorithm was used to produce our reconstructions. Although the theoretical basis for choosing one reconstruction method over another is not yet in a satisfactory state, the maximum entropy method has considerable practical advantages. The method consists of solving the transcendental equation

$$S = m \exp(-A (B^TBS - B^TD)) \, , \qquad (7)$$

for a given value of the Lagrange multiplier A. In the process the second Lagrange multiplier m is adjusted to scale the solution to the data. For A=0, the solution of Equation (7) is obviously S=constant. As the value of A is increased, more and more structure will be introduced into the solution. The process of increasing A is terminated at the least squares criterion where the sum of the squares of the residuals is equal to the number of data points, i.e.

$$N = \sum (BS - D)^2 \, . \qquad (8)$$

It is also clear that the size of the structure introduced will be a strong function of the local signal-to-noise ratio (SNR) where the data have been normalized by the noise. Intuitively, this is exactly the behavior for a non-linear reconstruction technique. In regions of high SNR the differences between a point source and an extended object can be easily recognized. In the faint, i.e. low SNR, portions of an image, any structure is difficult to distinguish, as is often even the presence of flux. **Maximum entropy reconstructions naturally produce a variable degree of reconstruction over an image as demanded by statistical theory.**

The effective beam size of each detector is **not** constant over the image. By satisfying the statistical requirements on the effective beam size the ability to intercompare images trivially is negated. The maximum entropy package MemSys5 (Gull, S.F. and Skilling, J. 1991, "Quantified Maximum Entropy MemSys5 Users' Manual," Maximum Entropy Data Consultants Ltd., Meldreth, England) in the 'historical' mode is used for the reconstructions.

D. The Point Spread Functions

The point spread function (psf) of each individual detector is needed to apply the maximum entropy reconstruction rigorously. The original psf's provided by M. Moshir (1987, personal communication) were used initially. However, they were defined using survey data and most of the AO data were obtained at half the survey rate. In addition, the edges of the individual psf's in the cross step direction were not completely determined. To account for these differences, the psf's determined by N.A. Silbermann ("An Investigation of the IRAS Point Response Functions," Master's Thesis, University of Wyoming, 1989) were used.

E. Estimating the Noise

Accurate assignment of the noise is crucial in applying maximum entropy techniques. It is very important that the relative values of the noise from detector to detector are correct. Over large portions of the image field, data from more than one detector will be involved in forming the reconstruction. The numerical value of the noise determines the stopping criterion; therefore, estimates of the noise have a major effect on the overall reconstruction. For these reasons we have invested considerable effort in correctly estimating the noise in the IRAS data.

The noise estimates provided with the footprint scan data by IPAC are often much larger than we deduced from direct examination of the data. These noise estimates are apparently the running standard deviation of the recent data stream and do not reflect the nature of the sky most recently surveyed. The consequences of this method of estimating the noise are documented in the IRAS literature. A more realistic estimate of the detector noise which appears consistent with the actual data is found from the median of the first differences of the data stream. Unlike the survey data, which may originate from scans that are weeks or months apart (see Section B), the AO noise is quite stationary.

Two additional noise sources are considered in the reconstructions. A small fraction of the signal is added in quadrature to the detector noise. This term accounts for small gain fluctuations and minor non-linearities. One way of describing this noise term is to express the accuracy given by repeated observations of a bright source. Setting this noise estimate at 2% of the signal is very reasonable.

An apparent source of the noise due to minor non-linearities is introduced by the gridded nature of the reconstruction. In computing the expected value for a particular data point, the program actually calculates the intensity expected at a grid point rather than at the known coordinates of the data point. The latter calculation could be carried out but would require a different point spread function for each data point, a level of computational complexity that seems extreme. The IRAS beams are difficult to recompute since they have sharp edges and large areas of nearly constant

response. To sample the edges of the beams adequately would require a grid that is much too fine to be realistic in computing reconstructions. Without a very fine grid, however, the current computational scheme produces large residuals at the edges of the beam. Obviously their size depends on the gradient of the signal at these positions. If the data were uniformly spaced there would be no particular difficulty and first differences alone would provide an adequate estimate of the effect.

IV. Pre-Processing of the AO Data

The footprint scan data as supplied by IPAC require processing before they are introduced into the reconstruction code. This pre-processing follows the sequence outlined in Table 3. The steps for the pre-processing are identical for each band and for each MACRO, although some unique differences are band specific and are noted. Following this sequence permitted a batch mode operation of data pre-processing and image reconstruction, which led to maximizing computational efficiency. A brief discussion of many of the specific pre-processing procedures follows.

A. Data Quantization and Intensities

The calibrated IRAS data are in equivalent point source flux density units. Specific intensities are required for image processing purposes. The conversion factor is related to the equivalent solid angle of the point spread functions for the individual detectors.

At the low flux density levels the data are sometimes quantized due to the digitization of the data. The quantization level was determined from a histogram of the data. All the data were then scaled by one-half the quantization value times a random number.

B. Flag detectors, legs, and MACRO

In each field, for each band, the data are sorted into individual scans, detector number, and positional offsets. The MACRO type and reference center were recorded. These data flags were used in calculations of the rotation angle, noise estimates, detector biasing, de-tailing, and proper trimming of data area and image size. Some specific MACRO types had peculiar data strings that were not part of the area of interest and had to be removed.

TABLE 3.
DATA PRE-PROCESSING

Read in data per band; check for quantization

↓

Flag detectors, legs, and MACRO

↓

Conversion to specific intensities

↓

Remove 'glitches'

↓

Calculate rotation angle;
rotate data into image space

↓

'Detail' data

↓

'Destripe' data

↓

Noise estimate

↓

Remove offset/edge effects

↓

Trim data

↓

Send data to MemSys5

C. Removing 'Glitches'

The original data were affected by particle hits. These data were not removed from the footprint AO data set. Two zero-sum filters were used for each scan to remove these spikes or glitches.

D. Rotation Angle Calculation

For each detector and each scan of data the rotation angle was calculated. The first and last seven observations were excluded from this calculation. This was a result of the satellite changing directions before settling into a stable motion. The median value of all rotation angles was then computed for each individual AO field. This rotation was then used to rotate the data into a rectilinear grid or image space where the detector psf's are aligned in the in-scan and cross-scan directions. This rotation angle is also used for the rotational orientation of the image relative to equatorial coordinates. (See information on FITS files of final images in Section VI.)

E. Detailing

Many of the AO observations contain bright objects which exhibited 'detector tails'. Although these effects were attributed by the IPAC staff to complex history effects in the detectors, R. Gonsalves (1989, personal communication) has demonstrated that exponential recursive filters will successfully remove the 'detector tails' for point sources of widely differing brightnesses. We have implemented his three exponential filters on all the data. Gonsalves derived the filters on the basis of survey data. To account for half the survey rate, two scaling factors for the filters were used: one is linear in tail intensity, the second changes the time or point scale of the filters. There may be additional tails due to non-linear effects in the detectors but they have yet to be seen in our AO data. The extreme length of the tails has profound effects on the backgrounds observed in the AO data. Application of these filters clearly makes the slowly varying backgrounds far more consistent between the forward and reverse directions.

F. Individual Detector Bias

After the data are converted to specific intensities, the zero points of the individual detectors are adjusted by examining the scans that come closest to spatially overlapping for successive pairs of detectors. The required offsets between two adjacent detectors are derived by taking the median of pointwise differences between the overlapping scans. A median is required since the overlap is only approximate and point sources may appear in one scan and not the other.

G. Edge Effects

In a field, the outermost data points are the result of a convolution over portions of image space which cannot possibly be reconstructed. The computational difficulty is how to handle that systematic lack of knowledge. The crucial step in resolving this problem was to focus on the behavior of the convolution of the beam with an image of uniform surface brightness. If portions of the convolution that involve points outside of the desired area are ignored, the result is a profile that decays by about a factor of two at each of the edges and a factor of four at the corners. Since that is the result for a uniform surface brightness image, a simulation of that result is made by the proper scaling factor for the edge of the data and the errors in the data.

Since the actual surface brightness is unlikely to remain constant at the edge of the field this approach is not entirely perfect. Consider the case of data which are increasing at the edge of the field. The convolution process will not quite reproduce that increase since it does not know about the increased intensity outside the image field. The reconstruction process puts an additional gradient into the reconstructed image to make up for the deficiency. The general effect will be enhanced gradients at the edge of the reconstructed image. In practice these enhancements are sufficiently small that it is not necessary to take any further precautions in dealing with the edges.

H. Prepare Data for MEMSYS

Finally the data are ready for submission into the maximum entropy program. Based on the AO MACRO the image size is determined and only data within that image space are used. This trimming process is fixed for each individual MACRO.

V. Image Reconstruction and Post-processing

Once the data are adequately prepared by the pre-processing programs, they are then ready for image production and the quantified maximum entropy routine. As mentioned before, the maximum entropy package, MemSys5, by Gull and Skilling (1991) was used. The details of MemSys5 can be reviewed in that publication and its references. The general philosophy and scientific justification for use of a maximum entropy approach to the reconstruction problem is discussed in the Gull and Skilling papers. In Table 4 we summarize the remaining components of the AO image enhancement program. Once the final image was produced, it was visually inspected and then sent to the point source extractor stage. The point sources were identified and measured for their fluxes and positions. The region was then checked for possible PSC sources which were compared with point sources from the enhanced image. The reference center of the image was then recalculated using the PSC comparitors. A final list of sources from each AO field for each band was made. Finally, all sources were then matched for multiple observations within each band and between the two bands. A final catalog of the sources and images was then generated. The details of each step will be discussed.

A. Maximum Entropy Reconstruction

Use of the MemSys5 quantified maximum entropy package is the essence of the image enhancement program. To begin image production, the data had to be adequately prepared for submission into the MemSys standard package. This included allocation of storage space for the data, the successive image reconstructions through the MEMSYS steps, and the construction of two comparison images: a conventional regrid of the data and the initial 'guess' of the starting reconstruction. After extensive trials a uniform image at the level of the average image intensity was used as the initial guess.

The MemSys package had several stopping or convergence criteria available. Through a series of trials we decided to use the modified version of 'historical' maximum entropy in the MemSys5 package for which the convergence criterion is

$$\chi^2 \leq N$$

where N = number of data points. The use of intrinsic correlation functions or a gaussian function in 'classic' maximum entropy to further 'smooth' the image was not applicable to our problem because of the varying shapes of a point source signature throughout the image. The varying shapes of point sources are due to the different detectors which contribute to the point source signature and the incomplete point response function at the cross-scan wings for the large detectors. Minor influences from sparse data sampling and dead detectors also contributed to the variable point source signatures. In addition, 'classic' maximum entropy generated non-reproducible final images.

-15-

All final images were visually inspected to check for obvious artifacts or dominant low frequency stripes. In the former case, these images had either extremely noisy data or were contaminated by 'tails' from bright sources that were not adequately removed. In the latter case, the noise estimate was either too low or too high. We then corrected for this discrepancy and reran the reconstruction. Overall, more than 97% of all the images in the AO program passed the visual inspection the first time.

TABLE 4.
IMAGE RECONSTRUCTION, SOURCE EXTRACTION
AND
THE FINAL CATALOG

Submission into MemSys5

↓

Image convergence

↓

Inspection of image

↓

Submission to extractor

↓

Identification of sources

↓

Source fluxes and positions

↓

Comparison with PSC

↓

Recalculation of reference center

↓

Final list of sources

↓

Binary and global matcher

-16-
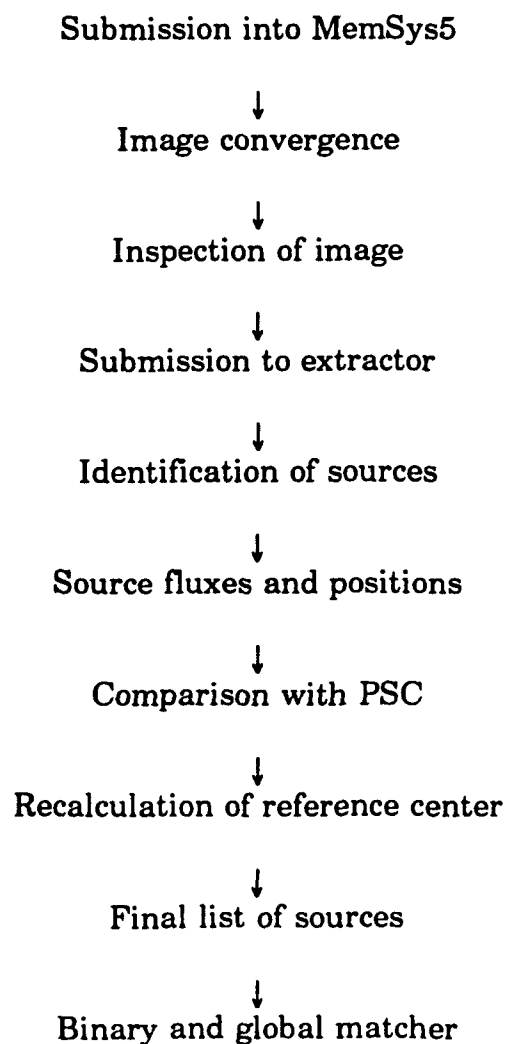
B. The Wyoming Point Source Extraction Program

Once the final, converged, reconstructed image was produced and passed visual inspection, the image was then passed to the point source extractor program. This robust program was used for both 12 μm and 25 μm images.

Two images are used in this program: the MemSys output image and a median-filtered image. Initially, two median filters were applied to the MemSys output image, one 3 pixels wide and the second 7 pixels wide. A difference median-filtered image (3-pixel minus 7-pixel) was generated which produced a bandpass-filtered image approximately centered on the nominal spatial frequency maximum of the MemSys point spread function. This difference median filtered image

- has minimal low and high spatial frequency components,

- has the property that absolute source heights are proportional to the flux,

- provides the initial positional estimate of the point sources,

- enables a SNR-based stopping criterion to be implemented.

The source extraction process begins by first locating the region of a potential source on the basis of its signal amplitude in the filtered image, in order of brightness. The position of this source is then computed from the moments of that region in the MemSys output image. The zero and first order moments characterize the centroid of the point source; the second order moment characterizes the spatial extent of the source. A second pass through this positional filter is made by eliminating all pixels greater than 3 times the second moment. The final centroid position is then recomputed from the zero and first order moments, which give the position and an estimate of the errors in the position.

Next the zero order moment is computed for a region centered on the final centroid position. The mean sky level is computed from the edges of the selected region and the source volume is computed by taking the difference between the zero order moment and the sky level. The local sky σ is computed by using the edges from the selected region. A running mean sky noise estimate, $\hat{\sigma}_{sky}$, is computed from this local sky σ. The SNR of a point source is defined to be the ratio of its source volume to its local sky σ.

All potential sources must pass two validity criteria where (1) the SNR must be greater than 3 and (2) the height, H, of the source in the filtered image must satisfy the following equation:

$$H > 3\, \hat{\sigma}_{sky}\, \mathscr{F} / (2\pi\, \sigma_x \sigma_y)$$

where $\mathscr{F}$ is the difference, median-filter amplitude function evaluated at the spatial frequency maximum of a modeled MemSys point spread function; σ_x and σ_y are the widths of the model gaussian point spread function. Note that $(2\pi\sigma_x\sigma_y)$ is the volume-to-height ratio for a two dimensional gaussian. The model σ_x, σ_y's are determined by fitting 2-dimensional gaussians to various flux-level point source signatures from a typical MemSys image.

Sequentially all candidate sources are selected in order of decreasing height in the difference median-filtered image. Each candidate source must first pass the selection criteria. If the first criterion (SNR) is satisfied, the source is placed in the final source list. If the second criterion (source height) is not satisfied, the extractor procedure terminates. For a valid source a model point spread function whose volume is equal to the source volume is subtracted from the MemSys image. A similar subtraction is made from the filtered image. Finally, the process continues until the second criterion is not satisfied. This means that all point sources in the MEMSYS image whose volume is greater than 3 times the best estimate of the sky noise, $\hat{\sigma}_{sky}$, have been found. One problem with this technique is that the algorithm sometimes turns bright knots and extended emission into a string of point sources. Subsequent processing (both visual and electronic) identified and removed these artifacts from the final point source list.

C. Reference Center Comparisons with the PSC

One of the benefits from using high-spatial-resolution images is the ability to determine more precisely the reference centers of the AO fields. When the final list of sources for a given AO field is made in each band, the positions and fluxes are determined from the data, reference centers, and rotation angle. The PSC is then searched for matches. Once a list of matched sources is found the position of the reference center for the MemSys-produced image is recalculated and used as the final reference center for the image. A comparison between the original AO reference center and the revised position based on the comparison with the PSC sources will be reviewed later (Section VIIA).

D. Matching sources

The core of the matching algorithm for the IRAS AO source list is what we call the **binary matcher**. The binary matcher combines two catalogs of sources. At the lowest level, a catalog is a list of sources found in one AO in one band. The binary

matcher starts by generating a distance array, where each element contains the Euclidean distance from a source in one list to a source in the other list. This array is searched for its minimum, which yields the indices of the two sources which are closest in the whole field. These sources are flagged as a match; then their respective row and column are removed from the distance array and the whole process repeated. The row and column are removed because the two sources are now matched to each other, so all other matches for those sources are disallowed. A distance threshold of 30 arcsec is used as a stopping criterion -- if the smallest distance left in the array is larger than the user-defined distance threshold, the matching process terminates, since we are assuming that separations larger than the distance threshold are not true matches. This distance threshold is based on the FWHM of the average bivariate gaussian of all the source fits and the fraction of sources matched for a given distance threshold. For matches between the final lists of 12 and 25 μm sources, a distance threshold of 45 arcsec was used (see section VIIb).

The binary matcher is the root of the **global matcher**. The global matcher applies the binary matcher to the entire set of 297 AO source catalogs/fields in no particular order on the sky. To start, two catalogs are matched using the binary matcher. The result of this match is recorded in the **biglist**, which contains a list of matched sources supplemented with the list of unmatched sources from each catalog. The next AO source catalog is then matched to the biglist using the binary matcher, generating a list of matches between catalogs 1, 2, and 3, between catalogs 1 and 2, between catalogs 2 and 3, and between catalogs 1 and 3, and appending the lists of unmatched sources from all three catalogs. This process is repeated for all 297 catalogs. The resulting biglist is non-redundant (no source position appears more than once). A given source can be matched several times due to spatially-redundant AO fields.

The advantages of the binary matcher are that it generates an unbiased match (no master/slave problem) and it works in a "natural" way, i.e. given the same task, a human might well take the same approach in generating a matched list - find the pair that is closest, then the next closest, then on and on until a certain separation is reached. The matching is done in ra and dec, which is the universal coordinate system to which all the source positions are translated. The distance metric currently in use is the simple Euclidean distance, i.e.

$$SQRT \{[ra_2*\cos(dec_2) - ra_1*\cos(dec_1)]^2 + (dec_2 - dec_1)^2\},$$

where the subscripts 1 and 2 refer to the two matched sources. A distance metric which incorporates flux or SNR could easily be implemented but the simplest distance formula possible was chosen because incorporating flux into the matching criterion precludes a variable-source search. The coordinates used in the match are weighted-averaged ra and dec of all the individual catalog entries currently matched. The

standard weighting factor incorporates the SNR, the difference between the reference center for the image and the median reference center for the 254 fields where new reference centers were computed, and the width of the bivariate Gaussian for each source. So if a given source in the new catalog is to match to a matched source in biglist, its position must match the <u>average</u> position of the sources in biglist to within the matching radius.

The output of the matching process is a list of indices into the constituent catalogs for matched and unmatched sources. This makes it simple to access all the sources in a given match and execute higher-level processing such as a variable-source test or flux combining without repeating the entire matching run. Then, as more data become necessary or different combining schemes are developed, it is easy and fast to apply them to the list of matches.

VI. The Products of the Project

Two final deliverables were produced from this project in electronic format:

- A compendium of reproductions of each converged 12 μm and 25 μm high spatial resolution galactic plane AO image in FITS format.

- A catalog of point sources extracted from each AO image that can be used as a supplement to the IRAS PSC.

A sample FITS header for the reconstructed images is given in Table 5. The standard FITS words are used and the definitions are given for convenience. The galactic plane AO Point Source Supplemental Catalog includes the source name, following the PSC convention, the position, flux for both Bands in Jy, errors in the position and flux, the minimum SNR of all detections in both bands, and information on the number of detections flagged in noisy regions or regions of extended emission. Included in the catalog is a simple probability estimate of variability based on the chi-square statistic between multiple detections and the number of degrees of freedom (detections). The Q values range from 0 to 1. A value of Q = 0 implies a high probability of variability. For sources with only one detection a null value of -1 is reported. A list of the data entered in the supplemental AO galactic plane point source catalog is given in Table 6.

TABLE 5.
SAMPLE FITS HEADER

```
SIMPLE  =                  T / Written by IDL:  19-Apr-1994 10:58:54.00

BITPIX  =          -32 /

NAXIS   =           2 /

NAXIS1  =          148 /

NAXIS2  =          178 /

DATE    = '19/04/94'        / Creation date (DD/MM/YY) of FITS header

ORIGIN  = 'Wyoming Infrared Observatory' /

TELESCOP= 'IRAS Additional Observation' /

OBJECT  = 'bs0555a '        /

BAND    =           1 /12 microns

CTYPE1  = 'RA      '        /

CTYPE2  = 'DEC     '        /

CRPIX1  =       72.0000 /

CRPIX2  =       129.000 /

CRVAL1  =       282.53760 /RA of reference center (decimal degrees)

CRVAL2  =       -8.79035 /DEC of reference center (decimal degrees)

CDELT1  =       -15.0000 /Number of arcseconds per pixel

CDELT2  =       15.0000 /Number of arcseconds per pixel

CROTA1  =       172.828 /Rotation (degrees E of N from RA into AXIS1)

CROTA2  =       -7.17249 /Rotation (degrees E of N from DEC into AXIS2)

MACRO   = 'DPS60D '         /

BUNIT   = 'W/(m^2*ster)'     /Image units

END
```

TABLE 6.
THE AO GALACTIC PLANE SUPPLEMENT
TO THE
IRAS POINT SOURCE CATALOG

Source Name: The same conventions as the PSC are used, except in the instance of redundant names, in which case the names will have letters appended in alphabetical order with increasing RA

RA: hours, minutes, seconds of time (to tenths of a second), e.g. 10 20 15.5

DEC: degrees, arcminutes, arcseconds

σ_c Cross-scan positional uncertainty for highest-SNR detection in either band, in arcsec

σ_I In-scan positional uncertainty for highest-SNR detection in either band, in arcsec

ROT: Rotation angle for image with highest-SNR detection in either band, in decimal degrees

N1   Number of times the source was detected in Band 1

N2   Number of times the source was detected in Band 2

FLUX1   Weighted-averaged flux density, Band 1 (to 0.1 Jy)

FLUX2   Weighted-averaged flux density, Band 2 (to 0.1 Jy)

DELFL1   Uncertainty in weighted-averaged flux density, Band 1 (to 0.1 Jy)

DELFL2   Uncertainty in weighted-averaged flux density, Band 2 (to 0.1 Jy)

SNR1   Minimum SNR of all detections, Band 1

SNR2   Minimum SNR of all detections, Band 2

TABLE 6 (continued)

Q1   Probability that the chi-squared of the Band 1 fluxes should exceed a particular value of chi-squared by chance. This statistic measures the stability of the flux measurements, so is a measure of potential variability or at least a way to search for discrepant fluxes. Please see Numerical Recipes in C, Second Edition, p. 660 for details of the distribution.)

Q2   (Same as Q1, only for Band 2)

NNOISE1   Number of detections flagged as being in noisy regions of their respective images, Band 1

NNOISE2   Number of detections flagged as being in noisy regions of their respective images, Band 2

NEMIS1   Number of detections flagged as being in regions of extended emission in their respective images, Band 1

NEMIS2   Number of detections flagged as being in regions of extended emission in their respective images, Band 2

VII. FUNDAMENTAL RESULTS OF THE PROJECT

From the information acquired from the extracted point sources a few preliminary fundamental results are required for validation of the AO component of this project. These results include the properties of the supplemental catalog of sources, a comparison of the reference positions, and a comparison of the PSC, AO fluxes, and ground-based observations.

A. The AO Reference Centers

Within each AO field the IRAS PSC was searched for matching sources in each band. Using these matched AO-PSC sources the reference center of the AO data field was recomputed. The reason for this correction is to check the influence of attitudinal control problems of the satellite while the data were taken. In these highly confused regions this information reflects the overall accuracy of the satellite fine guidance system during the pointed observations. In Figures 3a and 3b a histogram of the reference center corrections is given as a function of pixel size (1 pixel = 15 arcsec). For most AO fields the declination axis is in the in-scan direction and the right ascension axis is in the cross-scan direction. The median values for the RA and Dec offsets are 0.09 and -0.31 pixels respectively or 1.35 and -4.6 arcsec. The distributions are gaussian and the half widths are 1.11 and 0.65 pixels for the RA and Dec reference center corrections or 16.5 and 9.7 arcsec.

B. Matched and Unmatched Sources

By applying the binary and global matcher routines, a straightforward analysis of the entire point source catalog from each AO field can be made. Initially a histogram of the half-widths of each source in the in-scan and cross-scan directions, σ_I and σ_C, is made. For both bands the median value for the in-scan direction is 0.87 pixels or 13 arcsec and for the cross-scan direction 1.09 pixels or 16 arcsec.
The position of a source critically depends on the gaussian width of the source, the SNR of the source, and the correct reference center of the AO field. Using this information one would expect the minimum matching distance to be of the order of 21 arcsec. Applying different matching distances to the catalog sources reveals an interesting result. The number of matched sources as a function of matching distance increases exponentially. Therefore a different approach to choose the correct matching distance should be made. For the individual fields we produced a random distribution of point sources and compared the accidental matches. This was done within each band and across the two bands. The results of this matching function

are shown in Figures 4a and 4b. In Figure 4a the number of matched sources minus the number of random matches is plotted as a function of distance threshold for Band 1. A similar function was reported for Band 2. In Figure 4b the same relation is applied to matches across bands. Both results show that a maximum separation is reached, past which the accidental matches begin to influence the total number of matches. For this reason, a distance threshold of 30 arcsec (2 pixels) was used for matches within each band, and a distance threshold of 45 arcsec (3 pixels) was used ac⋅ ⋅ the two bands.

The AO catalog has 24,755 individual detections (entries) with unique ⋅ ⋅ ⋅ions, each having a SNR greater than or equal to 3.0. In Table 7 a compilation of the number of detections and matches is presented. Interestingly, there are 10,538 sources that have at least 1 detection (confirmation) at 12 μm and 13,143 sources at 25 μm. Nearly 2500 sources in both bands had two or more detections. Of the total of 24,755 entries, 10,827 did not have a detection in Band 1; 9,099 in Band 2. Finally, there are a total of 4,829 sources that have at least one detection in both the 12 and 25 μm bands!

TABLE 7.
SOURCE CONFIRMATIONS

Confirmations	Number sources confirmed in Band 1	Number sources confirmed in Band 2
0	10,827	9,099
1	10,538	13,143
2	2,976	2,217
3	230	182
4	167	104
5	8	4
6	9	3
7	0	3

Histogram of RA reference center correction (pixels)

[-2.000, 2.560], binsize = 0.100   Fri Jan 7 15:43:51 1994

median = 0.09

Histogram of Dec reference center correction (pixels)

[-2.000, 1.349], binsize = 0.100   Fri Jan 7 15:42:42 1994

median = -0.31
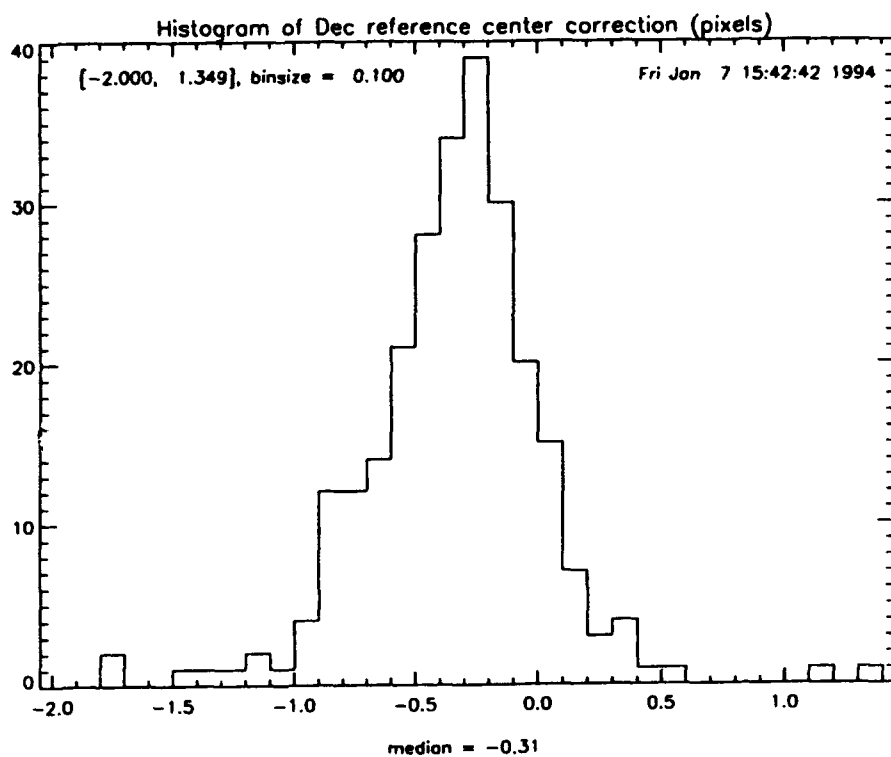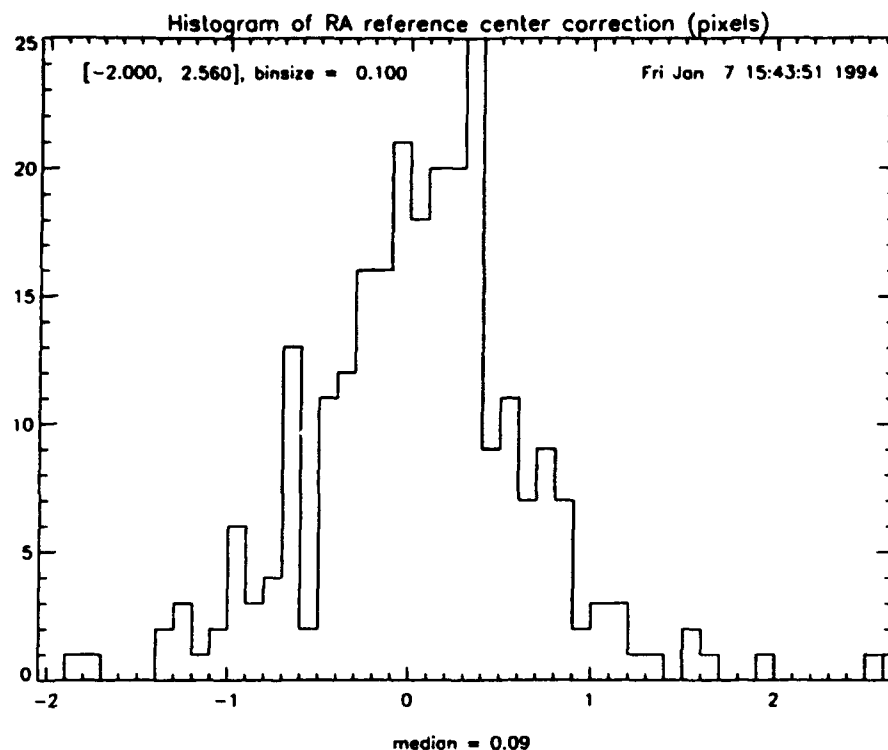
Figure 3a. (top) A histogram of the Right Ascension reference center corrections in pixels for all AO fields.

Figure 3b. (bottom) A histogram of the Declination reference center corrections in pixels for all AO fields.
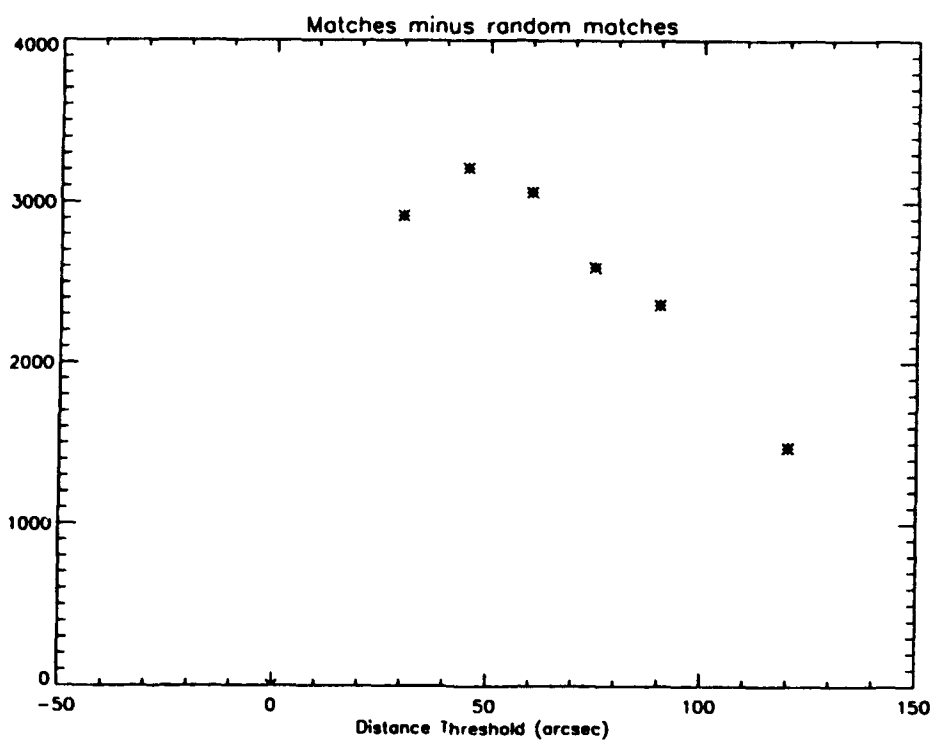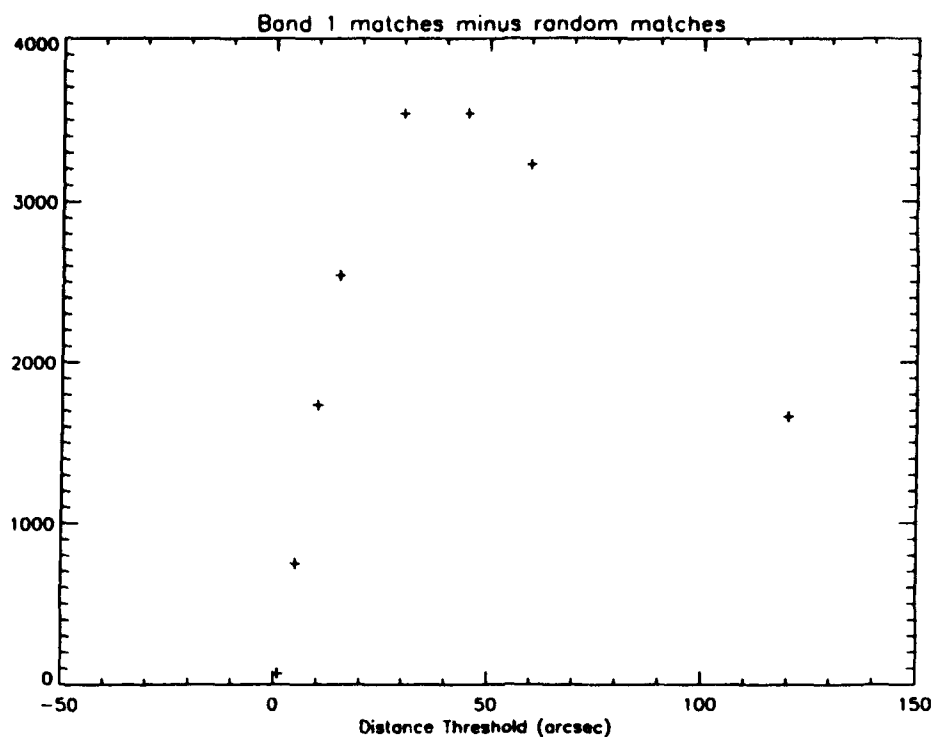
Figure 4a. (top) A plot of the number of matches minus the number of random matches as a function of the distance threshold for sources detected in Band 1 .

Figure 4b. (bottom) A plot of the number of matches minus the number of random matches as a function of the distance threshold for sources detected in both Bands 1 and 2.

C. Photometric Results

Once a reliable list of sources is compiled, a comparison of the photometry with the IRAS PSC is necessary. However, it is important first to compare the ratio of fluxes from matched sources within each band. Following the comparison established by IPAC, Figures 5a and 5b plot a histogram of the natural logarithm of the flux ratio for matched sources for Bands 1 and 2. The distribution is gaussian with widths that are comparable to the IRAS PSC. In Figures 6a and 6b the plot of the logarithm of the 12 μm flux, in Jy, from the AO images versus the logarithm of the 12 μm PSC flux is given for those sources matched between the two catalogs. In Figures 7a and 7b the same plot is given for the 25 μm fluxes. The solid line in all four plots is a slope of unity. Figures 6a and 7a are for single measurements only. Figures 6b and 7b are for all measurements of either single detections or sources with several detections. In all cases notice that the relationship is near unity, with a tendency that the PSC fluxes are slightly higher than the AO fluxes. This is to be expected since the AO images can resolve close sources whereas the PSC combined fluxes from multiple unresolved sources. This is most prevalent for the brightest sources. Notice the deficiency of sources in the upper left-hand side of the relationship compared to the lower right-hand side. This shows that the AO image enhancements will resolve close sources that were unresolved by the PSC. Finally, notice that for sources fainter than 10 Jy, the relationship is nearly 1 with no selection effects.

Another confirmation of the reliability of the photometry produced from the enhanced images comes from ground-based observations. A selected region in the galactic plane, GS0513, near galactic longitude 30° was chosen for ground-based observations at the University of Wyoming Infrared Observatory. Normal infrared observing procedures were used for this part of the program. Observations at 10 μm were made with a standard bolometer, using the standard Wyoming photometric system. The observing technique that we used was to start with either the PSC or AO positions of a list of randomly selected sources. The telescope then made a spiral search for the source. Once a detection was made, the source was centered and then measured for its 10 μm brightness. In Table 8 these data are presented with the AO and PSC results. The PSC or AO name is given, the source's position is given in 1950 coordinates, the offsets, in arcsec, from the PSC or AO positions are given, as are the PSC, AO and observed 10 μm fluxes with errors in parentheses. In Figure 8, the observed N band (10 μm) flux in Jy is plotted versus the 12 μm PSC derived flux (fig 8a) and the AO derived flux (fig 8b).

-29-
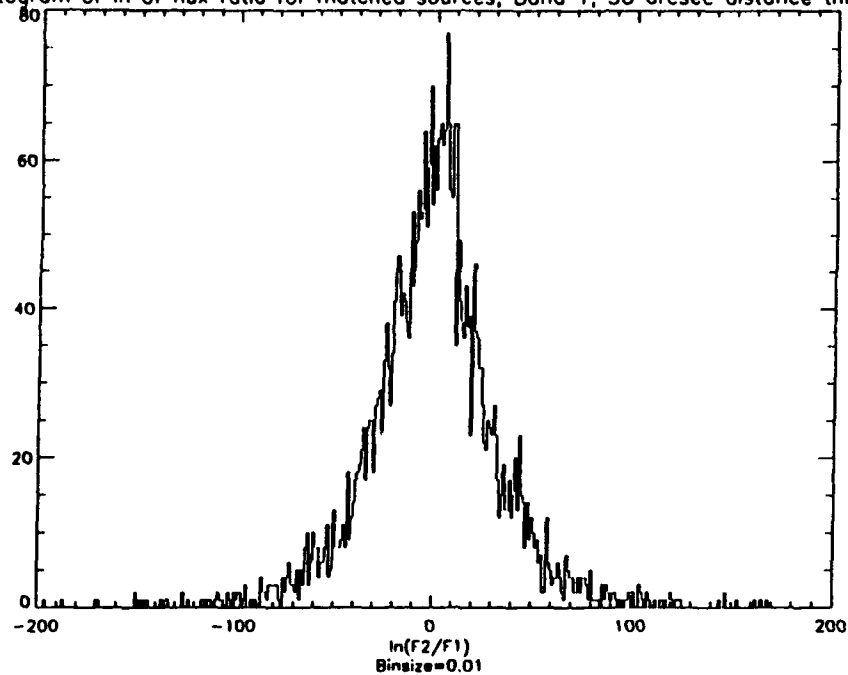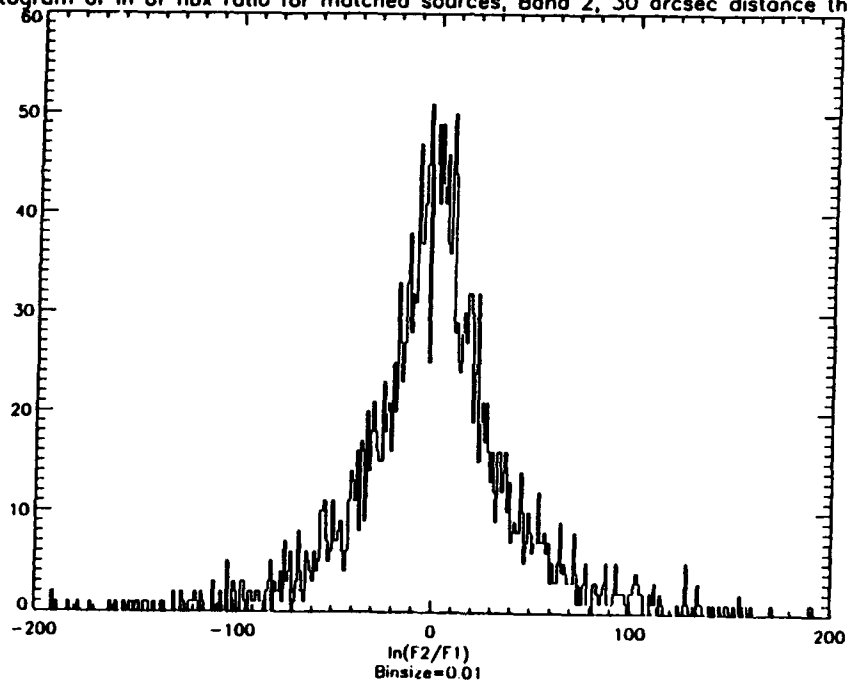
Figure 5a. (top) A histogram of the natural logarithm of the ratio of 12 μm fluxes determined from the AO images from single sources with multiple detections.

Figure 5b. (bottom) A histogram of the natural logarithm of the ratio of 25 μm fluxes determined from the AO images from single sources with multiple detections.
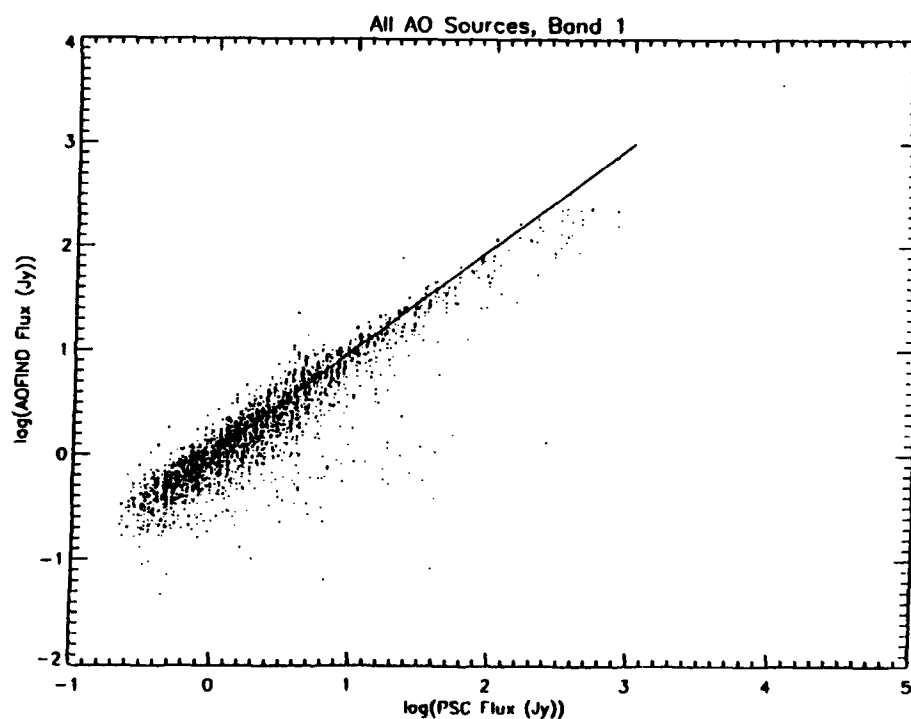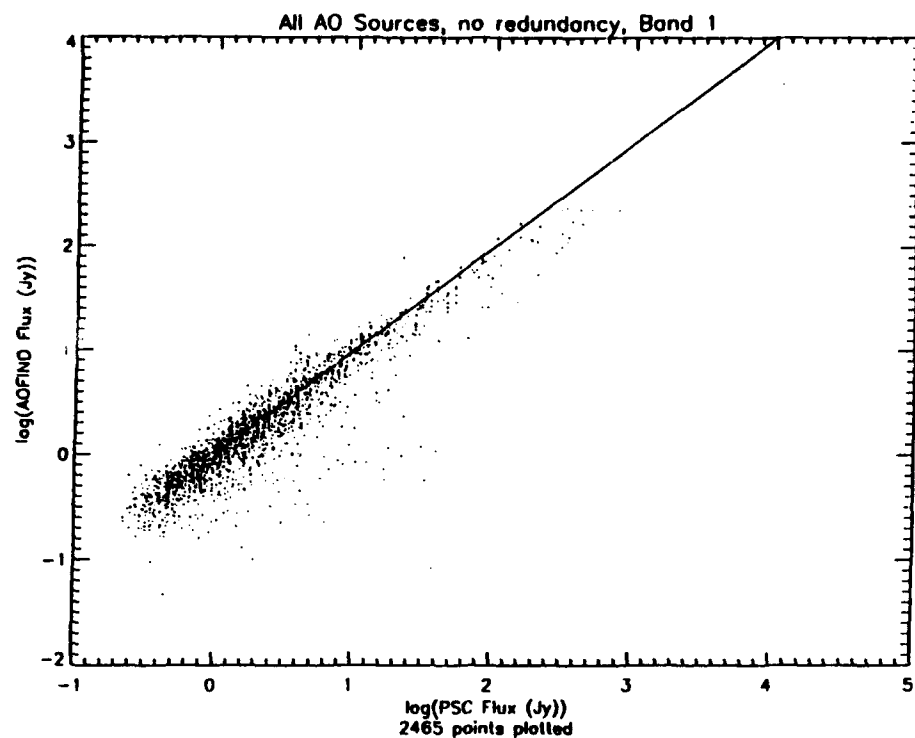
Figure 6a. (top) A plot of the logarithm of the 12 μm flux determined from the AO images versus the logarithm of the PSC 12 μm flux for individual sources with a single detection.

Figure 6b. (bottom) A plot of the logarithm of the 12 μm flux determined from the AO images versus the logarithm of the PSC 12 μm flux for individual sources with a single or multiple detection.

All AO Sources, no redundancy, Band 2

All AO Sources, Band 2
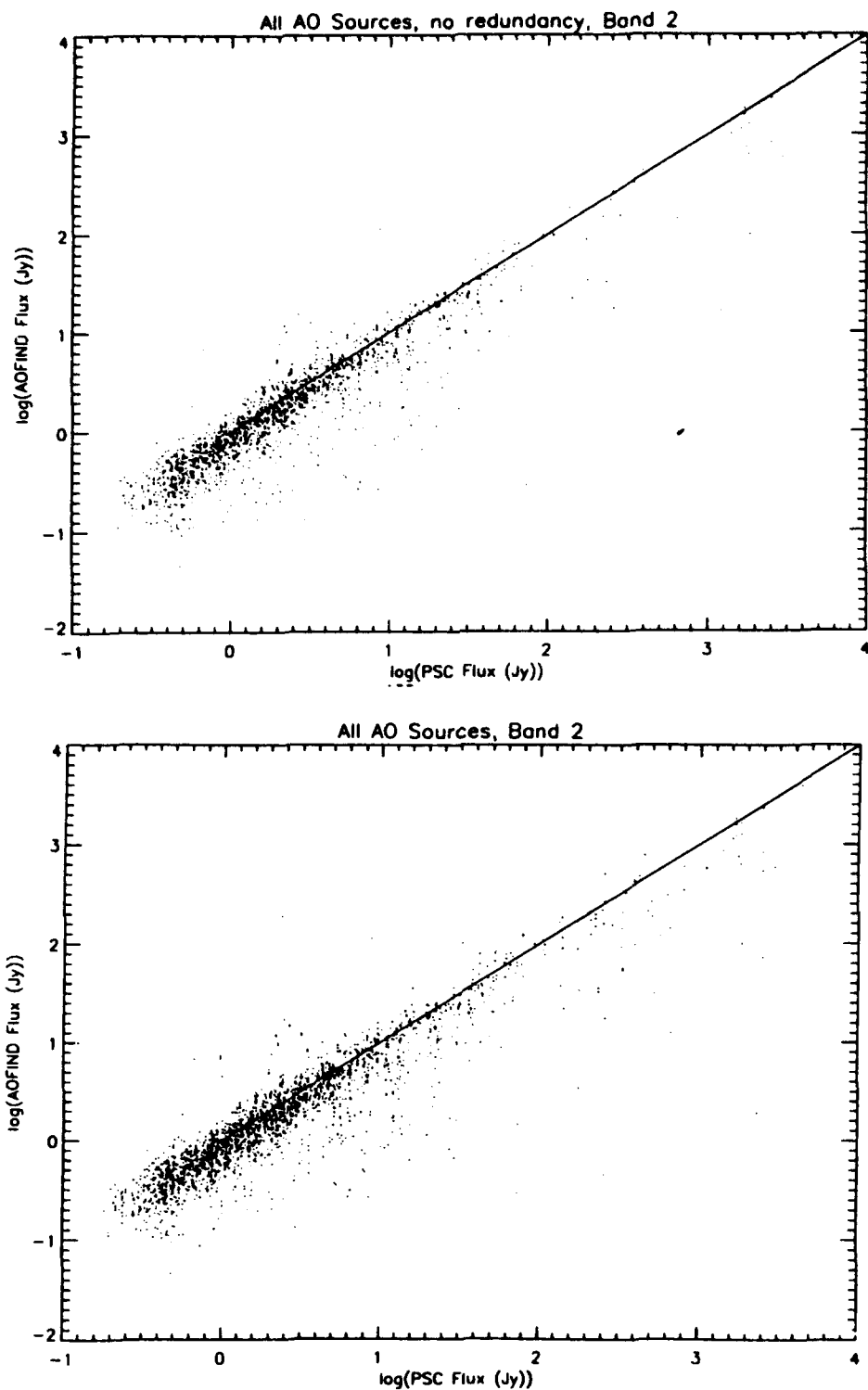
Figure 7a. (top) A plot of the logarithm of the 25 μm flux determined from the AO images versus the logarithm of the PSC 25 μm flux for individual sources with a single detection.

Figure 7b. (bottom) A plot of the logarithm of the 25 μm flux determined from the AO images versus the logarithm of the PSC 25 μm flux for individual sources with a single or multiple detection.

-32-
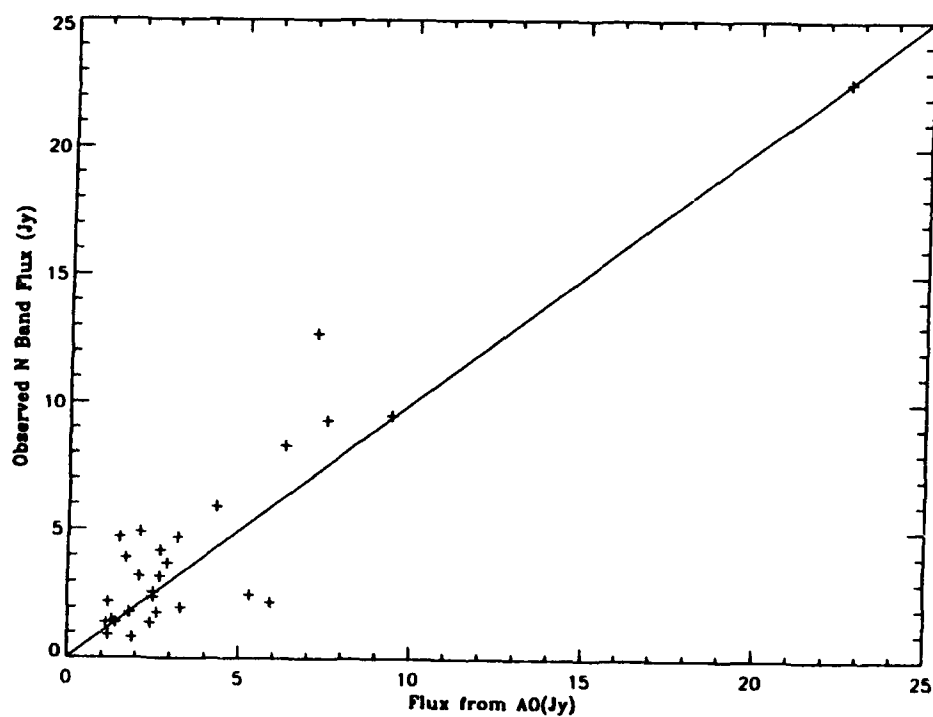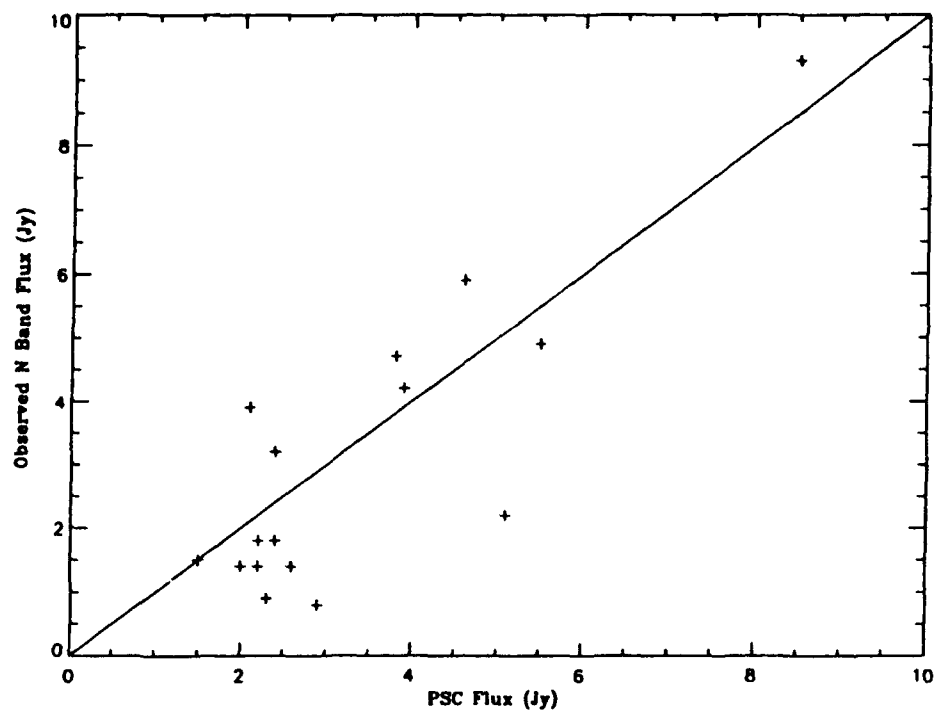
Figures 8a. (top) A plot of the observed N band 10 μm flux and the PSC flux of a select number of point sources in the galactic field GSO513.

Figures 8b. (bottom) A plot of the observed N band 10 μm flux and the AO flux of a select number of point sources in the galactic field GSO513.

TABLE 8.
GROUND-BASED OBSERVING RESULTS

Name	R.A.	Dec	R.A. Dec (Offsets)		PSC	AO	Observed
18418-0305	18:41:52.23	-03:05:38.3	-4.5	-5.5	42.7	22.6	22.6 (0.22)
18417-0305	18:41:44.63	-03:05:49.0	-6.0	3.0	NA	9.4	9.5 (0.36)
18427-0314	18:42:46.88	-03:14:56.0	+31.0	-4.0	8.5	7.5	9.3 (0.39)
18421-0318	18:42:10.38	-03:18:35.0	+17.0	-8.0	5.5	2.1	4.9 (0.30)
18421-0337	18:42:07.60	-03:37:23.0	0.0	-1.0	5.1	5.9	2.2 (0.20)
18430-0310	18:43:04.10	-03:10:15.0	0.0	0.0	4.6	4.3	5.9 (0.25)
18420-0316	18:42:05.68	-03:16:48.0	-12.0	9.0	3.9	2.7	4.2 (0.28)
18428-0316	18:42:49.29	-03:16:51.0	0.0	0.0	3.8	3.2	4.7 (0.13)
18429-0322	18:42:55.79	-03:22:39.0	-17.0	2.0	2.9	1.9	0.8 (0.18)
18430-0331	18:43:00.59	-03:31:53.0	+4.0	-1.0	2.2	1.8	1.8 (0.12)
18425-0304	18:42:34.39	-03:04:35.0	+7.0	+2.0	2.6	2.4	1.4 (0.12)
18431-0335	18:43:06.50	-03:35:54.0	+28.0	2.0	2.4	2.1	3.2 (0.12)
18421-0300	18:42:06.90	-03:00:36.0	+7.0	+7.0	2.4	2.6	1.8 (0.14)
18418-0312	18:41:51.69	-03:12:29.0	-17.0	2.0	2.3	1.2	0.9 (0.14)
18431-0255	18:43:09.78	-02:55:37.9	6.0	5.0	2.2	1.1	1.4 (0.13)
18426-0331	18:42:41.39	-03:31:14.0	-26.0	3.0	2.1	1.7	3.9 (0.49)
18423-0339	18:42:22.29	-03:39:46.0	43.0	0.0	2.0	1.4	1.4 (0.46)
18433-0342	18:43:22.30	-03:42:11.0	-30.0	-2.0	1.5	1.3	1.5 (0.39)
18430-0326	18:43:00.44	-03:26:24.9	-9.0	-4.0	NA	6.3	8.3 (0.32)
18424-0323	18:42:28.00	-03:23:13.0	-22.0	-10.0	NA	7.2	12.7 (0.21)
18423-0328	18:42:22.04	-03:28:55.4	-2.0	-4.0	NA	2.9	3.7 (0.33)
18431-0327	18:43:10.54	-03:27:30.7	-9.0	-6.0	NA	5.3	2.5 (0.36)
18426-0324	18:42:39.08	-03:24:18.4	1.0	-10.0	NA	3.3	2.0 (0.12)
18436-0323	18:43:39.47	-03:23:28.0	-20.0	-7.0	NA	2.7	3.2 (0.09)
18424-0327	18:42:25.26	-03:27:39.6	-16.0	-8.0	NA	2.5	2.6 (0.12)
18427-0326	18:42:46.61	-03:26:00.0	0.0	5.0	NA	2.5	2.4 (0.25)
18420-0316	18:42:02.20	-03:16:00.4	30.0	50.0	NA	1.2	2.2 (0.24)
18422-0320	18:42:13.68	-03:20:46.0	8.0	2.0	NA	0.9	1.6 (0.24)

D. AO INFORMATION

For the sake of convenience a brief catalog of the AO fields that were processed in this program is tabulated. In Table 9 we present the AO name of the field, the grid number, the SOP-OBS numbers, the MACRO of the data, and the galactic plane region.

TABLE 9: AO INFORMATION.

AO NAME	GRID#	SOP	OBS	MACRO	REGION
BS0555A	13090	525	39	DPS60D	1
BS0555B	13156	527	40	DPS60D	1
BS0585A	11329	480	21	DPS60D	1
BS0585B	12212	503	03	DPS60D	1
GS0451A	01688	144	27	DPS60B	1
GS0451B	01736	148	26	DPS60B	1
GS0513C	02450	182	25	DPS60B	1
GS0808C	12548	513	37	DSD01A	1
GS0808D	12894	521	45	DSD01A	1
GS0971	13329	533	42	DPS60D	1
GS0983	13999	557	39	DPS60D	1
MC2888A	13125	527	04	DPS62D	1
MC2888B	13298	533	04	DPS62D	1
BS0411A	11155	474	29	DPS61D	2
BS0411B	11214	476	26	DPS61D	2
BS0451A	10706	463	40	DPS61D	2
BS0451B	10960	469	44	DPS61D	2
BS0453	10958	469	43	DPS60D	2
BS0456A	11784	492	31	DPS60D	2
BS0456B	11976	495	47	DPS60D	2
BS0456C	11568	488	24	DPS60D	2
BS0472A	10384	458	02	DPS60D	2
BS0472B	09833	446	02	DPS60D	2
BS0472C	10729	464	03	DPS60D	2
BS0472D	10270	456	02	DPS60D	2
BS0483	11818	493	03	DPS60D	2
BS0484	12618	515	39	DPS60D	2
BS0637	12083	499	04	DPS60D	2
BS0640	12321	507	04	DPS60D	2
BS0646A	12968	523	05	DPS61D	2
BS0646B	12980	523	15	DPS61D	2
BS0647	13264	531	40	DPS60D	2
GS0770A	10475	459	28	DSD01A	2
GS0770B	10356	457	43	DSD01A	2
GS0772C	10424	458	35	DSD01A	2
GS0772D	10554	460	34	DSD01A	2
GS0773A	11044	471	45	DSD01A	2
GS0773B	10881	467	43	DSD01A	2
GS0784	11387	483	05	DPS60D	2
GS0793A	11946	495	04	DPS60D	2
GS0793B	12149	501	04	DPS60D	2
GS0780A	11070	472	10	DPS60D	2

AO NAME	GRID#	SOP	OBS	MACRO	REGION
GS0780B	10910	468	23	DPS60D	2
GS0799A	12288	505	38	DPS60D	2
GS0799B	12232	503	38	DPS60D	2
GS0800	12311	506	21	DPS60D	2
GS0844	12004	496	22	DPS60D	2
GS0845A	12391	509	06	DSD01A	2
GS0845B	12458	511	04	DSD01A	2
GS0853A	12214	503	04	DSD01A	2
GS0853B	12588	515	04	DSD01A	2
GS0864A	13010	523	46	DSD01A	2
GS0864B	13127	527	05	DSD01A	2
GS0866A	12901	521	52	DPS60D	2
GS0866B	12989	523	26	DPS60D	2
GS0869A	12788	519	49	DPS60D	2
GS0869B	12936	522	14	DPS60D	2
GS0870A	12887	521	40	DSD01A	2
GS0870B	12744	519	13	DSD01A	2
GS0878A	12323	507	05	DSD01A	2
GS0878B	12522	513	04	DSD01A	2
GS0895A	12873	521	22	DSD01A	2
GS0895B	12862	521	13	DSD01A	2
GS0902	12778	519	40	DSD01A	2
GS0923	12485	511	39	DPS60D	2
MC2206A	10548	460	27	DSD01A	2
MC2206B	10367	457	53	DSD01A	2
MC2250	11363	481	39	DSD01A	2
MC2631A	12938	522	20	DSD01A	2
MC2631B	12825	520	20	DSD01A	2
SF0062A	12840	520	32	DPS61D	2
SF0062B	13069	525	05	DPS61D	2
SF0067A	13020	523	53	DPM06D	2
SF0067B	13059	524	29	DPM06D	2
SY0149	12415	509	40	DPS60M	2
SY0150	12444	510	22	DPS60M	2
GS0924A	12777	519	39	DSD01A	3
GS0924B	12787	519	48	DSD01A	3
GS0842A	12886	521	39	DSD01A	3
GS0842B	13009	523	45	DSD01A	3
GS0954A	12945	522	25	DSD01A	3
GS0954B	12958	522	35	DSD01A	3
GS0955	12966	523	04	DPS60D	3
GS0960A	13232	531	03	DSD01A	3
GS0960B	13740	549	04	DSD01A	3

AO NAME	GRID#	SOP	OBS	MACRO	REGION
BS0474	10744	464	17	DPS60D	4
BS0480	10103	452	02	DPS60D	4
BS0481	10402	458	16	DPS60D	4
BS0482	10523	460	02	DPS60D	4
GS0738	10193	454	02	DPS60D	4
GS0739A	10567	460	44	DSD01A	4
GS0739B	10662	462	29	DSD01A	4
GS0743A	10333	457	27	DSD01A	4
GS0743B	10486	459	39	DSD01A	4
GS0754	09500	437	05	DPS60D	4
GS0758	10531	460	08	DPS60D	4
GS0759	10541	460	21	DPS60D	4
GS0767	10816	466	16	DPS60D	4
MC2374A	11275	478	31	DSD01A	4
MC2374B	11372	482	03	DSD01A	4
MC2503A	11128	473	51	DSD01A	4
MC2503B	11191	475	48	DSD01A	4
MC2504	11744	491	57	DPS62D	4
GS0734A	09198	430	36	DSD01A	5
GS0734B	09273	431	61	DSD01A	5
GS0745	10652	462	16	DPS60D	5
MC1123	10580	461	05	DPS02B	5
MC1970A	10990	470	16	DSD01A	5
MC1970B	11078	472	18	DSD01A	5
MC1971A	10995	470	22	DSD01A	5
MC1971B	11083	472	24	DSD01A	5
BS0535	12734	519	03	DPS60D	6
BS0586A	11996	496	13	DPS60D	6
BS0586B	12057	498	08	DPS60D	6
BS0800A	14422	571	03	DPS61D	6
BS0800B	14483	573	03	DPS61D	6
GS0454A	01652	141	18	DPS60B	6
GS0452A	01654	141	23	DPS60B	6
GS0453A	01668	143	05	DPS60B	6
GS0455A	01670	143	10	DPS60B	6
GS0452B	01672	143	19	DPS60B	6
GS0454B	01707	147	04	DPS60B	6
GS0455B	01710	147	10	DPS60B	6
GS0453B	01754	149	22	DPS60B	6
GS0984A	13768	549	40	DSD01A	6
GS0984B	13933	555	42	DSD01A	6

AO NAME	GRID#	SOP	OBS	MACRO	REGION
SF0086A	14098	560	29	DSD01A	6
SF0086B	14320	567	49	DSD01A	6
BS0382A	08280	406	35	DPS61D	7
BS0382B	08358	408	03	DPS61D	7
BS0444A	08731	416	18	DPS62D	7
BS0444B	08781	418	03	DPS62D	7
MC1109A	08498	411	23	DPS02B	7
MC1109B	08909	421	48	DPS02B	7
MC1124	10408	458	22	DPS02B	7
MC1814A	08927	422	24	DSD01A	7
MC1814B	09091	428	23	DSD01A	7
MC1815A	09161	429	60	DSD01A	7
MC1815B	09309	432	36	DSD01A	7
MC2509A	11142	474	09	DSD01A	7
MC2509B	11199	476	03	DSD01A	7
MC2510	11136	474	03	DPS62D	7
BS0587A	12964	523	03	DPS60D	8
BS0587B	13045	524	15	DPS60D	8
GS0810A	12647	516	19	DSD01A	8
GS0810B	12712	518	21	DSD01A	8
GS0811A	13172	528	14	DSD01A	8
GS0811B	13263	531	38	DSD01A	8
MC1115A	01540	135	49	DPS02B	8
MC1115B	02011	163	18	DPS02B	8
MC1131A	01530	135	41	DPS02B	8
MC1131B	01588	137	21	DPS02B	8
MC2302A	12824	520	18	DSD01A	8
MC2302B	12927	522	06	DSD01A	8
MC2335A	13627	544	30	DPS02B	8
MC2335B	13825	551	38	DPS02B	8
MC2336	12899	521	50	DPS02B	8
MC2337A	12871	521	21	DPS02B	8
MC2337B	13569	542	23	DPS02B	8
MC2339	13183	528	25	DPS02B	8
MC2340A	13025	523	57	DPS02B	8
MC2340B	13118	526	25	DPS02B	8
MC2341A	13057	524	27	DPS02B	8
MC2341B	13496	539	40	DPS02B	8
MC2448	13518	540	22	DSD01A	8
MC2933A	14162	562	22	DSD01A	8
MC2933B	14699	579	62	DSD01A	8
MC2934	14002	557	46	DPS02B	8

AO NAME	GRID#	SOP	OBS	MACRO	REGION
MC2938	14386	569	47	DPS02B	8
MC2940A	14903	584	26	DPS62D	8
MC2940B	15055	589	51	DPS62D	8
MC2942	14957	585	69	DSD01A	8
CG1082	08142	403	60	DPS02B	9
GS0614	08045	402	02	DPS02B	9
GS0632	07912	398	24	DPS02B	9
GS0647A	09404	434	20	DSD01A	9
GS0647B	09484	436	18	DSD01A	9
GS0648A	09411	434	28	DSD01A	9
GS0648B	09489	436	26	DSD01A	9
MC1862A	09023	426	17	DSD01A	9
MC1862B	09077	428	03	DSD01A	9
MC2387A	09849	446	17	DSD01A	9
MC2387B	09913	447	48	DSD01A	9
MC2400	09782	445	06	DPS62D	9
BS0374	12892	521	44	DPS61D	10
FL0028A	02833	201	32	DPS60B	10
FL0028B	15519	199	17	DPS60B	10
GS0267	01524	135	35	DPS02B	10
GS0360	01617	139	04	DPS02B	10
GS0378A	02569	188	19	DPS02B	10
GS0378B	02640	190	27	DPS02B	10
GS0812A	13663	458	09	DSD01A	10
GS0812B	13962	556	21	DSD01A	10
GS0880A	13514	540	08	DSD01A	10
GS0880B	14018	558	08	DSD01A	10
GS0974	13548	541	47	DPS60D	10
MC1118	01944	159	31	DPS02B	10
MC2944A	14968	586	09	DSD01A	10
MC2944B	15154	595	11	DSD01A	10
SY0165	14258	565	43	DPS61D	10
SF0276A	14230	565	03	DSD01A	10
SF0276B	14285	566	24	DSD01A	10
SF0304A	14779	581	41	DSD01A	10
SF0304B	14911	584	33	DSD01A	10

AO NAME	GRID#	SOP	OBS	MACRO	REGION
BS0348	06172	344	14	DPS61D	11
BS0372	06880	368	03	DPS61D	11
BS0396	07571	386	10	DPS61D	11
BS0432	08426	409	59	DPS61D	11
BS0584	10894	468	03	DPS61D	11
FL0061	06403	349	14	DPS60B	11
FL0100	10418	458	29	DPS63D	11
GS0622	07522	384	27	DPS02B	11
GS0623	07902	398	17	DPS02B	11
GS0624	07861	396	22	DPS02B	11
MC1727	08162	404	16	DPS02B	11
MC1731	08364	408	10	DPS02B	11
MC1733	08546	412	12	DPS02B	11
MC1737	06918	369	34	DPS02B	11
MC1746A	07111	374	50	DSD01A	11
MC1746B	07999	401	19	DSD01A	11
MC1770	08172	404	29	DPS02B	11
MC1784	07345	379	18	DPS02B	11
MC1895A	08436	409	68	DSD01A	11
MC1895B	09080	428	09	DSD01A	11
MC2396	09827	445	51	DPS62D	11
BS0575	13850	552	22	DPS61D	12
BS0739	14036	585	42	DPS61D	12
BS0802	14616	577	53	DPS61D	12
GS0466	02676	191	46	DPS02B	12
GS0567	03036	215	06	DPS02B	12
GS0813A	14360	569	03	DSD01A	12
GS0813B	14772	581	32	DSD01A	12
GS0855A	14262	565	52	DSD01A	12
GS0855B	14468	572	15	DSD01A	12
GS0887A	14762	581	22	DSD01A	12
GS0887B	15132	593	03	DSD01A	12
GS0938	14717	580	15	DPS60D	12
MC0772	02013	163	36	DPS02B	12
MC1531	03191	223	05	DPS02B	12
MC2534A	14090	560	23	DPS62D	12
MC2534B	14844	583	15	DPS62D	12
SY0164	14203	563	54	DPS61D	12

AO NAME	GRID#	SOP	OBS	MACRO	REGION
BS0316	05919	334	02	DPS61D	13
GS0595	06912	369	23	DPS02B	13
GS0605	07467	382	40	DPS02B	13
GS0619	06565	353	18	DPS02B	13
U10072	06039	340	30	DPS02B	13
MC1356	06278	346	34	DPS02B	13
MC1405	07301	378	23	DPS02B	13
MC1647	06127	343	14	DPS02B	13
MC1712	07777	393	48	DPS02B	13
MC1715	07150	375	41	DPS02B	13
MC1721	07964	399	55	DPS02B	13
MC2021A	07885	397	38	DSD01A	13
MC2021B	09199	430	37	DSD01A	13
AG1219A	02064	165	38	DPS02B	14
AG1219B	02072	165	45	DPS02B	14
AG3435A	13702	547	35	DPS61D	14
AG3435B	13766	549	39	DPS61D	14
BS0803	14469	572	22	DPS61D	14
GS0225	02188	168	24	DPS02B	14
GS0468	03406	227	61	DPS02B	14
GS0476A	02687	192	06	DPS02B	14
GS0476B	02722	193	48	DPS02B	14
GS0474	15438	196	30	DPS02B	14
MC0773	03239	224	35	DPSO2B	14
MC2415B	14827	582	19	DSD01A	14
MC2415A	14691	579	56	DSD01A	14
GS0483	05613	318	21	DPS02B	15
GS0585	05957	336	19	DPS02B	15
MC1126	05866	330	25	DPS02B	15
MC1127	06170	344	02	DPS02B	15
MC1266	05434	314	36	DPS02B	15
MC1406	06693	358	17	DPS02B	15
MC1677A	05942	335	29	DSD01A	15
MC1677B	06015	339	29	DSD01A	15

AO NAME	GRID#	SOP	OBS	MACRO	REGION
BS0260	04818	288	32	DPS02B	16
BS0267	04856	290	16	DPS02B	16
GS0557	03185	222	24	DPS02B	16
MC1682A	06212	345	20	DSD01A	16
MC1682B	06241	345	43	DSD01A	16
MC2558A	11537	487	39	DSD01A	16
MC2558B	11869	493	54	DSD01A	16
GS0494	05305	312	19	DPS02B	17
MC0774	03752	246	28	DPS02B	17
MC1363	04589	284	20	DPS02B	17
MC1254	04684	285	55	DPS02B	17
MC1264	05316	312	28	DPS02B	17
MC1376	05401	314	04	DPS02B	17
MC1331	04866	290	23	DPS02B	18
MC1681A	06251	345	58	DSD01A	18
MC1681B	06610	354	27	DSD01A	18
GS0487	04401	279	10	DPS02B	19
GS0489	04422	279	45	DPS02B	19
MC1191	03368	227	28	DPS02B	19
MC1662A	05097	304	09	DSD01A	19
MC1662B	05155	307	34	DSD01A	19
MC1663A	05100	304	14	DSD01A	19
MC1663B	05152	307	29	DSD01A	19

AO NAME	GRID#	SOP	OBS	MACRO	REGION
AG3023B	10185	453	57	DPS62D	OR
AG3023A	10974	469	54	DPS62D	OR
BS0376A	09073	427	58	DPS61D	OR
BS0376B	09207	430	47	DPS61D	OR
CG0837A	09533	437	41	DPS02B	OR
CG0837B	10376	457	63	DPS02B	OR
FL0127	11878	493	62	DPS63D	OR
MC0874A	01067	113	27	DPS02B	OR
MC0874B	01218	123	23	DPS02B	OR
MC0875A	01222	123	38	DPS02B	OR
MC0875B	01298	125	44	DPS02B	OR
MC2255	11342	480	39	DSD01A	OR
MC2500	12557	513	47	DPS62D	OR
MC2528A	11574	488	35	DSD01A	OR
MC2528B	11646	490	18	DSD01A	OR
MC2568A	11602	489	40	DSD01A	OR
MC2568B	11614	489	51	DSD01A	OR